JESSICA GUARATO DE FREITAS SANTOS

ADJOINT-BASED SHAPE OPTIMIZATION APPLIED TO MULTIPHASE FLOWS

FEDERAL UNIVERSITY OF UBERLÂNDIA
DEPARTMENT OF MECHANICAL ENGINEERING
2023

JESSICA GUARATO DE FREITAS SANTOS

ADJOINT-BASED SHAPE OPTIMIZATION APPLIED TO MULTIPHASE FLOWS

Thesis submitted to the Graduate Program in Mechanical Engineering at the Federal University of Uberlândia in partial fulfillment of the requirements to obtain the degree of **DOCTOR IN MECHANICAL ENGINEERING**.

Concentration area: Heat Transfer and Fluid Mechanics

Advisor: Prof. Dr. Francisco José de Souza

UBERLÂNDIA
2023

Ficha Catalográfica Online do Sistema de Bibliotecas da UFU
com dados informados pelo(a) próprio(a) autor(a).

S237
2023

Santos, Jessica Guarato de Freitas, 1994-
Adjoint-based shape optimization applied to multiphase flows [recurso eletrônico] / Jessica Guarato de Freitas Santos. - 2023.

Orientador: Francisco José de Souza.
Tese (Doutorado) - Universidade Federal de Uberlândia, Pós-graduação em Engenharia Mecânica.
Modo de acesso: Internet.
Disponível em: http://doi.org/10.14393/ufu.te.2023.477
Inclui bibliografia.
Inclui ilustrações.

1. Engenharia mecânica. I. Souza, Francisco José de, 1973-, (Orient.). II. Universidade Federal de Uberlândia. Pós-graduação em Engenharia Mecânica. III. Título.

CDU: 621

Bibliotecários responsáveis pela estrutura de acordo com o AACR2:
Gizele Cristine Nunes do Couto - CRB6/2091
Nelson Marcos Ferreira - CRB6/3074

UNIVERSIDADE FEDERAL DE UBERLÂNDIA
Coordenação do Programa de Pós-Graduação em Engenharia Mecânica
Av. João Naves de Ávila, nº 2121, Bloco 1M, Sala 212 - Bairro Santa Mônica, Uberlândia-MG, CEP 38400-902
Telefone: (34) 3239-4282 - www.posmecanicaufu.com.br - secposmec@mecanica.ufu.br

ATA DE DEFESA - PÓS-GRADUAÇÃO

Programa de Pós-Graduação em:	Engenharia Mecânica				
Defesa de:	Tese de Doutorado Acadêmico, nº 366, PPGEM				
Data:	29/08/2023	Hora de início:	14:00	Hora de encerramento:	16:27
Matrícula do Discente:	11923EMC012				
Nome do Discente:	Jéssica Guarato de Freitas Santos				
Título do Trabalho:	Adjoint-based shape optimization applied to multiphase flows				
Área de concentração:	Transferência de Calor e Mecânica dos Fluidos				
Linha de pesquisa:	Dinâmica dos Fluidos e Transferência de Calor				
Projeto de Pesquisa de vinculação:					

Reuniu-se por meio de videoconferência a Banca Examinadora, designada pelo Colegiado do Programa de Pós-graduação em Engenharia Mecânica, assim composta: Professores Doutores: Aristeu Silveira Neto - FEMEC/UFU; Fran Sergio Lobato - FEQUI/UFU; Carlos Antonio Ribeiro Duarte - UFCAT; Henry França Meier - FURB; e Francisco José de Souza - FEMEC/UFU, orientador da candidata.

Iniciando os trabalhos, o presidente da mesa, Dr. Francisco José de Souza, apresentou a Comissão Examinadora e a candidata, agradeceu a presença do público, e concedeu à Discente a palavra para a exposição do seu trabalho. A duração da apresentação da Discente e o tempo de arguição e resposta foram conforme as normas do Programa.

A seguir o senhor(a) presidente concedeu a palavra, pela ordem sucessivamente, aos(às) examinadores(as), que passaram a arguir o(a) candidato(a). Ultimada a arguição, que se desenvolveu dentro dos termos regimentais, a Banca, em sessão secreta, atribuiu o resultado final, considerando o(a) candidato(a):

Aprovada.

Esta defesa faz parte dos requisitos necessários à obtenção do título de Doutora.

O competente diploma será expedido após cumprimento dos demais requisitos, conforme as normas do Programa, a legislação pertinente e a regulamentação interna da UFU.

Nada mais havendo a tratar foram encerrados os trabalhos. Foi lavrada a presente ata que após lida e achada conforme foi assinada pela Banca Examinadora.

---

sei! assinatura eletrônica

Documento assinado eletronicamente por **Francisco José de Souza**, **Professor(a) do Magistério Superior**, em 29/08/2023, às 16:29, conforme horário oficial de Brasília, com fundamento no art. 6º, § 1º, do Decreto nº 8.539, de 8 de outubro de 2015.

---

sei! assinatura eletrônica

Documento assinado eletronicamente por **Carlos Antonio Ribeiro Duarte**, **Usuário Externo**, em 29/08/2023, às 16:29, conforme horário oficial de Brasília, com fundamento no art. 6º, § 1º, do Decreto nº 8.539, de 8 de outubro de 2015.

Documento assinado eletronicamente por **Aristeu da Silveira Neto**, **Professor(a) do Magistério Superior**, em 29/08/2023, às 16:29, conforme horário oficial de Brasília, com fundamento no art. 6º, § 1º, do Decreto nº 8.539, de 8 de outubro de 2015.

Documento assinado eletronicamente por **Fran Sergio Lobato**, **Professor(a) do Magistério Superior**, em 29/08/2023, às 16:30, conforme horário oficial de Brasília, com fundamento no art. 6º, § 1º, do Decreto nº 8.539, de 8 de outubro de 2015.

Documento assinado eletronicamente por **Henry França Meier**, **Usuário Externo**, em 29/08/2023, às 16:40, conforme horário oficial de Brasília, com fundamento no art. 6º, § 1º, do Decreto nº 8.539, de 8 de outubro de 2015.

A autenticidade deste documento pode ser conferida no site https://www.sei.ufu.br/sei/controlador_externo.php?acao=documento_conferir&id_orgao_acesso_externo=0, informando o código verificador **4699820** e o código CRC **6D335257**.

Referência: Processo nº 23117.055198/2023-51 SEI nº 4699820

To my parents for always encouraging me.

ACKNOWLEDGEMENTS

First of all, I would like to express my deepest thanks to Professor Dr. Francisco José de Souza for giving me continuous support and guidance during these past years. He always made good recommendations for my doctoral study, understood my perspectives, and questions, and had the patience to clear all my doubts. Every discussion with him has brought me great reflections, learning, and, most importantly for me, confidence in the work I have been accomplishing. If I got this far, it is because he did not let me get discouraged by the difficulties.

I would also like to thank Professor Dr. Francisco for providing the computational fluid dynamics code, UNSCYFL3D. Due to his excellent work in the management and maintenance of this code, I did not have to face major problems that could hinder the progress of my research.

I would like to extend my gratitude to my parents, Adriana and Marco Aurélio, for always pushing me to be the best version of myself. I must also thank my life partner, Matheus, for his companionship, complicity, and love.

I am grateful to all my colleagues, professors, technicians, and collaborators in the Department of Mechanical Engineering, especially the Fluid Mechanics Laboratory (MFLab), at the Federal University of Uberlândia (UFU), who have contributed to my academic growth and kept me resourceful.

Lastly, I would like to acknowledge the National Council of Technological and Scientific Development (CNPq) for the financial assistance provided throughout my doctorate.

"You cannot go back and change the beginning, but you can start from where you are and change the ending."

C. S. Lewis

SANTOS, J. G. de F. **Adjoint-based shape optimization applied to multiphase flows.** 2023. 132 p. PhD Thesis, Federal University of Uberlândia, Uberlândia.

ABSTRACT

The adjoint method in computational fluid dynamics (CFD) offers a computationally affordable optimization by efficiently calculating gradients of objective functions with respect to design parameters. It outperforms other methods in terms of computational cost and is widely used in sensitivity analysis. Traditional methods, such as finite difference, require a large number of simulations as the number of design parameters increases, limiting the scope of optimization. However, the adjoint method in CFD allows for gradient calculation of an objective function at the cost of one flow field computation, making it practically independent of the number of design parameters and providing a more flexible and robust optimization tool. The aim of this thesis is to advance knowledge and expertise in the utilization of the adjoint method, with a specific focus on flows inside pipe bends commonly encountered in problems involving multiphase flows with particle transport. The work encompasses validating implementations, optimizing fluid dynamics systems, addressing problems related to particles in optimized systems, and proposing a novel adjoint-based formulation for shape optimization applied to multiphase flows. The adjoint fluid dynamics equations are derived at the level of partial differential equations using the continuous adjoint approach. The frozen turbulence assumption is adopted, neglecting variations of the turbulence field with respect to the design parameters. Furthermore, a technique for mesh adaptation is employed to adjust the shape of the computational domain as it is optimized. Firstly, the adjoint method is applied in a shape optimization process to minimize the total pressure losses in three different pipe fittings. Secondly, gas-solid flows are simulated in both the original and optimized pipe fittings to compare the erosion wear caused by particle impacts on the walls. This investigation explores how single-phase flow optimization can also affect the particle problem, i.e., mitigate erosion. The results demonstrate substantial reductions in peak erosion as a consequence of minimizing total losses, which can potentially increase the service life of these systems. Finally, new adjoint equations are derived to account for the dispersed phase of multiphase flows, and the corresponding sensitivity derivatives are obtained to maximize the deposition efficiency of particles on bend walls.

Keywords: adjoint methods, shape optimization, sensitivity derivatives, computational fluid dynamics, multiphase flows.

SANTOS, J. G. de F. **Otimização de forma baseada no método adjunto aplicada a escoamentos multifásicos.** 2023. 132 f. Tese de Doutorado, Universidade Federal de Uberlândia, Uberlândia.

RESUMO

O método adjunto na dinâmica de fluidos computacional (CFD) proporciona uma otimização computacionalmente acessível, possibilitando que os gradientes das funções objetivo em relação aos parâmetros de projeto sejam calculados de forma eficiente. Ele supera outros métodos em termos de custo computacional e é amplamente utilizado em análise de sensibilidade. Métodos tradicionais, como diferenças finitas, exigem um grande número de simulações à medida que o número de parâmetros de projeto aumenta, limitando o escopo da otimização. No entanto, o método adjunto em CFD permite o cálculo do gradiente de uma função objetivo ao custo de um único cálculo do campo de escoamento, tornando-o praticamente independente do número de parâmetros de projeto, o que viabiliza uma ferramenta de otimização mais flexível e robusta. Sendo assim, o propósito desta tese é avançar no conhecimento e na experiência acerca da utilização do método adjunto, com foco específico em escoamentos em curvas de dutos comumente encontradas em problemas envolvendo escoamentos multifásicos com transporte de partículas. O trabalho inclui a validação de implementações, otimização de sistemas de dinâmica de fluidos, análise de problemas relacionados às partículas nos sistemas otimizados e proposição de uma nova formulação baseada no adjunto para otimização de forma aplicada a escoamentos multifásicos. As equações adjuntas de dinâmica de fluidos são derivadas a nível de equações diferenciais parciais usando a abordagem adjunta contínua. A hipótese de turbulência congelada é adotada, negligenciando variações do campo de turbulência em relação aos parâmetros de projeto. Além disso, uma técnica de adaptação de malha é empregada para ajustar a forma do domínio computacional à medida que é otimizada. Em primeiro lugar, o método adjunto é aplicado na otimização de forma para minimizar as perdas de pressão total em três diferentes curvas de dutos. Em segundo lugar, escoamentos gás-sólido são simulados nas curvas originais e otimizadas para comparar o desgaste erosivo causado pelo impacto das partículas nas paredes. Nessa investigação, explora-se como a otimização de um escoamento monofásico também pode afetar o problema relacionado às partículas, ou seja, mitigar a erosão. A partir dos resultados, reduções na taxa de erosão máxima como consequência da minimização das perdas totais são obtidas, o que pode aumentar potencialmente a vida útil desses sistemas. Por fim, novas equações adjuntas são desenvolvidas para considerar a fase dispersa dos escoamentos multifásicos, e as derivadas de sensibilidade correspondentes são deduzidas para maximizar a eficiência de deposição de partículas nas paredes de curvas.

Palavras-chave: métodos adjuntos, otimização de forma, derivadas de sensibilidade, dinâmica de fluidos computacional, escoamentos multifásicos.

LIST OF FIGURES

LIST OF TABLES

NOMENCLATURE

Abbreviations and Acronyms

2D, 3D	two- or three-dimensional
AD	automatic differentiation
CAD	computer aided design
CFD	computational fluid dynamics
DEM	discrete element method
DNS	direct numerical simulation
DPM	discrete particle method
FFD	free-form deformation
GCI	grid convergence index
LES	large eddy simulation
LPC	lagrangian parcel concept
LSM	level-set method
ODE	ordinary differential equation
PDE	partial differential equation
RANS	Reynolds-averaged Navier-Stokes
RSM	response surface model

SIMPLE	semi-implicit method for pressure-linked equations
SST	shear-stress transport
UNSCYFL3D	in-house finite volume solver: Unsteady Cyclone Flow 3D
URANS	unsteady Reynolds-averaged Navier-Stokes
VOF	volume of fluid

Operators and Specials

$\Delta(\ )$	difference operator
$\delta(\ )$	variation operator
$\delta_\beta(\ )$	convective variation operator (with respect to the position)
$\delta_\phi(\ )$	local variation operator (with respect to the flow)
$\mathcal{O}(\ )$	order of
$\partial(\ )/\partial(\ )$	partial derivative
$\sum(\ )$	sum operator
$V\!\!\!/$	volume
$\nabla\times(\ )$	curl operator
$(\ )'$	turbulent fluctuation of variable
$(\ )\cdot(\ )$	scalar product
$(\ )\times(\ )$	vector cross product
$(\ )^\mathsf{T}$	transpose
$(\bar{\ })$	mean operator
$(\hat{\ })$	adjoint variable
$(\underline{\ })$	discrete variable

$(\vec{\ })$	vector
d( )/d( )	ordinary derivative

Subscripts

d	dispersed phase
f	fluid phase
i, j, k	indices according to tensor notation
m	mixture
n, t, s	indices of local boundary coordinates (normal, tangentials)
p	particle p or particle phase
q	node q
r, φ	indices of cylinder coordinates (radial and circumferential)
2layer	two-layer $k - \varepsilon$ model
eff	effective
in	on inlet boundaries
out	on outlet boundaries
ref	reference value
standard	standard $k - \varepsilon$ model
wall	on wall boundaries

Greek Letters

α	impact angle
β	shape control
$\Delta\gamma$	standard deviation

δn	boundary-normal position shift
δx	position shift
δ_{ij}	Kronecker delta
η	mass loading
η_{dep}	deposition efficiency
Γ	boundary of flow domain
$\Gamma_{\mathrm{wall}}^{+}$	wall boundaries where particle impact velocity is positive
$\Gamma_{\mathrm{wall}}^{-}$	wall boundaries where particle impact velocity is not positive
Γ_{D}	design surface subjected to the shape control
Γ_{O}	part of the boundary carrying the objective function
λ	step of the steepest descent method
λ_{ε}	blending function of the two-layer model
μ	dynamic viscosity
μ_d	dynamic friction coefficient
μ_s	static friction coefficient
μ_t	turbulent viscosity
ω	angular velocity or vorticity
Ω	interior flow domain
Ω_{O}	part of the interior domain carrying the objective function
Φ_p	volume fraction of particles
ϕ	state variable
Ψ	control point sensitivity field

ψ	control point coordinates
ρ	density
ρ_p	particle density
$\sigma_k, \sigma_\varepsilon$	constant of the diffusive terms of $k - \varepsilon$ model
τ_f	characteristic time of the fluid flow
τ_p	particle response time
τ_w	wall shear stress magnitude
ε	turbulent kinetic energy dissipation
$\vec{\Omega}$	relative angular velocity between particle and fluid
ξ	Gaussian random number

Latin Letters

$\dot{m}$	mass flow rate
$\dot{m}_f$	mass flow rate crossing cell face
$\mathcal{R}$	vector of residuals
$\overline{u'_i u'_j}$	Reynolds stress tensor
$\tilde{x}, \tilde{y}, \tilde{z}$	system of local coordinates that defines a control volume
A	width of the blending function used in the two-layer model
$A_\varepsilon, A_\mu, C_l$	constants in the two-layer model
$B_{i,l}$	Bernstein polynomial of degree l
$C_{\varepsilon_1}, C_{\varepsilon_2}, C_\mu$	constants in the $k - \varepsilon$ model
d_p	particle diameter
e	restitution coefficient

f_d	term of drag force
F_{d_i}	drag force
F_{ls_i}	shear-induced lift force
G	complete gradient
G^*	non-dimensional gradient
g_i	gravitational acceleration
G_{var}	auxiliar variable used for calculating the gradient
I_p	moment of interia of particle
J	objective function
k	turbulent kinetic energy
L	Lagrange function
l	characteristic length
l, m, o	number of control points in 3D
l_ε, l_μ	characteristic lengths in the two-layer model
M	number of (discrete) control parameters
m_p	particle mass
N	number of (discrete) constraints or number of cells
n, t, s	system of local boundary coordinates
N_p	number of particles
p	pressure
p^+	modified pressure
Q	residual of continuity equation

Q_p	residual of volume fraction equation
r, φ	system of cylinder coordinates
R_i	residuals of linear momentum equations
r_i, r_o	inner and outer radius of coaxial cylinders
R_{p_i}	residuals of linear momentum equations of particles
Re_y	Reynolds number of the region near the wall
S	rate of strain
S_{ij}	rate of strain tensor
St	Stokes number
t	time
T_i	torque acting on particle
U	average velocity
U_∞	velocity of free stream
u_i, u, v, w	velocity components of fluid
u_{p_i}, u_p, v_p, w_p	velocity components of particle
x_i, x, y, z	cartesian coordinates
y^+	dimensionless distance from a point to the wall

SUMMARY

CHAPTER I

INTRODUCTION

Making purchase decisions based on cost, quality, and personal preference; allocating time for work, leisure, and other activities to maximize productivity and satisfaction; and budgeting and investing are just a few examples that show how the concept of optimization is present in many aspects of people's daily lives. This ability to optimize helps them make decisions that improve their quality of life and overall well-being.

In engineering, as stated by Saramago (2012), optimizing means improving what already exists or designing something new with more efficiency and lower cost. This is commonly combined with numerical techniques to find the best design configuration without testing all possibilities. Hence, the great advantage of optimization is to reduce the time dedicated to project, allowing the treatment of large systems with restrictions.

With energy costs constantly increasing, optimizing power consumption has been a persistent concern in many process industries. Specifically in pipelines, fittings may represent important components in the overall energy budget as they may be responsible for most pressure losses and, thereby, require most of the pumping power. In this context, it is highly desirable to devise accessory shapes that minimize losses. This may result in unconventional shapes, but with modern manufacturing techniques, the manufacturability of these pipeline components should not be an issue.

Although optimization is a natural human ability, proposing an optimal design based on intuitive insight is normally difficult, especially considering the typically wide range of design variables and potential constraints. Clearly, there is a demand for shape optimization methods.

One common technique for shape optimization is to obtain the search direction for design improvement by computing the sensitivity derivatives of an objective function with respect to the design variables. However, in addition to the optimization process, it is worth mentioning that the fluid dynamics equations must be solved. Thus, there is a need for numerical methods that achieve the best possible design while not incurring high computational costs. The adjoint methods fit into such a category of methods due to an important advantage over the others: the gradient of the objective function is obtained with only one single calculation. Consequently, the computational effort of these methods does not depend on the number of design variables, whereas the naivest methods would require calculating the derivatives relative to each design variable.

Adjoint methods surely render themselves to the optimization of fluid systems and have been successfully used over the last decades (REUTHER *et al.*, 1996; KIM *et al.*, 2001; ZYMARIS *et al.*, 2009; STÜCK, 2011; HINTERBERGER; OLESEN, 2011; OTHMER, 2014; KRÖGER; KÜHL; RUNG, 2018). The first appearances of these methods are found in the works of Pironneau (1974) and Jameson (1988). These authors focused on minimizing the drag force or maximizing the lift-to-drag ratio of bodies immersed in a fluid, which are common applications in the area of aerodynamics. In the case of internal single-phase flows, generally, objective functions focus on minimizing total losses, pressure drop, or flow inhomogeneity (OTHMER, 2008).

Basically, adjoint methods are divided into continuous and discrete approaches, and deciding which one is more appropriate for a desired application is a pertinent question. For computational fluid dynamics (CFD) solvers based on the finite volume method, the implementation of the continuous adjoint approach can be more straightforward (OTHMER, 2008).

Pipeline components are also very prone to erosion problems. Previous works (DUARTE; SOUZA; SANTOS, 2016; SANTOS; SOUZA; DUARTE, 2016; DUARTE; SOUZA, 2017) have proposed several possibilities for geometric changes to mitigate erosion caused by particles carried in a fluid flow, most of which were based on practical experience and somehow intuitive. Despite their significant gains in terms of reducing peak erosion, such geometries can be difficult to propose in other situations based only on physical insights, particularly when a complex geometry is involved and the physics and erosion mechanisms are not well known. Furthermore, the proposed geometries normally increase the system pressure drop. In this sense, adjoint methods can be powerful tools as they will naturally indicate designs, possibly with different degrees of complexity, that would otherwise be impossible to obtain by pure intuition.

Few developments for multiphase flows have been proposed (KRÖGER; KÜHL; RUNG, 2018), as there are still fundamental limitations in adjoint methods that might prevent their commonplace usage. The Euler-Lagrange approach, for example, has been the workhorse in particle-induced erosion simulations. Unfortunately, the adjoint theory is not applicable to the Lagrangian formulation. Alternatively, an Euler-Euler approach could be applied to simulate dispersed multiphase flows.

The main goal of this thesis is to demonstrate how multiphase flow systems can be improved through a shape optimization process with the application of an adjoint method. The first objectives are to optimize different accessories commonly used in pipelines in process industries while minimizing a single-phase flow problem and to compare the particle-induced erosion caused in the original and optimized systems. Given the lack of a formal demonstration of erosion reduction, evidence will be provided to show that this side effect can be obtained even for high Stokes numbers, in which the correlation between fluid and particle flows is low. Although minimizing functions related to the continuous phase can indirectly benefit from information associated with the dispersed phase of a multiphase flow, there are no well-defined adjoint equations in the literature to specifically control information related to particles, such as erosion or collection/deposition efficiency. Until now, adjoint-based shape optimization for multiphase flow systems has not been available in open-source or commercial software. A few research codes have addressed this issue, but they still exhibit several limitations. Accordingly, the subsequent objectives are to propose adjoint equations that consider particle transport in the optimization process and implement them.

The research methodology is based on computational simulations, with the finite volume, unstructured CFD code, UNSCYFL3D, as the primary component. This in-house code was used to solve both fluid dynamics and optimization problems, requiring the implementation of the adjoint equations and the optimization algorithm. The adjoint solver developed in this work is not restricted to the presented cases, so it is also applicable to other fluid dynamics problems. Nevertheless, minor adaptations may be necessary to customize the adjoint post-processing to a particular type of control or to account for different objective functions.

The present thesis is organized into six chapters, each addressing specific aspects of the research. The current chapter provides a brief introduction to the subject, including an overview of the research topic and outlining the research objectives. In Chapter 2, a comprehensive review of the relevant literature is presented, covering topics related to multiphase flows and shape optimization of fluid dynamics systems based on adjoint methods. Chapter 3 is focused on the single-phase flow optimization problem, presenting the shape optimization of different pipeline bends. The erosion problem is investigated in the original pipeline bends and their optimized shapes and discussed in Chapter 4. The multiphase flow optimization problem is further explored in Chapter 5, considering the complexities specific to particle equations and exploring the application of adjoint-based optimization. Lastly, outlook and final remarks are offered in Chapter 6, summarizing the key findings, discussing limitations, suggesting future research directions, and concluding the thesis.

CHAPTER II

LITERATURE REVIEW

A selection of central issues observed in the context of shape optimization applied to fluid dynamics systems is discussed in the following. The focus is on incompressible fluid dynamics related to multiphase flows. Even though erosive wear is not the main focus of this thesis, it is an explored problem and, therefore, addressed here. The chapter ends with a review of shape optimization, presenting the optimization methods and, finally, the adjoint methods.

2.1 Simulation of fluid dynamics systems

The fundamental laws of classical mechanics are applicable to fluid flow. These laws lead to the mass balance equation and the linear momentum equations, also known as the Navier-Stokes equations, a group of equations composed of partial derivatives that describe fluid behavior. Within the CFD technique, complex system geometries are replaced by thousands (even millions) of known elements, and systems of partial differential equations (PDEs) are represented as a set of approximate algebraic equations. For most software used in CFD simulations, including ANSYS® Fluent, STAR-CCM+®, and OpenFOAM®, the finite volume method is employed. Therefore, each element is seen as a small control volume in which discretized versions of the equations are solved iteratively.

Most flows found in nature and in practical applications are turbulent. Thus, how to model turbulence plays an important role in CFD problems. Three main approaches can be distinguished to predict the evolution of the turbulent flow. Choosing one of them depends on the specific application, the accuracy required, and the computational resources available. In general, requiring a higher mesh resolution implies a more computationally expensive model.

The simulation of turbulent flows by just numerically solving the fluid dynamics equations requires resolving a wide range of characteristic time and length. Hence, the mesh spacing must be smaller than the smallest structure of the flow to ensure proper resolution. This resolution can be achieved with direct numerical simulation (DNS). The computational cost of this approach, though, turns out to be prohibitive for simulating practical engineering systems with complex geometry or flow configurations.

Ignoring the smallest structures, the computational cost of simulating the turbulent flow is reduced. This can be achieved with the large eddy simulation (LES), in which the filtered Navier-Stokes and mass balance equations are solved. In this sense, only the large turbulent structures are resolved, which does not mean that the information related to the small structures is irrelevant. For this reason, the effects and the interaction of the small structure (smaller than the filter size, which depends on the mesh spacing) with the resolved structures must be modeled.

The third approach consists of time-averaging the fluid dynamics equations, which are known as the Reynolds-averaged Navier-Stokes equations (RANS). However, this process causes the appearance of a nonlinear term, referred to as the Reynolds stress, that requires additional modeling to close the RANS equations. A great diversity of turbulence closure models can be found in the literature. They mainly differ between those that depend on the turbulent viscosity of the flow and those that do not. Clearly, the RANS-based approach is computationally cheaper than the previous ones.

The turbulent structures resolved in each of the approaches are illustrated in Fig. 2.1. Observing the figure, there are still the URANS (unsteady Reynolds-averaged Navier-Stokes) class models, which are different from RANS due to the time term considered in the average equations, and the hybrid methods, which are the result of a combination of RANS and LES models. More information about turbulent flow simulation is available at Pope (2000), Lesieur, Métais, and Comte (2005) and Wilcox (2006).

Figure 2.1 – Illustration of the turbulent structures resolved by modeling approach.

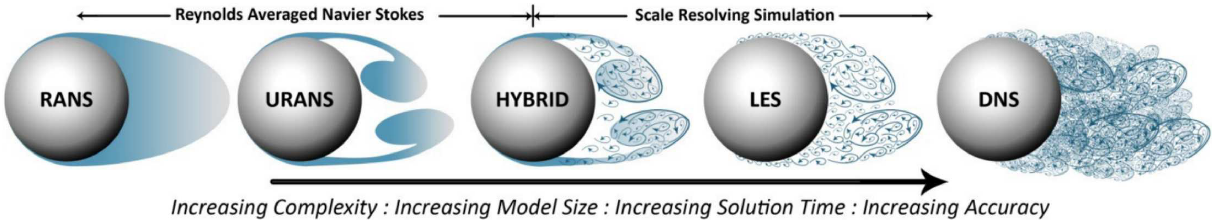

Source: Hart (2016).

In the context of multiphase flows, just using one of the above methodologies is not enough, as more than one phase needs to be modeled. Before presenting the numerical approaches for multiphase systems, some fundamentals will be reviewed in the next section.

2.2 Multiphase flows

Matter can exist in three typical phases: solid, liquid, and gas. A multiphase flow consists of a mixture of two or more phases, in which at least one phase consists of non-continuous elements that are dispersed in a continuous phase composed of a carrier fluid. In cases where two phases are separated in the form of two streams sharing a definite interface, the flow is often referred to as a separated flow. The annular flow in a pipe, which includes a liquid layer on the pipe wall and a core of gas, is an example of separated flow.

Depending on the nature of the multiphase flow, the dispersed phase can take various forms, such as droplets, bubbles, or solid particulates. For the sake of brevity, all these forms will be called just particles in this thesis. Some examples and applications of multiphase flows are displayed in Tab. 2.1. Three-phase flows are also found in a few engineering systems. For example, bubbles rising in slurry (solids suspended in liquid). However, these flows have a higher degree of complexity, and because of that, not much research work has been reported in the literature on them (MICHAELIDES; CROWE; SCHWARZKOPF, 2016).

Table 2.1 – Summary of multiphase flow systems and important industrial and technical processes.

Continuous-dispersed phase	**Industrial and technical applications**
Gas-solid flows	Pneumatic conveying, particle separation in cyclones and filters, fluidized beds
Liquid-solid flows	Hydraulic conveying, liquid-solid separation
Gas-droplet flows	Spray drying, spray cooling, spray painting
Liquid-droplet flows	Mixing of immiscible liquids, liquid-liquid extraction
Liquid-gas flows	Bubble columns, aeration of sewage water, flotation

Source: Modified from Sommerfeld (2017).

A deep understanding of the flow behavior and properties can be achieved through flow characterization. This process involves analyzing the relevant physical parameters of the flow and studying the underlying physical mechanisms, which turn out to be very relevant for flow modeling. In this sense, multiphase flows can be characterized by the Stokes number, the flow regime, and the coupling type between phases. More details on each parameter will be discussed separately below.

2.2.1 Stokes number

The Stokes number St is a dimensionless parameter used to characterize the behavior of the particles in the fluid flow. This number is defined as the ratio of the particle response time τ_p to the characteristic time τ_f of the fluid flow (CROWE *et al.*, 2011):

$$St = \frac{\tau_p}{\tau_f}. \tag{2.1}$$

The particle response time is the time a particle takes to reach a steady-state velocity when subjected to a constant force, and it depends on the particle density ρ_p, the particle diameter d_p and the dynamic viscosity of the fluid μ:

$$\tau_p = \frac{\rho_p {d_p}^2}{18\mu}. \tag{2.2}$$

On the other hand, the characteristic time of the flow is determined as:

$$\tau_f = \frac{l}{U_\infty}, \tag{2.3}$$

where l is the characteristic length of the flow and U_∞ is the velocity of the free stream.

When the Stokes number is very small ($St \ll 1$), the particle response time is shorter than the characteristic time of the fluid flow. This means that the particles have enough time to react to the velocity changes in the flow. Therefore, the particles follow the turbulent structures closely and do not exhibit any significant inertia. In contrast, when the Stokes number is large ($St \gg 1$), the particles cannot respond to the velocity changes in the flow and end up passing almost in a straight line through the turbulent structures. Finally, when the Stokes number is moderate ($St \approx 1$), the particles have sufficient inertia to deviate from the turbulent structures, although they are somehow still affected by the velocity field (CROWE *et al.*, 2011; SOMMERFELD, 2017). The effect of the Stokes number on particle behavior in turbulent flows is illustrated in Fig. 2.2.

Figure 2.2 – Effect of Stokes number on particle dispersion in turbulent structures.

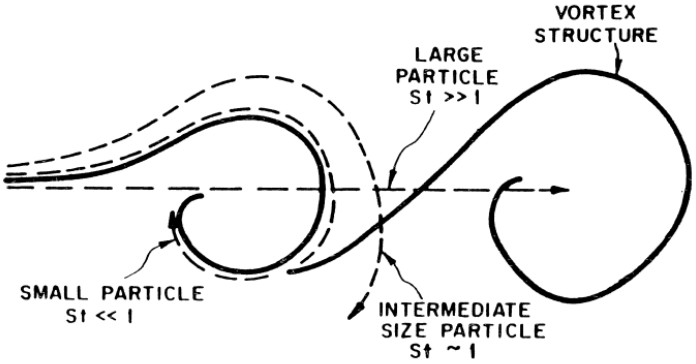

Source: Crowe, Troutt, and Chung (1995).

2.2.2 Dilute and dense regimes

The terms “dilute” and “dense” are often used to describe two distinct regimes of multiphase flows. These regimes are differentiated by the forces that control the motion of particles. The flow is dilute when the fluid-particle interaction forces, such as drag and buoyancy, are predominant in determining the trajectory of particles. Nevertheless, the flow is dense when particle motion is mostly influenced by particle-particle interaction forces.

As suggested by Crowe *et al.* (2011), the volume fraction can be used as a parameter to determine whether the flow regime is dilute or dense. The volume fraction is calculated by dividing the volume of the dispersed phase V_d by the total volume of the mixture V_m:

$$\Phi_p = \frac{V_d}{V_m} = \frac{1}{V_m}\sum_{n=1}^{N_p} V_{p,n}, \tag{2.4}$$

where N_p is the number of particles and V_p is the volume of a particle. According to Fig. 2.3, flows are considered dilute for volume fractions smaller than 10^{-3}. For volume fractions larger than 10^{-3}, the regime is dense and can still be classified as collision-dominated or contact-dominated. Thus, if particles collide with each other but the contact time is shorter than the time between collisions, the flow is dominated by interparticle collisions. However, if the volume fraction is specifically greater than 10^{-1}, the particles remain in constant contact, and consequently, the flow is contact-dominated.

Figure 2.3 – Flow regimes for dilute and dense flows.

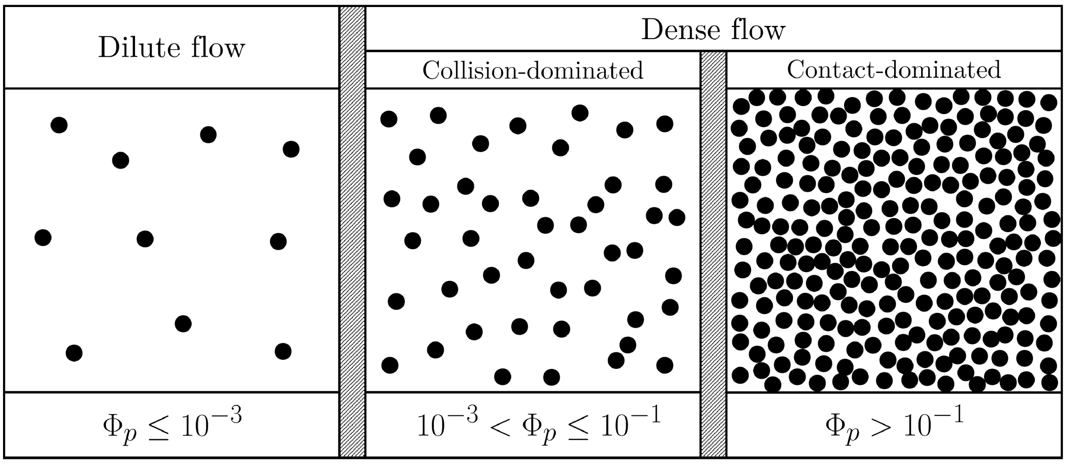

Source: Modified from Crowe *et al.* (2011).

2.2.3 Phase coupling

The coupling type in a multiphase flow is related to the degree of interaction between dispersed and continuous phases. Knowing whether the coupling is one-way, two-way, or four-way is very important in a multiphase flow simulation. Elghobashi (1994) then classified turbulent multiphase flows by interaction mechanisms using the volume fraction of the dispersed phase, as shown in Fig. 2.4.

Figure 2.4 – Regimes of interaction between phases.

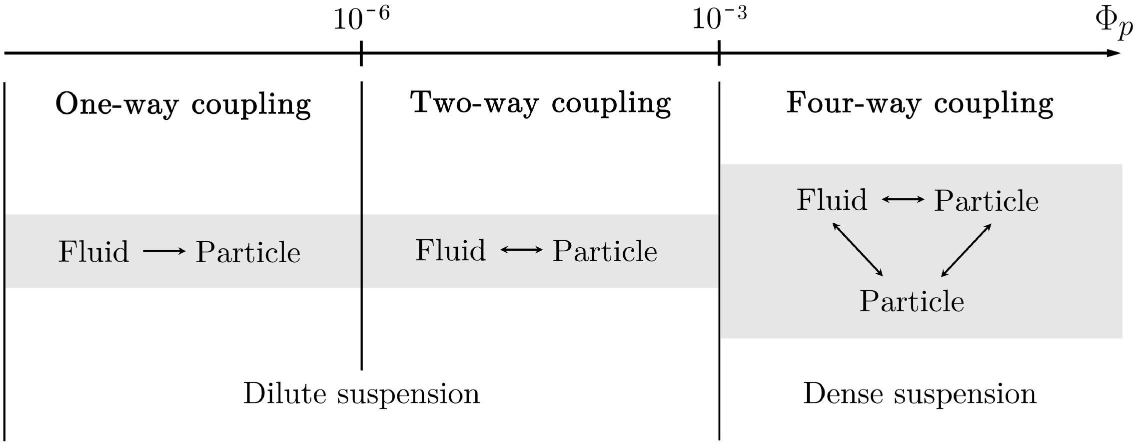

Source: Modified from Elghobashi (1994).

The mass loading η can also be useful to determine the coupling type (DUARTE; SOUZA; SANTOS, 2015). This parameter is defined by the ratio between the mass flow rates of particles $\dot{m}_p$ and fluid $\dot{m}$ (SOMMERFELD, 2017):

$$\eta = \frac{\dot{m}_p}{\dot{m}} = \frac{\Phi_p \rho_p U_p}{(1 - \Phi_p)\, \rho U}, \tag{2.5}$$

where ρ is the fluid density, and U_p and U are the average velocities in a given cross section of particles and fluid, respectively.

In one-way coupling ($\Phi_p \leq 10^{-6}$ or $\eta \ll 1$), the dispersed phase is assumed to be passively carried along by the continuous phase without significantly affecting the behavior of the carrier fluid. This means that the continuous phase is modeled independently of the dispersed phase, and the effects of the dispersed phase on the continuous phase are neglected. In two-way coupling ($10^{-6} < \Phi_p \leq 10^{-3}$ or $\eta \approx 1$), both the dispersed phase and the continuous phase are modeled together, and the effects of each phase on the other are taken into account. In other words, the behavior of the dispersed phase affects the behavior of the continuous phase, and vice versa. Lastly, four-way coupling ($\Phi_p > 10^{-3}$ or $\eta \gg 1$) is similar to two-way coupling, but with the addition of interactions between particles, which suggests that this type of coupling is especially observed in dense flows.

2.2.4 Simulation of multiphase flows

The two commonly used approaches to numerically solving multiphase flow problems are Euler-Euler and Euler-Lagrange. In the Euler-Euler approach, all phases are formulated based on the Eulerian description of the flow field. In the Euler-Lagrange approach, the continuous phase is defined in the Eulerian frame of reference, while the dispersed phase is defined in the Lagrangian frame of reference. Both approaches have their own advantages and limitations and are more suitable depending on the specific characteristics of the multiphase flow being modeled.

2.2.4.1 Euler-Euler approach

In the Euler-Euler approach, both phases are assumed to behave as interpenetrating continuous media, and they can either be modeled as a single fluid or as two fluids. One-fluid modeling is based on tracking the motion of the interface between separated phases (RIBERA, 2015; MIRJALILI; JAIN; DODD, 2017; GIBOU; FEDKIW; OSHER, 2018), for example, the VOF (volume of fluid) and LSM (level-set method) methods. In this method, the problem is solved by a set of PDEs as in single-phase flows, and an additional scalar field is applied to capture the interface. With the scalar field, which represents the volume fraction in the VOF method or the distance to the interface in the LSM method, the physical properties of each phase can be determined. Conversely, modeling dispersed multiphase flows is more appropriate with the two-fluid models.

In two-fluid models, each phase is assumed to be a continuum with its own set of transport equations (KUIPERS *et al.*, 1992). In addition, exchange terms that model momentum, mass, and energy transfer can be implemented to account for interactions, although not all the details that occur at the particle scale can be described and modeled. For dense flows, the use of this modeling is advantageous when compared with an Euler-Lagrange approach. Nevertheless, if particles have a size distribution, the transport equations must be solved for each size class, and, therefore, this modeling eventually becomes computationally expensive (ALLETTO, 2014).

Van Wachem *et al.* (2001) carried out a comparative analysis between some existing two-fluid models in the literature and in commercial CFD software through simulations of fluidized beds. The author observed that when comparing two different proposals for linear momentum equations, the results were similar in terms of the macroscopic characteristics of the flow. Furthermore, the results were not dependent on the different turbulence closure models for the solid phase. However, the different proposals to calculate the drag force considerably influenced the behavior of the multiphase flow.

2.2.4.2 Euler-Lagrange approach

In the Euler-Lagrange approach, the continuous phase is treated as a continuum, and the dispersed phase is treated as a collection of discrete particles with a specific position, velocity, and mass. This approach allows a very detailed description of the particle behavior, including all relevant mechanisms involved, such as body forces, fluid-particle interactions, particle-particle interactions, and particle-wall interactions.

A usual way to model the dispersed phase in the Euler-Lagrange approach is through the point-particle approximation, which means that particles are assumed to be material points. For this assumption to be valid, the particle size must be smaller than the grid size so that the disturbances caused in the continuous phase are contained within a cell (ALLETTO, 2014). This approximation relies on Newton's second law, which implies using a set of ordinary differential equations (ODEs) to track the motion of particles.

Sommerfeld (2017) suggested a classification for the point-particle approach as presented in Fig. 2.5. Some distinctions in tracking and modeling particles are observed. In the discrete particle method (DPM), for example, all real particles are tracked. Nevertheless, in cases where particles are many and tiny, tracking them all becomes computationally infeasible. Under these conditions, the Lagrangian parcel concept (LPC) is more advantageous, in which the simulated particles are called parcels and represent a certain number of real particles. Both in LPC and DPM, the hard sphere model is adopted, which is more effective in collision-dominated cases since it considers that only instantaneous collisions between pairs of particles happen. In the discrete element method (DEM), all real particles are tracked as in DPM, but instead of the hard sphere model, the soft sphere model is considered. In the soft sphere model, a particle can have contact with more than one particle at the same time, and it is assumed to be a deformable body that will return to its original shape after releasing the contact (NOROUZI *et al.*, 2016). This model is suitable for contact-dominated cases, allowing simulations of much denser flows than with DPM.

Figure 2.5 – Classification of Lagrangian particle tracking methods.

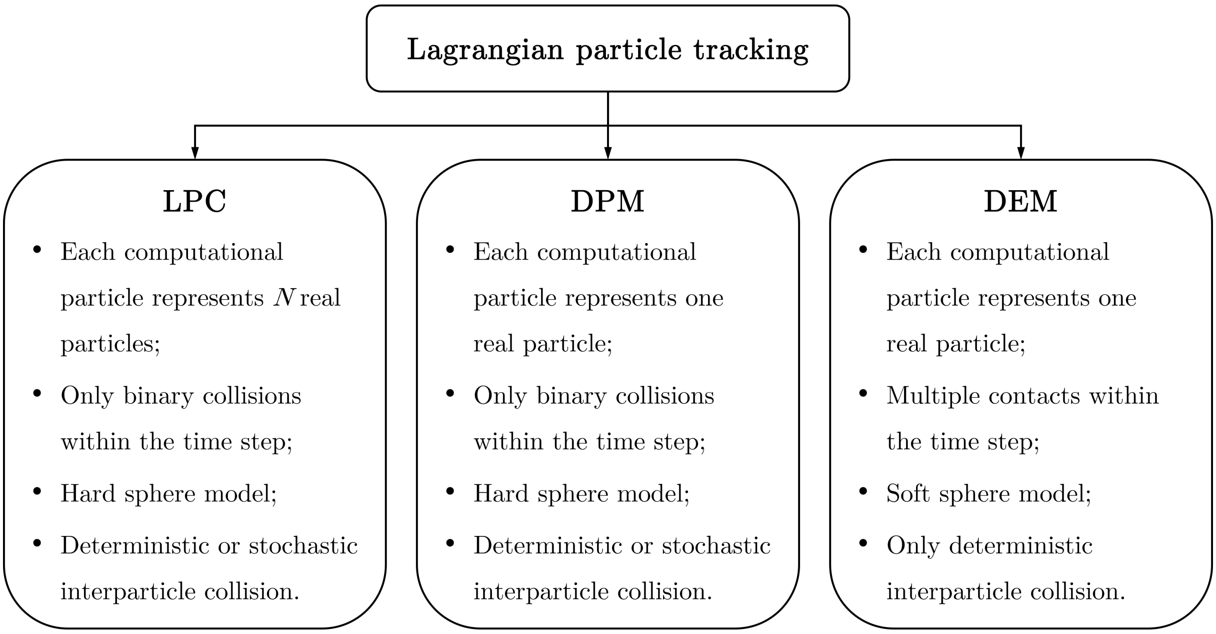

Source: Modified from Sommerfeld (2017).

2.2.5 Erosive wear due to particles

Erosive wear is a type of wear that occurs when a solid surface is subjected to the impact of particles of solid or liquid carried in a fluid flow. According to Bhushan (2013), the erosion caused by solid particles is a form of abrasion that is generally treated rather differently because the contact stress arises from the kinetic energy of particles flowing in a fluid stream as it encounters a surface. The particle velocity and impact angle combined with the size of the abrasive give a measure of the kinetic energy of the hitting particles, that is, of the square of the velocity.

Although erosion can be an advantage in certain practical uses, such as erosive cleaning of surfaces and erosive drilling and cutting, it can be a severe problem in other situations. Due to the high velocities required for conveying particulate materials, erosion of pipeline surfaces caused by solid particles in pneumatic conveying systems is a major industry concern, especially if abrasive particles have to be handled (DUARTE, 2017). Erosion can cause significant damage to the surface of equipment, leading to reduced functionality and a shorter service life. Thus, the search for solutions is something desired in the industry, and that is why studying this phenomenon is so important.

Understanding the physics involved requires determining the flow conditions, the number, direction, and velocity of particles striking the surface, as well as the surface material removed in the process. The erosion phenomenon is clearly defined as a fluid dynamics problem, with the fluid flow transporting particles that end up colliding with a surface (PEREIRA; SOUZA; MORO MARTINS, 2014).

The characteristics of the fluid flow have a strong effect on the final erosion rate. Some influencing factors are fluid properties, such as viscosity and density, and flow turbulence (SANTOS, 2018). In terms of viscosity, wear can be affected as drag forces imposed by a viscous flow on the erosive particles change the impact angles (HOJO; TSUDA; YABU, 1986). Furthermore, as can be seen in Fig. 2.6, particle impingement is more

Figure 2.6 – Effect of flow on erosive wear.

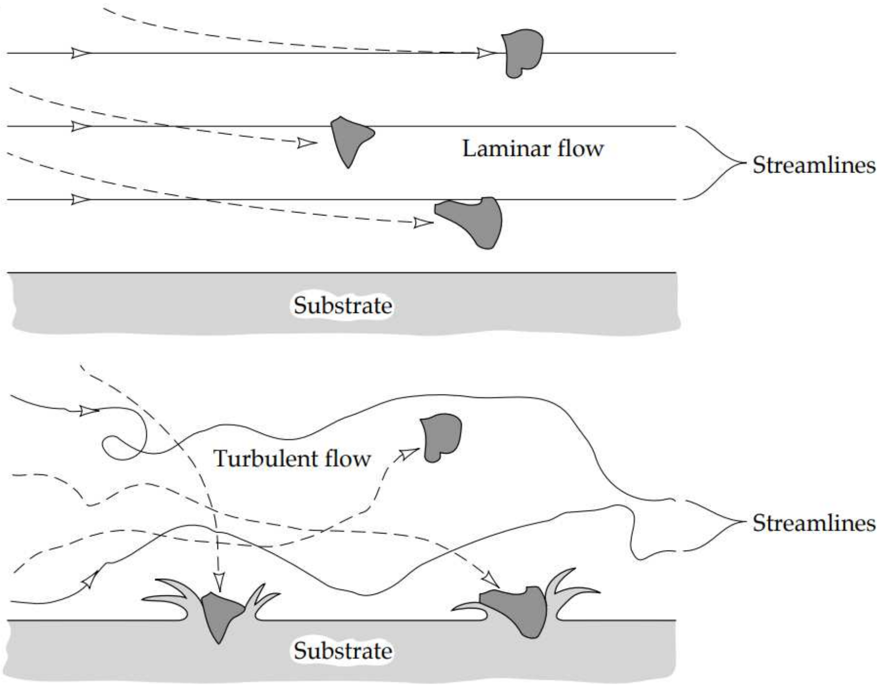

Source: Stachowiak and Batchelor (2014).

likely to occur in turbulent than in laminar flows, i.e., the presence of turbulence tends to accelerate erosive wear (DOSANJH; HUMPHREY, 1985). However, when a laminar jet is directed normally to the surface, the particles impinge against the surface. In this case, wear is concentrated directly beneath the jet, and a relatively unworn annular area surrounds the wear scar (STACHOWIAK; BATCHELOR, 2014).

The research community has made efforts to explore the topic of the erosion process in pipeline systems. Experimental investigations, by the way, have supported the development of empirical correlations and models capable of predicting erosion behavior (NEILSON; GILCHRIST, 1968; FINNIE, 1972; GRANT; TABAKOFF, 1975; HOJO; TSUDA; YABU, 1986; AHLERT, 1994; OKA; OKAMURA; YOSHIDA, 2005; ZHANG *et al.*, 2007; MAZUMDER; SHIRAZI; MCLAURY, 2008; RICARDO; SOMMERFELD, 2020). Regarding numerical investigations, progress in understanding erosion due to particles has been achieved by implementing these erosion models in CFD simulations (GRANT; TABAKOFF, 1975; DOSANJH; HUMPHREY, 1985; PEREIRA; SOUZA; MORO MARTINS, 2014; SOLNORDAL; WONG; BOULANGER, 2015; DUARTE; SOUZA; SANTOS, 2015; DUARTE *et al.*, 2017; YU, W. *et al.*, 2019). A complete review of the erosion equations developed over the years is found in Duarte (2017).

Neilson and Gilchrist (1968), Finnie (1972), Ahlert (1994), Oka, Okamura, and Yoshida (2005) and Zhang *et al.* (2007), for instance, proposed correlations to estimate the erosion ratio related to the impact of a particle on a surface. The erosion ratio E corresponds to the mass ratio of eroded material over erodent material. A common feature of these models is that, for a given pipe material and given particle parameters, the predicted erosion pattern is continuously dependent on the impact angle and impact velocity, as well as the amount of particles hitting the wall. Thus, by accumulating the damage that each particle causes when colliding, it is possible to calculate the mass of removed material per unit of area and per unit of time. This concept leads to the erosion rate:

$$E_f = \frac{1}{A_f} \sum_{\pi(f)} \dot{m}_{p,\pi} E, \tag{2.6}$$

where $\dot{m}_{p,\pi}$ is the particle mass flow rate represented by each computational particle colliding with face f, and A_f is the face area. Another way to formulate erosion is in terms of the penetration ratio, which represents the thickness of material removed from the wall over the mass of particles injected into the system:

$$\text{Penetration ratio} = \frac{E_f}{\dot{m}_{p,\text{in}}\,\rho_s}. \tag{2.7}$$

This parameter is obtained just by dividing the erosion rate by the surface material density ρ_s and particle mass flow rate at the inlet $\dot{m}_{p,\text{in}}$.

In pipeline systems, the erosion typically occurs at bended segments, where the particles do not immediately respond to the sudden change in the carrier flow direction due to their inertia. This problem is mainly simulated with the Lagrangian approach for tracking particles, and only a few studies (MESSA; FERRARESE; MALAVASI, 2015; MESSA; MALAVASI, 2018; YU, W. *et al.*, 2019) considered the Eulerian approach.

The mitigation of erosion by somehow modifying pipes has been studied previously. Duarte, Souza, and Santos (2016), for example, added a vortex chamber to a standard elbow and verified, through simulations, an improvement in the efficiency of the cushioning effect, reducing the peak of penetration ratio up to 93 %. Santos, Souza, and Duarte (2016) numerically investigated the insertion of twisted tape at different positions upstream of a bend with the intention of reducing elbow erosion. The authors found that the further the insertion is placed upstream of the elbow, the less erosion there is in the elbow. Similarly, Zhu and Li (2018) did not change the surface of the pipe but inserted a trapezoidal rib by installing it at different positions on the extrados of a 90° elbow. A reduction of the erosion peak in the elbow up to 31.4 % was achieved by placing the rib at 25°. In contrast, Duarte and Souza (2017) proposed a novel design consisting of twisting a pipe wall along the streamwise direction. This modification caused a reduction of the erosion peak in a standard elbow of up to 33 %. Finally, Li *et al.* (2022) evaluated different arrangements of protuberances installed on the extrados of an elbow to improve its erosion resistance. It was observed that multiple rows of protrusions have a better effect, reducing the maximum erosion rate by 39.09 % at most.

2.3 Shape optimization of fluid dynamics systems

Optimization is the process of obtaining the most suitable solution to a given problem. While some types of problems may have a unique solution, others may have multiple potential solutions. The goal of optimization is to find the "best" solution, where "best" implies that the solution is not the exact solution but is sufficiently superior.

In this sense, shape optimization is a branch of optimal control theory that consists of geometrically controlling the shape of a system in order to improve its performance. The search for an optimal shape β is accomplished by minimizing a certain objective function J while satisfying the imposed constraints $\mathcal{R}$. From a fluid dynamics point of view, the evaluation of the objective function is subject to the solution of PDEs defined in a fluid domain Ω with boundary conditions defined on domain boundaries Γ:

$$\begin{aligned} &\text{minimize} \quad && J(\beta, \phi) \\ &\text{subject to} \quad && \mathcal{R}(\beta, \phi) = 0 \quad \text{in} \quad \Omega. \end{aligned} \tag{2.8}$$

Since the fluid flow is denoted as state ϕ, $\mathcal{R} = 0$ corresponds to the equations of state, i.e., the fluid dynamics equations. Although, in shape optimization problems, the control is applied to a part of the domain boundary $\Gamma_{\mathrm{D}} \subset \Gamma$ (boundary-based control), called the design surface, the objective function can be declared either on the objective surface $\Gamma_{\mathrm{O}} \subset \Gamma$ (boundary-based objective) or in the objective volume $\Omega_{\mathrm{O}} \subset \Omega$ (volume-based objective).

Shape optimization has a long history since Newton was looking several centuries ago for axisymmetric bodies with minimum drag in a fluid. Not so long ago, Hadamard, at the end of the 19th century, was able to formulate the differential of functions of the solution of some partial differential equations with respect to boundary variations (GLOWINSKI, 1998). In terms of the computational aspects, after the 1970s, the emergence of new approaches and techniques enabled a breakthrough in shape optimization (LIONS, 1971; PIRONNEAU, 1974; JAMESON, 1988). Early applications are primarily found in aerodynamic design (GLOWINSKI; PIRONNEAU, 1975, 1976) and structural optimization (HAFTKA; GRANDHI, 1986).

In the aeronautical industry, one of the main concerns is drag. This force acts in the opposite direction to an aircraft's motion, so the aircraft can fly more efficiently by reducing it, resulting in lower fuel consumption and lower operating costs. The desire to minimize drag and obtain more aerodynamic aircraft has motivated numerous research studies on shape optimization, making it well established in aerodynamic design (SKINNER; ZARE-BEHTASH, 2018). Its use has spread to a wide variety of physical and engineering disciplines. Regarding fluid dynamics systems, some of the more recent works include the optimization of cars and automotive components (HINTERBERGER; OLESEN, 2011; OTHMER, 2014), ships (STÜCK; KRÖGER; RUNG, 2011; KRÖGER; KÜHL; RUNG, 2018), cyclones (SAFIKHANI *et al.*, 2011; ELSAYED, 2015), turbomachinery blades (WANG; HE, 2010; MONTANELLI, 2013), ducts (OTHMER, 2008; AVVARI; JAYANTI, 2013), microchannels in inkjet printers (KUNGURTSEV; JUNIPER, 2019), and polymer distributors (HOHMANN; LEITHÄUSER, 2019b). There are still applications in other fields, such as the optimization of electrical motors (GANGL *et al.*, 2015), acoustic signal horns (BÄNGTSSON; NORELAND; BERGGREN, 2003; SCHMIDT; WADBRO; BERGGREN, 2016), and magnetic induction tomography (HINTERMÜLLER; LAURAIN; YOUSEPT, 2015).

Shape optimization problems are usually solved by iterative methods, starting with an initial estimate of the shape of a geometry, which can be referred to as the baseline configuration. As the iterations advance, i.e., for each new design cycle, this shape is gradually modified until a minimum of the objective function is achieved. Clearly, just applying an optimization method is not enough; the geometry must change in some way throughout the process. In principle, this can be done with the geometric representation by means of a parameterized surface (QUAGLIARELLA; CIOPPA, 1995). The parameterization can even be performed by coupling computer-aided design software (CAD) to optimization (YU, G. *et al.*, 2011; AGARWAL *et al.*, 2019). However, when a code based on a numerical discretization method, such as finite difference, finite element, or finite volume, is applied to solve the PDEs, the geometry of the problem is defined by a mesh. Therefore, if the shape of the geometry changes, the mesh must be modified for the optimization process to continue. One option for this scenario would be to re-mesh whenever the geometry is updated, but this is not always a feasible option due to the high computational cost. Consequently, applying a mesh deformation approach may be more appropriate.

Considering the problem is numerically solved by using a mesh with N computational cells, Eq. (2.8) can be rewritten in discrete form as:

$$\begin{aligned} &\text{minimize} \quad J(\underline{\beta}, \underline{\phi}) \\ &\text{subject to} \quad \mathcal{R}_j(\underline{\beta}, \underline{\phi}) = 0, \quad j = 1, \ldots, N. \end{aligned} \tag{2.9}$$

As well as the constraints, the state variables and the control are evaluated in the cells of the domain:

$$\begin{aligned} &\underline{\beta} = (\beta_1, \ldots, \beta_M), \\ &\underline{\phi} = (\phi_1, \ldots, \phi_N). \end{aligned} \tag{2.10}$$

Thus, based on information of the flow field resolved in a domain bounded by the shape of its surface, the objective function is evaluated (STÜCK, 2011):

$$\text{Set } \underline{\beta} \quad \rightarrow \quad \text{Solve } \mathcal{R}_j(\underline{\beta}, \underline{\phi}) = 0 \text{ for } \underline{\phi} \quad \rightarrow \quad \text{Evaluate } J(\underline{\beta}, \underline{\phi}) \tag{2.11}$$

It is important to note that no optimization procedure guarantees the global optimum of the objective function will be found, since the process may not converge or only converge towards a locally optimal solution. Typically, in this situation, there are three possibilities: restart the optimization process to investigate if the same solution is found; approach the optimization with a different algorithm to compare solution quality; or accept the optimum found, knowing that while it is superior to the baseline configuration, it may not be the optimal solution (SKINNER; ZARE-BEHTASH, 2018). Further insights into optimization methods and their limitations are provided in the subsequent sections.

2.3.1 Optimization methods

The field of optimization is expansive, and although computational cost is important, the choice of a suitable algorithm also depends on the nature of the problem at hand, i.e., number and type of design variables, design scope and required fidelity, how constraints are handled in the optimization process, and how the algorithm should be embedded and tuned (SKINNER; ZARE-BEHTASH, 2018). Basically, the optimization methods are divided into two techniques: deterministic or classical optimization and heuristic or random optimization (SARAMAGO, 2012; LOBATO, 2008).

The classical optimization relies on the gradient (derivatives) information of the objective function with respect to a number of independent variables to identify the search direction of the design. An understanding of the design space is necessary, as a properly preconceived initial design point must be provided. Gradient-based algorithms are well suited to finding locally optimal solutions but may struggle to find the global optimal.

On the other hand, heuristic optimization operates from a completely different paradigm, often mimicking the behavior of natural systems (e.g., population genetics, biological evolution, particle swarm and simulated annealing) or other analogies. This technique is based on the calculation of probabilities and does not require the calculation of derivatives, which allows it to cope with discontinuous and numerically noisy objective functions. Gradient-free algorithms can prove more complex to implement than gradient-based ones, but they generally increase the probability of finding the global optimum.

Typically, the computational cost of the entire shape optimization process scales with the number of design variables and also depends on how the equations of state are solved. When optimizing fluid dynamics systems, computational cost plays a crucial role in selecting an appropriate optimization method. Given that CFD simulations are used to solve the fluid dynamics problem, a significant cost is already involved, especially if it is a complex three-dimensional problem.

The great disadvantage of heuristic methods for fluid dynamics systems is related to the high number of evaluations of the objective function, as they operate over a population of individuals. At each evaluation of the objective function, the flow field would need to be solved once, which results in several CFD simulations within a single iteration of the optimization process. Skinner and Zare-Behtash (2018) provided a critical review of aerodynamic shape optimization methods. The authors concluded that the cost of heuristic relative to classical methods increases dramatically, and they normally require tighter convergence tolerances. In aerodynamic optimizations with gradient-free algorithms, overcoming the computational cost was often done by applying a compact shape parameterization, or, in other words, a parameterization with a compact set of design variables, in order to reduce the dimensionality of the search space (SKINNER; ZARE-BEHTASH, 2018).

For classical methods, the computational cost is estimated based on the calculation of derivatives of the objective function. In shape optimization, obtaining the gradient consists of finding variations in the objective function δJ for a given perturbation of the design surface. This process is called sensitivity analysis, in which a perturbation of the design surface means changes in the design variables $\delta\beta$ and compatible changes in the flow field $\delta\phi$. Accordingly, the gradient is also referred to as sensitivity derivatives, or just sensitivities.

Together with the CFD simulation, the sensitivity analysis must be embedded in a single design procedure containing an optimization routine or strategy and tools for (automatic) geometry update, mesh adaptation, or re-meshing. Sensitivity derivatives can support both manual and automatic optimization, but manual optimization is not practical at all as it makes the whole procedure laborious, cumbersome, and very time-consuming. In this context, two methods stand out for sensitivity analysis: direct methods and adjoint methods.

The direct methods follow the straightforward chain of influence shown in Eq. (2.11). Computing the gradient for such methods requires varying each one of the design variables to obtain the respective objective function. However, a variation in each design variable requires a new solution for the flow field. Consequently, the number of CFD simulations in a single design cycle of the optimization process scales linearly with the number of design variables.

In contrast, the adjoint methods follow the opposite path of Eq. (2.11). They are focused on determining the required variation of the design variables for a desired variation in the objective function. Although the computational cost is practically independent of the number of design variables, a new system of partial equations, the adjoint equations, needs to be deduced (STÜCK, 2011). Thus, the complete computation of the gradient for a given objective function is accomplished with the effort of two CFD simulations. One simulation is intended to solve the conventional (primal) flow field and the other to solve the adjoint field. If the problem had more than one objective function, a different adjoint field would need to be solved for each function in addition to the primal flow field. A comparison between adjoint and direct methods considering one objective function can be seen in Fig. 2.7.

Figure 2.7 – Comparison of direct and adjoint methods considering one objective function.

Direct methods

Question: How do changes of the design variables $(\beta_1, \beta_2, \beta_3, ..., \beta_M)$ influence the system performance?

$$\begin{aligned} \delta\beta_1 &\rightarrow \delta J_{(1)} \\ \delta\beta_2 &\rightarrow \delta J_{(2)} \\ \delta\beta_3 &\rightarrow \delta J_{(3)} \\ &\vdots \\ \delta\beta_M &\rightarrow \delta J_{(M)} \end{aligned}$$

M + 1 required simulations

Adjoint methods

Question: What changes to the design variables are necessary to get an optimal system performance?

$$\{\delta\beta_1, \delta\beta_2, \delta\beta_3, ..., \delta\beta_M\} \rightarrow \delta J_{(optimal)}$$

2 required simulations
(1 primal + 1 adjoint)

Source: Modified from Brenner *et al.* (2015).

For CFD-based optimization, the simplest methods for geometry shape definitions are the deformative ones (SKINNER; ZARE-BEHTASH, 2018), in which the mesh is deformed as the boundary is modified. In deformative methods, the mesh nodes on the boundary of the domain are directly treated as design variables, and their position can be perturbed by the optimizer in order to generate new shapes. Therefore, a significant advantage of this method is that the solutions are more flexible, as the optimized shapes are not limited to parameterized surfaces. Any feasible geometry can be generated; however, this is likely to require a large number of design variables. As the adjoint methods are very capable of handling thousands of design variables, they can be more suitable and promising for optimizing fluid dynamics systems.

2.3.2 Adjoint methods

The adjoint methods are classified into two different approaches: continuous and discrete. The continuous approach consists of deducing the adjoint equations from the primal PDEs of the problem and discretizing them to obtain the discrete adjoint equations. Conversely, the discrete approach starts with the primal equations already discretized in order to obtain the discrete adjoint equations. A schematic representation of the steps of each approach is presented in Fig. 2.8.

Figure 2.8 – Schematic representation of the steps of the adjoint method approaches.

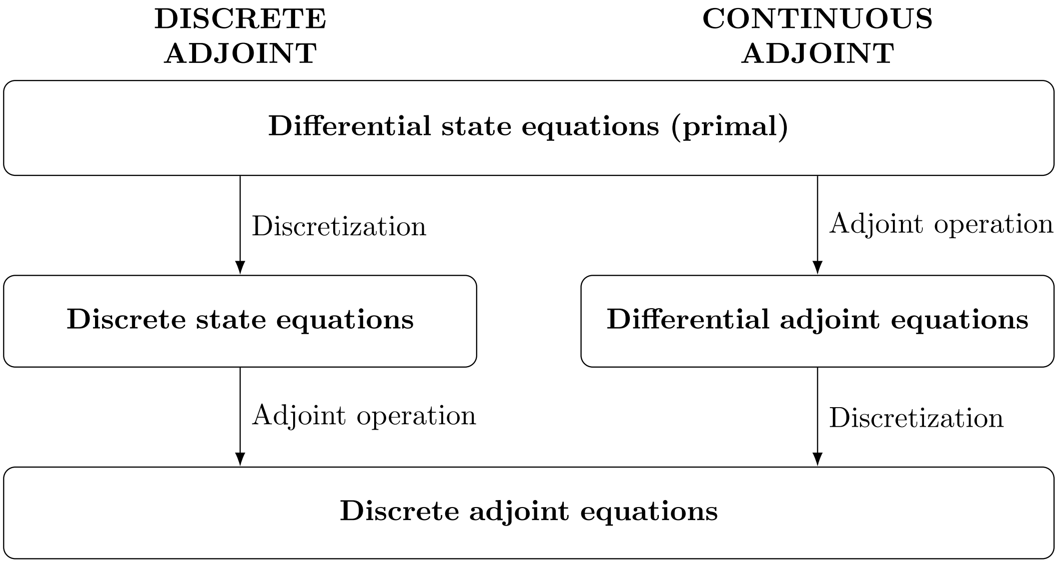

Source: Modified from Thévenin and Janiga (2008).

Both approaches have been successfully applied to the optimization of systems and equipment involving fluids in the last two decades. The pioneering works are normally attributed to Pironneau (1973, 1974), who studied drag minimization for two-dimensional shapes in Stokes and low-Reynolds number flows, and Jameson (1988), who was the first to apply the continuous adjoint method to transonic inviscid flow. The subsequent body of work of this last author with his students and colleagues is largely responsible for the widespread and popular application of these methods (REUTHER *et al.*, 1996; JAMESON; MARTINELLI; PIERCE, 1998; NADARAJAH; JAMESON, 2000). Reuther *et al.* (1996), for example, used the continuous adjoint method in the shape optimization of an aircraft and showed that accurate results can be obtained with it. Nadarajah and Jameson (2000) compared the continuous and discrete adjoint-based automatic aerodynamic optimization, focusing on studying the complexity of discretization, accuracy of results, and computational cost. The main conclusions of the authors were considered and will be outlined at the end of this section. Kim *et al.* (2001), on the other hand, considered the discrete approach in optimizing the design of an aircraft wing exposed to supersonic transport, confirming the validity and efficiency of the method. Othmer (2008) derived an adjoint formulation for the steady-state incompressible Navier-Stokes equations specialized to ducted flows, emphasizing the versatility of the formulation since the adjoint equations for ducted flows are objective function independent by nature and the adjoint boundary conditions have been expressed in a way that can be easily adapted to any commonly used objective function. Aiming to optimize automotive exhaust systems, Hinterberger and Olesen (2011) employed a continuous approach, disregarding density and viscosity variations of the flow. Although the authors agree that this consideration reduces the accuracy of the calculated gradients, in their opinion, the adjoint method still provides valuable information that allows even manual adjustments of the geometry. Stück, Kröger, and Rung (2011) considered the sensitivity analysis based on the adjoint method applied to the RANS equations for incompressible flows in order to redesign the hull of a ship. In this case, the authors were interested in improving the wake quality left by the ship, and with only two redesign cycles, they were able to obtain an improvement of approximately 10 %. Othmer (2014) addressed the achievements and challenges that have been encountered by researchers in collaboration with the automotive industry seeking to develop an industrially viable adjoint solver for car applications. Some of the obtained results have proven to be promising, leading the author to state that shape optimization methods will have an impact on the overall performance and consumption of cars in the future. Finally, Elsayed (2015) used a discrete adjoint solver to guide geometry modifications based on the Stairmand cyclone, and, after shape optimization, the new cyclone improved the flow symmetry.

When deriving the adjoint equations for turbulent flows, the turbulence closure model equations are often disregarded in the mathematical development. As pointed out by Dwight and Brezillon (2006), one of the most demanding parts of the spatial discretization to differentiate by hand is the turbulence closure model, partly due to the wide variety of blending functions, limiters, etc., but mainly because of the many coupling points to the fluid dynamics equations and the enormous selection of models available. Moreover, it is very difficult to treat turbulence closure models in a continuous adjoint framework. Hence, some simplifying assumptions must be made. A common approximation is to neglect the variation of the effective viscosity of the flow, which is known as the "frozen turbulence" hypothesis. Dwight and Brezillon (2006) studied the feasibility of this hypothesis for aerodynamic design optimization using an adjoint method. The authors concluded that assuming a constant effective viscosity might be invalid in the adverse pressure gradient region following the shock on a transonic airfoil. However, Kim, Kim, and Rho (2003) noticed that even causing inaccurate gradients in the design of the transonic airfoil with a strong shock wave, this assumption showed a minor difference in obtaining an optimal value of the objective function compared to the application without it. Despite a certain increase in complexity, some works have proposed formulations taking into account the effect of turbulence in the adjoint equations. For instance, Zymaris *et al.* (2009) and Gkaragkounis, Papoutsis-Kiachagias, and Giannakoglou (2018) presented the development of the continuous approach considering the Spalart-Allmaras turbulence model applied to an aerodynamic and a conjugate heat transfer problem, respectively.

Adjoint methods have already been applied to multiphase flows, but this remains limited to a few contributions. Extending shape optimization of single-phase to multiphase flow systems has generally been difficult due to the inclusion of more equations that can be time-dependent. A time-dependent adjoint solution points backward in time and is linearized around the current primal flow solution. Thus, the attractiveness of adjoint methods reduces for the optimization of unsteady flows due to memory requirements to record the complete time history of the primal problem (KRÖGER; KÜHL; RUNG, 2018). Besides that, when addressing multiphase problems within the framework of PDE-constrained shape optimization, the Lagrangian particle tracking approach is not well suited. In the Lagrangian approach, the individual trajectories of a number of representative particles are described by a set of ODEs. Instead, the Eulerian approach provides information about the spatial distribution of the flow variables on the entire domain and not on a discrete number of particle trajectories only. Although Eulerian models are less prevalent in this context, they are a better option for shape optimization.

Helgason and Krajnović (2014) presented a sensitivity analysis aiming to maximize particle uniformity at the outlet of a two-dimensional channel. The particle distribution in a flow was represented by a passive scalar transport equation, and simulations were performed in an open-source finite volume solver. The authors compared the sensitivity derivatives calculated using the continuous adjoint method with the numerical differentiation, and the same trend was obtained. In Boger and Paterson (2014), a continuous adjoint formulation for multiphase flow was developed based on a barotropic homogeneous mixture model and discretized with standard explicit Runge-Kutta methods. Results were presented for vapor minimization objective functions for a two-dimensional cavitating hydrofoil in which the geometry was parameterized using B-splines. It is worth mentioning that in both the works of Helgason and Krajnović (2014) and Boger and Paterson (2014), no shape optimization was performed. Kröger, Kühl, and Rung (2018) studied the hydrodynamic optimization of ships for drag reduction. The authors extended the idea of the adjoint method to the application of the VOF method using a finite volume solver. They obtained an optimized ship design, keeping the main dimensions, with a reduction of more than 5 % of the total drag. In Hohmann and Leithäuser (2019a), the shape optimization of a bended tube minimizing particle erosion was investigated. The non-dimensionalized, stationary, incompressible, isothermal Navier-Stokes equations were considered for laminar fluid flow, and the one-way coupled Eulerian model based on the volume averaging procedure was considered for particle transport. The shape derivative was formulated using the continuous adjoint approach, and the problem was solved in a code based on the finite element method. In order to optimize, a volume mesh deformation and a gradient descent method were applied. Regarding the results, the erosion rate on the optimized bend was less spatially concentrated than on the initial geometry, and its maximal value was reduced by 79 %. Bonnet *et al.* (2023) presented an adjoint-based optimization approach for finding the optimal shapes of peristaltic pumps transporting a rigid particle in Stokes flow. The authors applied boundary integral equation techniques to solve the PDE equations. The contribution of this work was an adjoint formulation that, in conjunction with a boundary integral formulation, significantly reduced the computational effort of evaluating shape derivatives for the case studied.

Concerning the aforementioned works, most used the continuous adjoint approach applied to a multiphase flow. None of them resorted to a Lagrangian approach to treat particle transport. In fact, in the work of Kröger, Kühl, and Rung (2018), the flow consisted of two immiscible, incompressible phases. Furthermore, only two works (HELGASON; KRAJNOVIĆ, 2014; KRÖGER; KÜHL; RUNG, 2018) discretized the adjoint equations with the finite volume method. Ultimately, the particle transport equations have not yet been addressed in shape optimization using adjoint formulations implemented in a finite volume CFD code.

The PDE-constrained problem for shape optimization can be solved by converting it to an unconstrained problem. In adjoint methods, this issue is tackled by reformulating the objective function J with the introduction of the Lagrange function L. Then, this new function is defined as the objective function extended by the domain integral of primal equations, which are the constraints $\mathcal{R}$, weighted by the Lagrange multipliers. The Lagrange multipliers are also called the adjoint variables $\hat{\phi}$. To better understand the specifics of each adjoint approach, the mathematical formulations of the continuous and discrete approaches are exposed separately below.

2.3.2.1 Continuous approach

According to the continuous approach, the Lagrange function is given by:

$$L = J + \int_{\Omega} \hat{\phi} \mathcal{R} \, \mathrm{d}\Omega, \tag{2.12}$$

with the objective function defined in a general form as:

$$J(\beta, \phi) = \int_{\Gamma_\mathrm{O}} J_\Gamma \, \mathrm{d}\Gamma + \int_{\Omega_\mathrm{O}} J_\Omega \, \mathrm{d}\Omega. \tag{2.13}$$

A variation of L comprises three different contributions. Firstly, there are local variations $\delta_\phi L$ of the flow properties at the old (original) position. Secondly, convective variations $\delta_\beta L$ arise from the position change within the old flow field. Lastly, geometric variations occur due to the change of geometric properties. Validation studies conducted by Stück (2011) showed that the geometric variation is of minor importance for the predictive accuracy of the sensitivities and can be neglected, so:

$$\delta L = \delta_\beta L + \delta_\phi L. \tag{2.14}$$

Along the design boundaries Γ_D, all contributions have to be considered. Along the remaining boundaries and in the interior domain, the state is only exposed to local variations (KRÖGER; KÜHL; RUNG, 2018). Therefore:

$$\delta L = \int_{\Gamma_\mathrm{O} \cap \Gamma_\mathrm{D}} \delta_\beta J_\Gamma \, \mathrm{d}\Gamma + \int_{\Gamma_\mathrm{O}} \delta_\phi J_\Gamma \, \mathrm{d}\Gamma + \int_{\Omega_\mathrm{O}} \delta_\phi J_\Omega \, \mathrm{d}\Omega + \int_\Omega \hat{\phi} \delta \mathcal{R} \, \mathrm{d}\Omega. \tag{2.15}$$

After obtaining the variation of the primal equations $\delta\mathcal{R}$, the variational form is subjected to the integration by parts that shifts derivatives from the variation of state variables to the adjoint variables. Consequently, the volume integrals immediately yield to the adjoint equations. Part of the surface integrals yields the boundary conditions, and the other part related to the design surface remains to determine the gradient equation. Based on the information of the resolved primal field ϕ and adjoint field $\hat{\phi}$, the gradient G required in the optimization can be estimated from:

$$\delta L = G \delta\beta. \tag{2.16}$$

2.3.2.2 Discrete approach

In the discrete approach, the Lagrange function is constructed as:

$$L = J(\underline{\beta}, \underline{\phi}) + \sum_{j=1}^{N} \hat{\phi}_j \mathcal{R}_j(\underline{\beta}, \underline{\phi}). \tag{2.17}$$

The problem formulated in Eq. (2.9) implies that:

$$\frac{\partial L}{\partial \hat{\phi}_j} = 0, \qquad j = 1, ..., N. \tag{2.18}$$

Accordingly, the linear variation of the discrete Lagrange function is obtained from the expansion of the truncated Taylor series around $(\underline{\beta}, \underline{\phi})$:

$$\delta L \approx \left[\sum_{k=1}^{M} \delta\beta_k \frac{\partial L}{\partial \beta_k} + \mathcal{O}\left(\sum_{k=1}^{M} \delta{\beta_k}^2 \right) \right] + \left[\sum_{i=1}^{N} \delta\phi_i \frac{\partial L}{\partial \phi_i} + \mathcal{O}\left(\sum_{i=1}^{N} \delta{\phi_i}^2 \right) \right] \tag{2.19a}$$

$$= \sum_{k=1}^{M} \delta\beta_k \left(\frac{\partial J}{\partial \beta_k} + \sum_{j=1}^{N} \hat{\phi}_j \frac{\partial \mathcal{R}_j}{\partial \beta_k} \right) + \sum_{i=1}^{N} \delta\phi_i \left(\frac{\partial J}{\partial \phi_i} + \sum_{j=1}^{N} \hat{\phi}_j \frac{\partial \mathcal{R}_j}{\partial \phi_i} \right). \tag{2.19b}$$

If $\hat{\underline{\phi}}$ is chosen to satisfy the adjoint equations obtained by:

$$\sum_{j=1}^{N} \hat{\phi}_j \frac{\partial \mathcal{R}_j}{\partial \phi_i} = -\frac{\partial J}{\partial \phi_i}, \qquad i = 1, ..., N, \tag{2.20}$$

the second term of Eq. (2.19) is eliminated, and then δL can be calculated for arbitrary admissible $\delta\underline{\phi}$:

$$\delta L = \sum_{k=1}^{M} \delta\beta_k \left(\frac{\partial J}{\partial \beta_k} + \sum_{j=1}^{N} \hat{\phi}_j \frac{\partial \mathcal{R}_j}{\partial \beta_k} \right). \tag{2.21}$$

Equation (2.20) contains the transpose of the Jacobian matrix of the system, $\partial \mathcal{R}_i / \partial \phi_j$. With the solution of $\hat{\underline{\phi}}$ from Eq. (2.20), the gradient or the sensitivity derivatives can be determined by:

$$G = \frac{\partial J}{\partial \beta_k} + \sum_{j=1}^{N} \hat{\phi}_j \frac{\partial \mathcal{R}_j}{\partial \beta_k}, \qquad k = 1, ..., M. \tag{2.22}$$

2.3.2.3 Particularities

The two approaches of the adjoint method have advantages and disadvantages. Choosing the continuous or discrete approach usually depends on priorities for some specific reason or limitations due to practical reasons. Based on some works present in the literature (REUTHER *et al.*, 1996; NADARAJAH; JAMESON, 2000; MAVRIPLIS, 2007; AUVINEN, 2014), the characteristics of both approaches are listed below.

For the discrete adjoint method, the highlights are:

- The obtained sensitivity derivatives present better agreement with those obtained through the direct methods, independently of the mesh refinement;

- Due to the above-mentioned fact, the discrete approach maintains algebraic consistency;
- The boundary conditions already appear as source terms in the adjoint equations;
- The implementation of the discrete adjoint equations is relatively simple when automatic differentiation tools are employed;
- It is more computationally intensive.

Automatic differentiation (AD) is a set of techniques for evaluating the derivatives of numerical functions expressed as computer programs. Knowing that every computer program executes a sequence of elementary arithmetic operations (e.g., addition, subtraction, multiplication, and division) and elementary functions (e.g., exp, log, sin, and cos), derivatives of arbitrary order can be computed automatically by repeatedly applying the chain rule to these operations. This tool has been widely used in the discrete adjoint method to calculate the terms $\partial \mathcal{R}_j / \partial \phi_i$ and $\partial \mathcal{R}_j / \partial \beta_k$ that appear in Eq. (2.20) and Eq. (2.22), respectively (LE MOIGNE, 2002). However, not all source code can be differentiated with the help of an AD tool, and without it, the implementation process tends to be expensive, since performing the differentiation manually is difficult, time-consuming, and tends to generate complicated code to maintain and debug (AUVINEN, 2014).

As for the continuous adjoint method:

- The obtained sensitivity derivatives tend to show better agreement with those obtained by direct methods for increasingly refined meshes;
- The adjoint boundary conditions appear as updates of the adjoint field after the adjoint equations are resolved;
- A certain effort is required in the mathematical development, so for problems involving more complex equations, it becomes more difficult to make the necessary deduction;

- With the continuous formulation, it is possible to extract the adjoint analytical solution of the problem, which allows to study the characteristics of the equations and even use them to validate the computational results;
- There is greater flexibility in the discretization stage;
- The continuous adjoint solver can leverage features of the primal solver code more freely.

CHAPTER III

SINGLE-PHASE FLOW OPTIMIZATION PROBLEM

This chapter provides a comprehensive overview of the use of shape optimization in the context of single-phase flow. Shape optimization can be applied to control the shape design of fluid dynamics systems to improve their performance or achieve specific flow characteristics.

The challenge in this context is to compute the gradient of fluid dynamics objectives in the adjoint way, ensuring that the computational effort is independent of the number of parameters involved. Therefore, an adjoint method is used to optimize the shape of three pipe fittings commonly found in pipelines of process industries with the goal of minimizing the total pressure losses of the flow.

Considering that the shape optimization will be applied to an existing and validated CFD code and taking into account the advantages and disadvantages of different adjoint approaches, the continuous adjoint method was chosen. The continuous approach results in adjoint equations that resemble the primal equations of fluid flow. Consequently, the primal solver can be easily used to create the adjoint solver with only minor adjustments. Although developing the adjoint equations may require more effort, the continuous approach offers a more intuitive understanding.

3.1 Mathematical modeling

The mathematical modeling for the fluid flow problem is described below. The respective adjoint equations for the constrained optimization problem are then deduced, in addition to the adjoint boundary conditions. This leads to the calculation of the gradient of the objective function, which plays a crucial role in determining the direction of design improvement in the optimization process. Before considering the objective function of the loss in total pressure, the adjoint formulation is developed in a general form.

3.1.1 Fluid phase equations

The Navier-Stokes (linear momentum) equations with the continuity equation are sufficient to model an isothermal fluid flow in both laminar and turbulent regimes. However, direct numerical simulation of a turbulent flow requires the use of very fine meshes to resolve all turbulent structures. As a consequence, a high computational cost is imposed, limiting the application of DNS to simulate flows with a high Reynolds number.

The continuity and the Navier-Stokes equations in indicial notation for incompressible flows are, respectively, given by:

$$\frac{\partial(\rho u_i)}{\partial x_i} = 0, \tag{3.1}$$

$$\frac{\partial(\rho u_i)}{\partial t} + \frac{\partial(\rho u_i u_j)}{\partial x_j} = -\frac{\partial p}{\partial x_i} + \frac{\partial}{\partial x_j}\left[\mu\left(\frac{\partial u_i}{\partial x_j} + \frac{\partial u_j}{\partial x_i}\right)\right], \tag{3.2}$$

where i and $j = 1, 2, 3$ correspond to the components of the three coordinate directions (x, y, z) and u is the instantaneous fluid velocity.

Even with the evolution of hardware, the values of the Reynolds number, for which the practice of DNS is feasible, are still modest relative to the values that characterize flows in industrial applications. For this purpose, other methodologies for simulating turbulent flows may be a better choice. Employing the concept of filtering, the spectrum of turbulent structures of the flow can be decomposed into two bands. Reynolds and Boussinesq proposed to apply the time average operator $(\bar{\ })$ to the Eqs. (3.1) and (3.2).

Since the time average operator and the partial derivative operators are linear, it can be deduced that (SILVEIRA NETO, 2020):

$$\frac{\partial(\rho \bar{u}_i)}{\partial x_i} = 0, \tag{3.3}$$

$$\frac{\partial(\rho \overline{u_i u_j})}{\partial x_j} = -\frac{\partial \bar{p}}{\partial x_i} + \frac{\partial}{\partial x_j}\left[\mu\left(\frac{\partial \bar{u}_i}{\partial x_j} + \frac{\partial \bar{u}_j}{\partial x_i}\right)\right]. \tag{3.4}$$

The above equations still cannot be solved directly because of the nonlinear term $\overline{u_i u_j}$ that appears in Eq. (3.4). The decomposition of the total velocity field proposed by Reynolds and Boussinesq is then considered:

$$u_i = \bar{u}_i + u_i', \tag{3.5}$$

with $\bar{u}_i$ being the mean and u_i' the fluctuation of the velocity field. Upon substitution of Eq. (3.5) into Eq. (3.4) and performing the appropriate mathematical manipulations, it can be obtained that:

$$\frac{\partial(\rho \bar{u}_i \bar{u}_j)}{\partial x_j} = -\frac{\partial \bar{p}}{\partial x_i} + \frac{\partial}{\partial x_j}\left[\mu\left(\frac{\partial \bar{u}_i}{\partial x_j} + \frac{\partial \bar{u}_j}{\partial x_i}\right) - \rho\overline{u_i' u_j'}\right], \tag{3.6}$$

where $\overline{u_i' u_j'}$ are the components of the Reynolds stress tensor.

Equations (3.6) are the RANS equations, which with Eq. (3.3) constitute the model of the mean behavior of an isothermal turbulent flow. Nevertheless, besides the average velocities and the average pressure, there are six other unknowns associated with the Reynolds stress tensor. Thus, there is a need for additional models to solve the turbulent closure problem.

3.1.2 Turbulence closure model

Boussinesq proposed by analogy with Stokes model for viscous molecular stresses that (SILVEIRA NETO, 2020):

$$-\rho\overline{u_i'u_j'} = \mu_t\left(\frac{\partial\bar{u}_i}{\partial x_j} + \frac{\partial\bar{u}_j}{\partial x_i}\right) - \frac{2}{3}\rho k\,\delta_{ij}, \tag{3.7}$$

where μ_t is the turbulent dynamic viscosity of the flow, δ_{ij} is the Kronecker delta, and k is the turbulent kinetic energy defined by:

$$k \equiv \frac{1}{2}\overline{u_i'u_i'} = \frac{1}{2}\left(\overline{u'u'} + \overline{v'v'} + \overline{w'w'}\right). \tag{3.8}$$

Substituting Eq. (3.7) in Eqs. (3.6), the following equations are obtained:

$$\frac{\partial(\rho\bar{u}_i\bar{u}_j)}{\partial x_j} = -\frac{\partial\bar{p}}{\partial x_i} + \frac{\partial}{\partial x_j}\left[\mu\left(\frac{\partial\bar{u}_i}{\partial x_j} + \frac{\partial\bar{u}_j}{\partial x_i}\right) + \mu_t\left(\frac{\partial\bar{u}_i}{\partial x_j} + \frac{\partial\bar{u}_j}{\partial x_i}\right) - \frac{2}{3}\rho k\,\delta_{ij}\right]. \tag{3.9}$$

The divergent term involving the turbulent kinetic energy $(2/3)\rho k\delta_{ij}$ results in its gradient:

$$\frac{\partial}{\partial x_j}\left(\frac{2}{3}\rho k\,\delta_{ij}\right) = \frac{2}{3}\frac{\partial(\rho k)}{\partial x_i}, \tag{3.10}$$

which allows to incorporate it into the pressure gradient term of Eq. (3.9) generating a modified pressure $\bar{p^*}$:

$$\bar{p^*} = \bar{p} + \frac{2}{3}\rho k. \tag{3.11}$$

Finally, the modeled equations are given by:

$$\frac{\partial(\rho\bar{u}_i\bar{u}_j)}{\partial x_j} = -\frac{\partial\bar{p^*}}{\partial x_i} + \frac{\partial}{\partial x_j}\left[(\mu+\mu_t)\left(\frac{\partial\bar{u}_i}{\partial x_j} + \frac{\partial\bar{u}_j}{\partial x_i}\right)\right]. \tag{3.12}$$

Equations (3.12) are not yet closed due to the unknown turbulent viscosity. Calculating this flow property is the main problem in the closure modeling of the RANS equations. There are several turbulence closure models that rely on the concept of turbulent viscosity. In general, they are classified into models with zero, one, and two transport equations. However, there are also models for alternative closure, such as the algebraic models and the Reynolds stress model (SILVEIRA NETO, 2020).

For the present thesis simulations, the k-ε turbulence closure model is considered. This model, originally proposed by Chou (1945), requires solving two extra transport equations: one for the turbulent kinetic energy k and another for the turbulent kinetic energy dissipation ε. Subsequent to Chou (1945), advancements were made to the k-ε model, as seen in Harlow and Nakayama (1968). Nonetheless, the most established version of this model in literature was introduced by Jones and Launder (1972), which is commonly referred to as the standard k-ε model.

In the standard k-ε model, the turbulent viscosity is calculated by:

$$\mu_t = \rho \frac{C_\mu k^2}{\varepsilon}, \tag{3.13}$$

which depends on the following transport equations:

$$\frac{\partial(\rho \bar{u}_j k)}{\partial x_j} = \frac{\partial}{\partial x_j}\left[\left(\mu + \frac{\mu_t}{\sigma_k}\right)\frac{\partial k}{\partial x_j}\right] + \mu_t S^2 - \rho\varepsilon, \tag{3.14}$$

$$\frac{\partial(\rho \bar{u}_j \varepsilon)}{\partial x_j} = \frac{\partial}{\partial x_j}\left[\left(\mu + \frac{\mu_t}{\sigma_\varepsilon}\right)\frac{\partial \varepsilon}{\partial x_j}\right] + C_{\varepsilon 1}\frac{\varepsilon}{k}\mu_t S^2 - \rho C_{\varepsilon 2}\frac{\varepsilon^2}{k}, \tag{3.15}$$

where $S = \sqrt{2S_{ij}S_{ij}}$, and S_{ij} is the rate of strain tensor defined as:

$$S_{ij} = \frac{1}{2}\left(\frac{\partial \bar{u}_i}{\partial x_j} + \frac{\partial \bar{u}_j}{\partial x_i}\right). \tag{3.16}$$

Over time, there have been proposals for modifications to the standard k-ε model. However, as these proposals generally did not suggest significant changes in the deduction processes of the transport equations, they retained the same nomenclature. Its variants are normally characterized by different values of constants. Here, the constants of Eqs. (3.13) to (3.15) are used according to Launder and Sharma (1974): $\sigma_k = 1.0$, $\sigma_\varepsilon = 1.3$, $C_{\varepsilon_1} = 1.44$, $C_{\varepsilon_2} = 1.92$, and $C_\mu = 0.09$.

The standard k-ε model is quite popular for simulating industrial problems due to its low computational cost and relatively simple implementation. Furthermore, it offers reasonable predictions for several turbulent flows, particularly developed and free shear flows. However, this model alone is not well-suited for flows near walls and therefore requires specific modeling to treat wall regions.

3.1.2.1 Wall treatment

The two-layer model (CHEN; PATEL, 1988) is employed to handle both the core flow and the near-wall region. Essentially, it combines the standard k-ε model for solving the turbulent flow region and one transport equation model for solving the region affected by the viscosity. In this last model, k is computed from Eq. (3.14), while ε is determined by:

$$\varepsilon = \frac{k^{3/2}}{l_\varepsilon}, \tag{3.17}$$

where the characteristic length l_ε is given by:

$$l_\varepsilon = y C_l \left[1 - \exp\left(-Re_y / A_\varepsilon\right)\right], \tag{3.18}$$

and Re_y is the turbulent Reynolds number:

$$Re_y = \frac{\rho y \sqrt{k}}{\mu}, \tag{3.19}$$

which depends on the distance from the wall to the cell centers y. This Reynolds number is the demarcation of the two regions: fully turbulent if $Re_y > Re_y^*$, and viscosity-affected if $Re_y < Re_y^*$, with $Re_y^* = 200$.

Still considering the one transport equation model, the turbulent viscosity is calculated from:

$$\mu_{t,\mathrm{2layer}} = \rho C_\mu l_\mu \sqrt{k}, \tag{3.20}$$

where the characteristic length l_μ is estimated by:

$$l_\mu = y C_l \left[1 - \exp\left(-Re_y / A_\mu\right)\right]. \tag{3.21}$$

In both characteristic length formulas, Eqs. (3.18) and (3.21), the constants are taken as: $C_l = 0.4187 C_\mu^{-3/4}$, $A_\mu = 70$, and $A_\varepsilon = 2C_l$.

The combination of the standard and the one-equation models is accomplished by summing the turbulent viscosities:

$$\mu_t = \lambda_\varepsilon \, \mu_{t,\text{standard}} + (1 - \lambda_\varepsilon) \, \mu_{t,\text{2layer}}, \tag{3.22}$$

which is smoothed by a blending function λ_ε:

$$\lambda_\varepsilon = \frac{1}{2}\left[1 + \tanh\left(\frac{Re_y - Re_y^*}{A}\right)\right], \tag{3.23}$$

where A determines the width of the blending function:

$$A = \frac{0.2\, Re_y^*}{\operatorname{arctanh}(0.98)}. \tag{3.24}$$

The purpose of λ_ε is to prevent the divergence of results when the solutions of both models do not match. Thus, the blending function is defined in such a way that it tends to zero as approaching the wall and tends to unity as moving away from the wall.

The refinement of the computational mesh near the wall is fundamental to guaranteeing accurate predictions for the fluid flow using the two-layer k-ε model. Since no wall functions are used, the centroid of the cells adjacent to the wall must lie within the viscous sublayer. In other words, the dimensionless distance from the centroid to the wall must be $y^+ \approx 1$:

$$y^+ = \frac{\rho\, y\, u_\tau}{\mu} \qquad \text{with} \qquad u_\tau = \sqrt{\frac{\tau_w}{\rho}}, \tag{3.25}$$

where the velocity u_τ is obtained as a function of the shear stress on the wall τ_w.

3.1.3 Continuous adjoint for fluid flows

The shape optimization problem restricted by a fluid flow can be stated as in Eq. (2.8):

$$\begin{aligned} &\text{minimize} \quad J(\beta, \bar{u}_i, \bar{p}) \\ &\text{subject to} \quad \mathcal{R}(\beta, \bar{u}_i, \bar{p}) = 0, \end{aligned} \tag{3.26}$$

where the state variables are the flow field information $\phi = (\bar{u}_i, \bar{p})$ and the state equations $\mathcal{R} = (R_i, Q)^\intercal$ are the Navier-Stokes and continuity equations for incompressible, isothermal, steady-state fluid flows, Eqs. (3.12) and (3.3). For the mathematical development of the adjoint method, these primal equations were adopted in the non-divergence form, as shown below:

$$R_i = \rho \bar{u}_j \frac{\partial \bar{u}_i}{\partial x_j} + \frac{\partial \bar{p}}{\partial x_i} - \frac{\partial}{\partial x_j}\left[\mu_{\text{eff}}\left(\frac{\partial \bar{u}_i}{\partial x_j} + \frac{\partial \bar{u}_j}{\partial x_i}\right)\right] = 0, \tag{3.27}$$

$$Q = -\frac{\partial \bar{u}_i}{\partial x_i} = 0, \tag{3.28}$$

with $\mu_{\text{eff}} = (\mu + \mu_t)$ representing the effective viscosity of the flow.

As covered in Section 2.3.2, the adjoint equations can be derived from the variation of the Lagrange function L:

$$L = J + \int_\Omega (\hat{u}_i, \hat{p})\, \mathcal{R}\, \mathrm{d}\Omega = J + \int_\Omega (\hat{u}_i R_i + \hat{p} Q)\ \mathrm{d}\Omega, \tag{3.29}$$

which leads to Eq. (2.15):

$$\begin{aligned}\delta L = & \int_{\Gamma_\mathrm{O} \cap \Gamma_\mathrm{D}} \delta_\beta J_\Gamma\, \mathrm{d}\Gamma + \int_{\Gamma_\mathrm{O}} (\delta_{\bar{u}_i} J_\Gamma + \delta_{\bar{p}} J_\Gamma)\ \mathrm{d}\Gamma + \int_{\Omega_\mathrm{O}} (\delta_{\bar{u}_i} J_\Omega + \delta_{\bar{p}} J_\Omega)\ \mathrm{d}\Omega \\ & + \int_\Omega (\hat{u}_i \delta R_i + \hat{p} \delta Q)\ \mathrm{d}\Omega,\end{aligned} \tag{3.30}$$

where the adjoint variables $\hat{\phi} = (\hat{u}_i, \hat{p})$ are the adjoint velocity and the adjoint pressure.

The variations of the primal equations $(\delta R_i, \delta Q)$ with respect to $(\bar{u}_i, \bar{p})$ can be obtained straightforwardly as:

$$\delta R_i = \rho(\delta \bar{u}_j)\frac{\partial \bar{u}_i}{\partial x_j} + \rho \bar{u}_j \frac{\partial(\delta \bar{u}_i)}{\partial x_j} + \frac{\partial(\delta \bar{p})}{\partial x_i} - \frac{\partial}{\partial x_j}\left[\mu_{\text{eff}}\left(\frac{\partial(\delta \bar{u}_i)}{\partial x_j} + \frac{\partial(\delta \bar{u}_j)}{\partial x_i}\right)\right], \tag{3.31}$$

$$\delta Q = -\frac{\partial(\delta \bar{u}_i)}{\partial x_i}. \tag{3.32}$$

Here, the variation of the effective viscosity μ_{eff} was neglected. For turbulent flows, neglecting this variation constitutes the common approximation known as “frozen turbulence”. Thereby, Eq. (3.30) can be rewritten as:

$$
\begin{aligned}
\delta L = & \int_{\Gamma_\mathrm{O}\cap\Gamma_\mathrm{D}} \delta_\beta J_\Gamma \,\mathrm{d}\Gamma + \int_{\Gamma_\mathrm{O}} \left(\delta_{\bar{u}_i} J_\Gamma + \delta_{\bar{p}} J_\Gamma\right) \mathrm{d}\Gamma + \int_{\Omega_\mathrm{O}} \left(\delta_{\bar{u}_i} J_\Omega + \delta_{\bar{p}} J_\Omega\right) \mathrm{d}\Omega \\
& + \int_\Omega \hat{u}_i \rho (\delta \bar{u}_j) \frac{\partial \bar{u}_i}{\partial x_j} \,\mathrm{d}\Omega + \underbrace{\int_\Omega \hat{u}_i \rho \bar{u}_j \frac{\partial (\delta \bar{u}_i)}{\partial x_j} \,\mathrm{d}\Omega}_{\text{(t.1)}} + \underbrace{\int_\Omega \hat{u}_i \frac{\partial (\delta \bar{p})}{\partial x_i} \,\mathrm{d}\Omega}_{\text{(t.2)}} \\
& \underbrace{- \int_\Omega \hat{u}_i \frac{\partial}{\partial x_j} \left[\mu_\mathrm{eff} \left(\frac{\partial (\delta \bar{u}_i)}{\partial x_j} + \frac{\partial (\delta \bar{u}_j)}{\partial x_i}\right)\right] \mathrm{d}\Omega}_{\text{(t.3)}} \underbrace{- \int_\Omega \hat{p} \frac{\partial (\delta \bar{u}_i)}{\partial x_i} \,\mathrm{d}\Omega}_{\text{(t.4)}} .
\end{aligned}
\tag{3.33}
$$

Before proceeding with the deductions, it is important to introduce the local coordinate system of the domain boundary Γ, in which the flow velocity can be decomposed as:

$$
\bar{u}_i = \bar{u}_n n_i + \bar{u}_t t_i + \bar{u}_s s_i, \tag{3.34}
$$

and the differential operator as:

$$
\frac{\partial}{\partial x_i} = \frac{\partial}{\partial n} n_i + \frac{\partial}{\partial t} t_i + \frac{\partial}{\partial s} s_i. \tag{3.35}
$$

Thus, the vector n_i consists of the unit vector normal to the boundary, which points outside the fluid domain Ω, while t_i and s_i are the unit vectors that lie in the plane of the boundary.

The next step is to apply integration by parts, using Gauss’s theorem, in the terms (t.1) to (t.4) of Eq. (3.33). In the term (t.3), the integration by parts has to be applied twice. Hence, it follows that:

$$
\text{(t.1)}: \int_\Omega \hat{u}_i \rho \bar{u}_j \frac{\partial (\delta \bar{u}_i)}{\partial x_j} \,\mathrm{d}\Omega = \int_\Gamma \rho \bar{u}_j n_j \hat{u}_i \delta \bar{u}_i \,\mathrm{d}\Gamma - \int_\Omega \delta \bar{u}_i \frac{\partial (\rho \bar{u}_j \hat{u}_i)}{\partial x_j} \,\mathrm{d}\Omega \tag{3.36}
$$

$$
\text{(t.2)}: \int_\Omega \hat{u}_i \frac{\partial (\delta \bar{p})}{\partial x_i} \,\mathrm{d}\Omega = \int_\Gamma \delta \bar{p} \left(\hat{u}_i n_i\right) \mathrm{d}\Gamma - \int_\Omega \delta \bar{p} \left(\frac{\partial \hat{u}_i}{\partial x_i}\right) \mathrm{d}\Omega \tag{3.37}
$$

$$\begin{aligned}(\text{t.3}):\ &-\int_\Omega \hat{u}_i\frac{\partial}{\partial x_j}\left[\mu_{\text{eff}}\left(\frac{\partial(\delta\bar{u}_i)}{\partial x_j}+\frac{\partial(\delta\bar{u}_j)}{\partial x_i}\right)\right]\,\mathrm{d}\Omega\\ &=\underbrace{-\int_\Omega \hat{u}_i\frac{\partial}{\partial x_j}\left[\mu_{\text{eff}}\frac{\partial(\delta\bar{u}_i)}{\partial x_j}\right]\,\mathrm{d}\Omega}_{(\text{t.5})}\underbrace{-\int_\Omega \hat{u}_i\frac{\partial}{\partial x_j}\left[\mu_{\text{eff}}\frac{\partial(\delta\bar{u}_j)}{\partial x_i}\right]\,\mathrm{d}\Omega}_{(\text{t.6})}\end{aligned}\tag{3.38a}$$

$$\begin{aligned}(\text{t.5}):\ &-\int_\Omega \hat{u}_i\frac{\partial}{\partial x_j}\left[\mu_{\text{eff}}\frac{\partial(\delta\bar{u}_i)}{\partial x_j}\right]\,\mathrm{d}\Omega\\ &=-\int_\Gamma \hat{u}_i\left[\mu_{\text{eff}}\frac{\partial(\delta\bar{u}_i)}{\partial x_j}\right]n_j\,\mathrm{d}\Gamma+\int_\Omega\left[\mu_{\text{eff}}\frac{\partial(\delta\bar{u}_i)}{\partial x_j}\right]\frac{\partial\hat{u}_i}{\partial x_j}\,\mathrm{d}\Omega\\ &=-\int_\Gamma \hat{u}_i\left[\mu_{\text{eff}}\frac{\partial(\delta\bar{u}_i)}{\partial x_j}\right]n_j\,\mathrm{d}\Gamma+\int_\Gamma\delta\bar{u}_i\left[\mu_{\text{eff}}\frac{\partial\hat{u}_i}{\partial x_j}\right]n_j\,\mathrm{d}\Gamma-\int_\Omega\delta\bar{u}_i\frac{\partial}{\partial x_j}\left[\mu_{\text{eff}}\frac{\partial\hat{u}_i}{\partial x_j}\right]\,\mathrm{d}\Omega\end{aligned}\tag{3.38b}$$

$$\begin{aligned}(\text{t.6}):\ &-\int_\Omega \hat{u}_i\frac{\partial}{\partial x_j}\left[\mu_{\text{eff}}\frac{\partial(\delta\bar{u}_j)}{\partial x_i}\right]\,\mathrm{d}\Omega\\ &=-\int_\Gamma \hat{u}_i\left[\mu_{\text{eff}}\frac{\partial(\delta\bar{u}_j)}{\partial x_i}\right]n_j\,\mathrm{d}\Gamma+\int_\Omega\left[\mu_{\text{eff}}\frac{\partial(\delta\bar{u}_j)}{\partial x_i}\right]\frac{\partial\hat{u}_i}{\partial x_j}\,\mathrm{d}\Omega\\ &=-\int_\Gamma \hat{u}_i\left[\mu_{\text{eff}}\frac{\partial(\delta\bar{u}_j)}{\partial x_i}\right]n_j\,\mathrm{d}\Gamma+\int_\Gamma\delta\bar{u}_j\left[\mu_{\text{eff}}\frac{\partial\hat{u}_i}{\partial x_j}\right]n_i\,\mathrm{d}\Gamma-\int_\Omega\delta\bar{u}_j\frac{\partial}{\partial x_i}\left[\mu_{\text{eff}}\frac{\partial\hat{u}_i}{\partial x_j}\right]\,\mathrm{d}\Omega\\ &=-\int_\Gamma \hat{u}_i\left[\mu_{\text{eff}}\frac{\partial(\delta\bar{u}_j)}{\partial x_i}\right]n_j\,\mathrm{d}\Gamma+\int_\Gamma\delta\bar{u}_i\left[\mu_{\text{eff}}\frac{\partial\hat{u}_j}{\partial x_i}\right]n_j\,\mathrm{d}\Gamma-\int_\Omega\delta\bar{u}_i\frac{\partial}{\partial x_j}\left[\mu_{\text{eff}}\frac{\partial\hat{u}_j}{\partial x_i}\right]\,\mathrm{d}\Omega\end{aligned}\tag{3.38c}$$

$$\begin{aligned}\therefore(\text{t.3}):\ &-\int_\Omega \hat{u}_i\frac{\partial}{\partial x_j}\left[\mu_{\text{eff}}\left(\frac{\partial(\delta\bar{u}_i)}{\partial x_j}+\frac{\partial(\delta\bar{u}_j)}{\partial x_i}\right)\right]\,\mathrm{d}\Omega\\ &=-\int_\Gamma \hat{u}_i\left[\mu_{\text{eff}}\frac{\partial(\delta\bar{u}_i)}{\partial x_j}\right]n_j\,\mathrm{d}\Gamma+\int_\Gamma\delta\bar{u}_i\left[\mu_{\text{eff}}\frac{\partial\hat{u}_i}{\partial x_j}\right]n_j\,\mathrm{d}\Gamma-\int_\Omega\delta\bar{u}_i\frac{\partial}{\partial x_j}\left[\mu_{\text{eff}}\frac{\partial\hat{u}_i}{\partial x_j}\right]\,\mathrm{d}\Omega\\ &\quad-\int_\Gamma \hat{u}_i\left[\mu_{\text{eff}}\frac{\partial(\delta\bar{u}_j)}{\partial x_i}\right]n_j\,\mathrm{d}\Gamma+\int_\Gamma\delta\bar{u}_i\left[\mu_{\text{eff}}\frac{\partial\hat{u}_j}{\partial x_i}\right]n_j\,\mathrm{d}\Gamma-\int_\Omega\delta\bar{u}_i\frac{\partial}{\partial x_i}\left[\mu_{\text{eff}}\frac{\partial\hat{u}_j}{\partial x_j}\right]\,\mathrm{d}\Omega\\ &=-\int_\Gamma \hat{u}_i\left[\mu_{\text{eff}}\left(\frac{\partial(\delta\bar{u}_i)}{\partial x_j}+\frac{\partial(\delta\bar{u}_j)}{\partial x_i}\right)\right]n_j\,\mathrm{d}\Gamma+\int_\Gamma\delta\bar{u}_i\left[\mu_{\text{eff}}\left(\frac{\partial\hat{u}_i}{\partial x_j}+\frac{\partial\hat{u}_j}{\partial x_i}\right)\right]n_j\,\mathrm{d}\Gamma\\ &\quad-\int_\Omega\delta\bar{u}_i\frac{\partial}{\partial x_j}\left[\mu_{\text{eff}}\left(\frac{\partial\hat{u}_i}{\partial x_j}+\frac{\partial\hat{u}_j}{\partial x_i}\right)\right]\,\mathrm{d}\Omega\end{aligned}\tag{3.38d}$$

$$(\text{t.4}):\ -\int_\Omega\hat{p}\,\frac{\partial(\delta\bar{u}_i)}{\partial x_i}\,\mathrm{d}\Omega=-\int_\Gamma\hat{p}\,(\delta\bar{u}_i n_i)\ \mathrm{d}\Gamma+\int_\Omega\delta\bar{u}_i\frac{\partial\hat{p}}{\partial x_i}\,\mathrm{d}\Omega\tag{3.39}$$

Then, replacing Eqs. (3.36) to (3.39) in Eq. (3.33), it can be found that:

$$
\begin{aligned}
\delta L = & \int_{\Gamma_\mathrm{O}\cap\Gamma_\mathrm{D}} \delta_\beta J_\Gamma \,\mathrm{d}\Gamma + \int_{\Gamma_\mathrm{O}} \left(\delta_{\bar{u}_i} J_\Gamma + \delta_{\bar{p}} J_\Gamma\right) \mathrm{d}\Gamma + \int_{\Omega_\mathrm{O}} \left(\delta_{\bar{u}_i} J_\Omega + \delta_{\bar{p}} J_\Omega\right) \mathrm{d}\Omega \\
& + \int_\Omega \hat{u}_i \rho (\delta \bar{u}_j) \frac{\partial \bar{u}_i}{\partial x_j} \,\mathrm{d}\Omega + \int_\Gamma \rho \bar{u}_j n_j \hat{u}_i \left(\delta \bar{u}_i\right) \mathrm{d}\Gamma - \int_\Omega \frac{\partial(\rho \bar{u}_j \hat{u}_i)}{\partial x_j} \left(\delta \bar{u}_i\right) \mathrm{d}\Omega \\
& + \int_\Gamma \delta \bar{p} \left(\hat{u}_i n_i\right) \mathrm{d}\Gamma - \int_\Omega \delta \bar{p} \left(\frac{\partial \hat{u}_i}{\partial x_i}\right) \mathrm{d}\Omega - \int_\Gamma \hat{p} \left(\delta \bar{u}_i n_i\right) \mathrm{d}\Gamma + \int_\Omega \delta \bar{u}_i \frac{\partial \hat{p}}{\partial x_i} \,\mathrm{d}\Omega \\
& + \int_\Gamma \delta \bar{u}_i \left[\mu_\mathrm{eff} \left(\frac{\partial \hat{u}_i}{\partial x_j} + \frac{\partial \hat{u}_j}{\partial x_i}\right)\right] n_j \,\mathrm{d}\Gamma - \int_\Gamma \hat{u}_i \left[\mu_\mathrm{eff} \left(\frac{\partial(\delta \bar{u}_i)}{\partial x_j} + \frac{\partial(\delta \bar{u}_j)}{\partial x_i}\right)\right] n_j \,\mathrm{d}\Gamma \\
& - \int_\Omega \delta \bar{u}_i \frac{\partial}{\partial x_j} \left[\mu_\mathrm{eff} \left(\frac{\partial \hat{u}_i}{\partial x_j} + \frac{\partial \hat{u}_j}{\partial x_i}\right)\right] \mathrm{d}\Omega.
\end{aligned}
\tag{3.40}
$$

The variation of the objective function in relation to the state variables can be expressed by:

$$
\delta_{\bar{u}_i} J = \delta \bar{u}_i \frac{\partial J}{\partial \bar{u}_i}, \tag{3.41}
$$

and

$$
\delta_{\bar{p}} J = \delta \bar{p} \frac{\partial J}{\partial \bar{p}}. \tag{3.42}
$$

Equations (3.41) and (3.42) are only valid for algebraic terms and require a reformulation if the objective function contains differential expressions (STÜCK, 2011).

Equation (3.40) can be rearranged as:

$$
\begin{aligned}
\delta L = & \int_{\Gamma_\mathrm{O}\cap\Gamma_\mathrm{D}} \delta_\beta J_\Gamma \,\mathrm{d}\Gamma - \int_\Gamma \hat{u}_i \left[\mu_\mathrm{eff} \left(\frac{\partial(\delta \bar{u}_i)}{\partial n} + \frac{\partial(\delta \bar{u}_n)}{\partial x_i}\right)\right] \mathrm{d}\Gamma \\
& + \int_\Gamma \delta \bar{u}_i \left[\rho \bar{u}_n \hat{u}_i + \mu_\mathrm{eff} \left(\frac{\partial \hat{u}_i}{\partial n} + \frac{\partial \hat{u}_n}{\partial x_i}\right) - \hat{p} n_i\right] \mathrm{d}\Gamma + \int_{\Gamma_\mathrm{O}} \delta \bar{u}_i \left(\frac{\partial J_\Gamma}{\partial \bar{u}_i}\right) \mathrm{d}\Gamma \\
& + \int_\Gamma \delta \bar{p} \left(\hat{u}_n\right) \mathrm{d}\Gamma + \int_{\Gamma_\mathrm{O}} \delta \bar{p} \left(\frac{\partial J_\Gamma}{\partial \bar{p}}\right) \mathrm{d}\Gamma \\
& + \int_\Omega \delta \bar{u}_i \left\{-\frac{\partial(\rho \bar{u}_j \hat{u}_i)}{\partial x_j} + \frac{\partial \hat{p}}{\partial x_i} - \frac{\partial}{\partial x_j} \left[\mu_\mathrm{eff} \left(\frac{\partial \hat{u}_i}{\partial x_j} + \frac{\partial \hat{u}_j}{\partial x_i}\right)\right] + \rho \hat{u}_j \frac{\partial \bar{u}_j}{\partial x_i}\right\} \mathrm{d}\Omega \\
& + \int_{\Omega_\mathrm{O}} \delta \bar{u}_i \left(\frac{\partial J_\Omega}{\partial \bar{u}_i}\right) \mathrm{d}\Omega - \int_\Omega \delta \bar{p} \left(\frac{\partial \hat{u}_i}{\partial x_i}\right) \mathrm{d}\Omega + \int_{\Omega_\mathrm{O}} \delta \bar{p} \left(\frac{\partial J_\Omega}{\partial \bar{p}}\right) \mathrm{d}\Omega.
\end{aligned}
\tag{3.43}
$$

Equation (3.43) has to be fulfilled for any $(\delta \bar{u}_i, \delta \bar{p})$ that satisfy the primal fluid dynamics equations, which can in general be accomplished if the integrals vanish individually. For the integrals over the domain, this requirement gives rise to the adjoint equations (OTHMER, 2008). Accordingly, the adjoint equations for steady-state, incompressible fluid flows with frozen turbulence are derived as follows:

$$\begin{cases} \dfrac{\partial \hat{u}_i}{\partial x_i} = \dfrac{\partial J_\Omega}{\partial \bar{p}} & \text{in} \quad \Omega_O, \\[2ex] \dfrac{\partial \hat{u}_i}{\partial x_i} = 0 & \text{in} \quad \Omega \setminus \Omega_O, \end{cases} \tag{3.44}$$

$$\begin{cases} -\dfrac{\partial \left(\rho \bar{u}_j \hat{u}_i\right)}{\partial x_j} = -\dfrac{\partial \hat{p}}{\partial x_i} + \dfrac{\partial}{\partial x_j}\left[\mu_{\text{eff}}\left(\dfrac{\partial \hat{u}_i}{\partial x_j} + \dfrac{\partial \hat{u}_j}{\partial x_i}\right)\right] - \rho \hat{u}_j \dfrac{\partial \bar{u}_j}{\partial x_i} - \dfrac{\partial J_\Omega}{\partial \bar{u}_i} & \text{in} \quad \Omega_O, \\[2ex] -\dfrac{\partial \left(\rho \bar{u}_j \hat{u}_i\right)}{\partial x_j} = -\dfrac{\partial \hat{p}}{\partial x_i} + \dfrac{\partial}{\partial x_j}\left[\mu_{\text{eff}}\left(\dfrac{\partial \hat{u}_i}{\partial x_j} + \dfrac{\partial \hat{u}_j}{\partial x_i}\right)\right] - \rho \hat{u}_j \dfrac{\partial \bar{u}_j}{\partial x_i} & \text{in} \quad \Omega \setminus \Omega_O. \end{cases} \tag{3.45}$$

Although the signs of the advective term are different, the structure of the adjoint equations is very similar to that of the primal equations, Eqs. (3.27) and (3.28). This difference means that the information from the adjoint field is transported in the opposite direction to that of the primal field.

The variation of the Lagrange function is reformulated as:

$$\begin{aligned} \delta L = & \int_{\Gamma_\mathrm{O} \cap \Gamma_\mathrm{D}} \delta_\beta J_\Gamma \, \mathrm{d}\Gamma - \int_\Gamma \hat{u}_i \left[\mu_{\text{eff}}\left(\frac{\partial(\delta \bar{u}_i)}{\partial n} + \frac{\partial(\delta \bar{u}_n)}{\partial x_i}\right)\right] \mathrm{d}\Gamma \\ & + \int_\Gamma \left\{\delta \bar{u}_i \left[\rho \bar{u}_n \hat{u}_i + \mu_{\text{eff}}\left(\frac{\partial \hat{u}_i}{\partial n} + \frac{\partial \hat{u}_n}{\partial x_i}\right) - \hat{p} n_i\right]\right\} \mathrm{d}\Gamma + \int_{\Gamma_\mathrm{O}} \delta \bar{u}_i \left(\frac{\partial J_\Gamma}{\partial \bar{u}_i}\right) \mathrm{d}\Gamma \\ & + \int_\Gamma \delta \bar{p} \left(\hat{u}_n\right) \mathrm{d}\Gamma + \int_{\Gamma_\mathrm{O}} \delta \bar{p} \left(\frac{\partial J_\Gamma}{\partial \bar{p}}\right) \mathrm{d}\Gamma. \end{aligned} \tag{3.46}$$

3.1.3.1 Boundary conditions

Only three types of boundaries are involved in the problems addressed in this thesis: **inlet**, **wall** and **outlet** ($\Gamma = \Gamma_{\text{in}} \cup \Gamma_{\text{wall}} \cup \Gamma_{\text{out}}$). To derive the boundary conditions for the adjoint variables, the surface integrals of Eq. (3.46) are analyzed under consideration of the primal boundary conditions. Boundaries that coincide with parts of the design surface require special attention. For now, the focus is only on boundaries that do not coincide with the design surface $(\Gamma \setminus \Gamma_{\mathrm{D}})$.

The boundary conditions for the adjoint pressure and the adjoint velocity can be obtained from:

$$\int_{\Gamma} \delta\bar{p}\,(\hat{u}_n)\ \mathrm{d}\Gamma + \int_{\Gamma_{\mathrm{O}}} \delta\bar{p}\left(\frac{\partial J_{\Gamma}}{\partial \bar{p}}\right)\ \mathrm{d}\Gamma = 0, \tag{3.47}$$

$$\begin{aligned}&\int_{\Gamma} \delta\bar{u}_i \left\{\rho\,\bar{u}_n\,\hat{u}_i + \left[\mu_{\mathrm{eff}}\left(\frac{\partial \hat{u}_i}{\partial n} + \frac{\partial \hat{u}_n}{\partial x_i}\right)\right] - \hat{p}\,n_i\right\}\ \mathrm{d}\Gamma + \int_{\Gamma_{\mathrm{O}}} \delta\bar{u}_i\left(\frac{\partial J_{\Gamma}}{\partial \bar{u}_i}\right)\ \mathrm{d}\Gamma \\ &- \int_{\Gamma} \hat{u}_i\left[\mu_{\mathrm{eff}}\left(\frac{\partial(\delta\bar{u}_i)}{\partial n} + \frac{\partial(\delta\bar{u}_n)}{\partial x_i}\right)\right]\ \mathrm{d}\Gamma = 0.\end{aligned} \tag{3.48}$$

At the fluid **inlet** boundaries Γ_{in} and no-slip **wall** boundaries Γ_{wall}, a Dirichlet condition for the velocity components and a Neumann condition for the pressure are considered:

$$\bar{u}_n = \begin{cases} U_{\mathrm{in}} & \text{on} \quad \Gamma_{\mathrm{in}}, \\ 0 & \text{on} \quad \Gamma_{\mathrm{wall}}, \end{cases} \tag{3.49}$$

$$\bar{u}_t = \bar{u}_s = 0 \quad \text{on} \quad \Gamma_{\mathrm{in}} \text{ and } \Gamma_{\mathrm{wall}}, \tag{3.50}$$

$$\frac{\partial \bar{p}}{\partial n} = 0 \quad \text{on} \quad \Gamma_{\mathrm{in}} \text{ and } \Gamma_{\mathrm{wall}}, \tag{3.51}$$

where U_{in} is the inlet velocity of the fluid in the domain. By definition, the local variation of velocity on these boundaries is zero, $\delta\bar{u}_i = 0$. Therefore, Eqs. (3.47) and (3.48) on the inlet results in:

$$\int_{\Gamma} \delta\bar{p}\,(\hat{u}_n)\ \mathrm{d}\Gamma = -\int_{\Gamma_{\mathrm{O}}} \delta\bar{p}\left(\frac{\partial J_{\Gamma}}{\partial \bar{p}}\right)\ \mathrm{d}\Gamma, \tag{3.52}$$

$$\hat{u}_i\left[\mu_{\mathrm{eff}}\left(\frac{\partial(\delta\bar{u}_i)}{\partial n} + \frac{\partial(\delta\bar{u}_n)}{\partial x_i}\right)\right] = 0. \tag{3.53}$$

For an arbitrary value of $\delta\bar{p}$, it is found from Eq. (3.52) that:

$$\hat{u}_n = \begin{cases} -\dfrac{\partial J_\Gamma}{\partial \bar{p}} & \text{on} \quad \Gamma_{\text{in}} \cap \Gamma_{\text{O}} \text{ and } \Gamma_{\text{wall}} \cap \Gamma_{\text{O}}, \\ \\ 0 & \text{on} \quad \Gamma_{\text{in}} \setminus \Gamma_{\text{O}} \text{ and } \Gamma_{\text{wall}} \setminus \Gamma_{\text{O}}. \end{cases} \tag{3.54}$$

Considering Eq. (3.3) for a negligible curvature, it is inferred that:

$$\frac{\partial \bar{u}_i}{\partial x_i} = \frac{\partial \bar{u}_n}{\partial n} + \frac{\partial \bar{u}_t}{\partial t} + \frac{\partial \bar{u}_s}{\partial s} = 0. \tag{3.55}$$

Given the constant velocity for the in-plane components on inlet and wall boundaries, it is implied that:

$$\frac{\partial \bar{u}_t}{\partial t} = \frac{\partial \bar{u}_s}{\partial s} = 0, \tag{3.56}$$

which implicates from Eq. (3.55) that:

$$\frac{\partial \bar{u}_n}{\partial n} = 0 \Rightarrow \frac{\partial (\delta \bar{u}_n)}{\partial n} = 0, \tag{3.57}$$

and, then:

$$\frac{\partial (\delta \bar{u}_i)}{\partial n} = \frac{\partial (\delta \bar{u}_t)}{\partial n} t_i + \frac{\partial (\delta \bar{u}_s)}{\partial n} s_i. \tag{3.58}$$

Substituting in Eq. (3.53):

$$\hat{u}_t \left[\mu_{\text{eff}} \left(\frac{\partial (\delta \bar{u}_t)}{\partial n} + \frac{\partial (\delta \bar{u}_n)}{\partial t} \right) \right] + \hat{u}_s \left[\mu_{\text{eff}} \left(\frac{\partial (\delta \bar{u}_s)}{\partial n} + \frac{\partial (\delta \bar{u}_n)}{\partial s} \right) \right] = 0, \tag{3.59}$$

it can be defined that:

$$\hat{u}_t = \hat{u}_s = 0 \quad \text{on} \quad \Gamma_{\text{in}} \text{ and } \Gamma_{\text{wall}}. \tag{3.60}$$

As for the primal pressure field, a Neumann condition for the adjoint pressure is considered:

$$\frac{\partial \hat{p}}{\partial n} = 0 \quad \text{on} \quad \Gamma_{\text{in}} \text{ and } \Gamma_{\text{wall}}. \tag{3.61}$$

In the case of **outlet** boundaries Γ_{out} with imposed pressure, a Dirichlet condition is applied for pressure, while a Neumann condition is applied for velocity:

$$\bar{p} = 0 \quad \text{on} \quad \Gamma_{\text{out}}, \tag{3.62}$$

$$\frac{\partial \bar{u}_i}{\partial n} = 0 \quad \text{on} \quad \Gamma_{\text{out}}. \tag{3.63}$$

By definition, both conditions remain unchanged, which means $\delta\bar{p} = 0$ and $\partial(\delta\bar{u}_i)/\partial n = 0$. In this way, the adjoint boundary conditions on the outlet can be obtained by:

$$\delta\bar{u}_i \left\{ \rho\bar{u}_n\hat{u}_i + \left[\mu_{\text{eff}} \left(\frac{\partial \hat{u}_i}{\partial n} + \frac{\partial \hat{u}_n}{\partial x_i} \right) \right] - \hat{p}n_i + \frac{\partial J_\Gamma}{\partial \bar{u}_i} \right\} - \hat{u}_i \left(\mu_{\text{eff}} \frac{\partial(\delta\bar{u}_n)}{\partial x_i} \right) = 0, \tag{3.64a}$$

$$\Rightarrow \delta\bar{u}_i \left\{ \rho\bar{u}_n\hat{u}_i + \mu_{\text{eff}} \left(\frac{\partial \hat{u}_i}{\partial n} \right) - \hat{p}n_i + \frac{\partial J_\Gamma}{\partial \bar{u}_i} \right\} = \mu_{\text{eff}} \left(\hat{u}_i \frac{\partial(\delta\bar{u}_n)}{\partial x_i} - \delta\bar{u}_i \frac{\partial \hat{u}_n}{\partial x_i} \right). \tag{3.64b}$$

According to Othmer (2008), the term on the right-hand side of Eq. (3.64) can be neglected, which leads to:

$$\delta\bar{u}_i \left\{ \rho\bar{u}_n\hat{u}_i + \mu_{\text{eff}} \left(\frac{\partial \hat{u}_i}{\partial n} \right) - \hat{p}n_i + \frac{\partial J_\Gamma}{\partial \bar{u}_i} \right\} = 0. \tag{3.65}$$

For an arbitrary value of $\delta\bar{u}_i$ on the outlet boundaries, it can imply that:

$$\hat{p}n_i = \rho\bar{u}_n\hat{u}_i + \mu_{\text{eff}} \left(\frac{\partial \hat{u}_i}{\partial n} \right) + \frac{\partial J_\Gamma}{\partial \bar{u}_i}. \tag{3.66}$$

Decomposing the above equation for the local coordinate system, the adjoint boundary conditions are obtained by:

$$\hat{p} = \begin{cases} \rho\bar{u}_n\hat{u}_n + \mu_{\text{eff}} \left(\dfrac{\partial \hat{u}_n}{\partial n} \right) + \dfrac{\partial J_\Gamma}{\partial \bar{u}_n} & \text{on} \quad \Gamma_{\text{out}} \cap \Gamma_{\text{O}}, \\ \rho\bar{u}_n\hat{u}_n + \mu_{\text{eff}} \left(\dfrac{\partial \hat{u}_n}{\partial n} \right) & \text{on} \quad \Gamma_{\text{out}} \setminus \Gamma_{\text{O}}, \end{cases} \tag{3.67}$$

$$\begin{cases} \rho\, \bar{u}_n\, \hat{u}_t + \mu_{\text{eff}} \left(\dfrac{\partial \hat{u}_t}{\partial n} \right) = -\dfrac{\partial J_\Gamma}{\partial \bar{u}_t} & \text{on} \quad \Gamma_{\text{out}} \cap \Gamma_{\text{O}}, \\[2ex] \rho\, \bar{u}_n\, \hat{u}_t + \mu_{\text{eff}} \left(\dfrac{\partial \hat{u}_t}{\partial n} \right) = 0 & \text{on} \quad \Gamma_{\text{out}} \setminus \Gamma_{\text{O}}, \end{cases} \tag{3.68}$$

$$\begin{cases} \rho\, \bar{u}_n\, \hat{u}_s + \mu_{\text{eff}} \left(\dfrac{\partial \hat{u}_s}{\partial n} \right) = -\dfrac{\partial J_\Gamma}{\partial \bar{u}_s} & \text{on} \quad \Gamma_{\text{out}} \cap \Gamma_{\text{O}}, \\[2ex] \rho\, \bar{u}_n\, \hat{u}_s + \mu_{\text{eff}} \left(\dfrac{\partial \hat{u}_s}{\partial n} \right) = 0 & \text{on} \quad \Gamma_{\text{out}} \setminus \Gamma_{\text{O}}. \end{cases} \tag{3.69}$$

3.1.3.2 Gradient equation

Finding the gradient of the optimization problem requires the remaining terms of Eq. (3.46) after resolving the adjoint boundary conditions, which are the boundary terms applied to the design surface:

$$\begin{aligned} \delta L = &\int_{\Gamma_{\text{O}} \cap \Gamma_{\text{D}}} \delta_\beta J_\Gamma \,\mathrm{d}\Gamma - \int_{\Gamma_{\text{D}}} \hat{u}_i \left[\mu_{\text{eff}} \left(\frac{\partial (\delta \bar{u}_i)}{\partial n} + \frac{\partial (\delta \bar{u}_n)}{\partial x_i} \right) \right] \mathrm{d}\Gamma \\ &+ \int_{\Gamma_{\text{D}}} \left\{ \delta \bar{u}_i \left[\rho\, \bar{u}_n\, \hat{u}_i + \mu_{\text{eff}} \left(\frac{\partial \hat{u}_i}{\partial n} + \frac{\partial \hat{u}_n}{\partial x_i} \right) - \hat{p}\, n_i \right] \right\} \mathrm{d}\Gamma + \int_{\Gamma_{\text{O}} \cap \Gamma_{\text{D}}} \delta \bar{u}_i \left(\frac{\partial J_\Gamma}{\partial \bar{u}_i} \right) \mathrm{d}\Gamma \\ &+ \int_{\Gamma_{\text{D}}} \delta \bar{p} \left(\hat{u}_n \right) \,\mathrm{d}\Gamma + \int_{\Gamma_{\text{O}} \cap \Gamma_{\text{D}}} \delta \bar{p} \left(\frac{\partial J_\Gamma}{\partial \bar{p}} \right) \mathrm{d}\Gamma. \end{aligned} \tag{3.70}$$

For the present thesis, two considerations must be highlighted. Firstly, the shape optimization has fixed inlet and outlet boundaries, which means they are not affected by the shape control. Hence, the only portion of Γ that is subject to shape variations is obviously the no-slip wall boundaries ($\Gamma_{\text{D}} \subset \Gamma_{\text{wall}}$). Secondly, the spacial perturbations on the design surface are represented by displacements in the normal direction of the surface:

$$\delta \beta = \delta n = n_i \delta x_i. \tag{3.71}$$

Thus, the convective variation $\delta_\beta J_\Gamma$ with respect to a surface normal perturbation δn reads:

$$\delta_\beta J_\Gamma = \delta n \frac{\partial J_\Gamma}{\partial n}. \tag{3.72}$$

In the primal system, $\bar{u}_i = 0$ on Γ_{wall}, so Eq. (3.70) yields:

$$\begin{aligned}\delta L = &\int_{\Gamma_{\text{O}} \cap \Gamma_{\text{D}}} \delta n \left(\frac{\partial J_\Gamma}{\partial n}\right) \, \mathrm{d}\Gamma + \int_{\Gamma_{\text{O}} \cap \Gamma_{\text{D}}} \delta \bar{u}_i \left(\frac{\partial J_\Gamma}{\partial \bar{u}_i}\right) \, \mathrm{d}\Gamma \\ &+ \int_{\Gamma_{\text{D}}} \delta \bar{u}_i \left[\mu_{\text{eff}} \left(\frac{\partial \hat{u}_i}{\partial n} + \frac{\partial \hat{u}_n}{\partial x_i}\right) - \hat{p} n_i\right] \mathrm{d}\Gamma \\ &+ \int_{\Gamma_{\text{D}}} \delta \bar{p} \, (\hat{u}_n) \, \mathrm{d}\Gamma + \int_{\Gamma_{\text{O}} \cap \Gamma_{\text{D}}} \delta \bar{p} \left(\frac{\partial J_\Gamma}{\partial \bar{p}}\right) \, \mathrm{d}\Gamma - \int_{\Gamma_{\text{D}}} \hat{u}_i \left[\mu_{\text{eff}} \left(\frac{\partial (\delta \bar{u}_i)}{\partial n} + \frac{\partial (\delta \bar{u}_n)}{\partial x_i}\right)\right] \mathrm{d}\Gamma. \end{aligned} \tag{3.73}$$

Evaluating the adjoint boundary conditions on Γ_{wall}, in the specific case of $\partial J_\Gamma / \partial \bar{p} = 0$, the boundary condition is $\hat{u}_i = 0$ for the adjoint velocity. This implies that:

$$\begin{aligned}\delta L = &\int_{\Gamma_{\text{O}} \cap \Gamma_{\text{D}}} \delta n \left(\frac{\partial J_\Gamma}{\partial n}\right) \, \mathrm{d}\Gamma + \int_{\Gamma_{\text{O}} \cap \Gamma_{\text{D}}} \delta \bar{u}_i \left(\frac{\partial J_\Gamma}{\partial \bar{u}_i}\right) \, \mathrm{d}\Gamma \\ &+ \int_{\Gamma_{\text{D}}} \delta \bar{u}_i \left[\mu_{\text{eff}} \left(\frac{\partial \hat{u}_i}{\partial n} + \frac{\partial \hat{u}_n}{\partial x_i}\right) - \hat{p} n_i\right] \mathrm{d}\Gamma. \end{aligned} \tag{3.74}$$

As a result of the shape perturbations, the boundary conditions of the design surface undergo variations, $\delta \bar{u}_i \neq 0$. Both the local variation and the convective variation due to surface normal perturbation have to be considered. The Dirichlet boundary condition postulated for the old flow at the old boundary position also needs to be satisfied by the new flow on the new geometry:

$$\bar{u}_i^{\text{old}} = \bar{u}_i^{\text{new}} \quad \text{on} \quad \Gamma_{\text{D}}. \tag{3.75}$$

Developing the boundary condition for the new flow to second-order accuracy about the old position (STÜCK, 2011):

$$\bar{u}_i^{\text{new}} \approx \bar{u}_i^{\text{old}} + \delta \bar{u}_i + \delta n \frac{\partial \bar{u}_i^{\text{old}}}{\partial n} \quad \text{on} \quad \Gamma_{\text{D}}, \tag{3.76}$$

the local variation of velocity is approximated by:

$$\delta \bar{u}_i \approx -\delta n \frac{\partial \bar{u}_i}{\partial n} \quad \text{on} \quad \Gamma_{\text{D}}. \tag{3.77}$$

Thereafter, Eq. (3.74) looks like:

$$\begin{aligned}\delta L &= \int_{\Gamma_\mathrm{O}\cap\Gamma_\mathrm{D}} \delta n \left(\frac{\partial J_\Gamma}{\partial n} - \frac{\partial \bar{u}_i}{\partial n}\frac{\partial J_\Gamma}{\partial \bar{u}_i}\right) \mathrm{d}\Gamma - \int_{\Gamma_\mathrm{D}} \delta n \frac{\partial \bar{u}_i}{\partial n}\left[\mu_\mathrm{eff}\left(\frac{\partial \hat{u}_i}{\partial n} + \frac{\partial \hat{u}_n}{\partial x_i}\right) - \hat{p} n_i\right] \mathrm{d}\Gamma,\\ &= \int_{\Gamma_\mathrm{O}\cap\Gamma_\mathrm{D}} \delta n \left(\frac{\partial J_\Gamma}{\partial n} - \frac{\partial \bar{u}_i}{\partial n}\frac{\partial J_\Gamma}{\partial \bar{u}_i}\right) \mathrm{d}\Gamma - \int_{\Gamma_\mathrm{D}} \delta n \left[\mu_\mathrm{eff}\left(\frac{\partial \hat{u}_i}{\partial n} + \frac{\partial \hat{u}_n}{\partial x_i}\right)\frac{\partial \bar{u}_i}{\partial n} - \hat{p}\frac{\partial \bar{u}_n}{\partial n}\right] \mathrm{d}\Gamma,\\ &= \int_{\Gamma_\mathrm{O}\cap\Gamma_\mathrm{D}} \delta n \left(\frac{\partial J_\Gamma}{\partial n} - \frac{\partial \bar{u}_i}{\partial n}\frac{\partial J_\Gamma}{\partial \bar{u}_i}\right) \mathrm{d}\Gamma - \int_{\Gamma_\mathrm{D}} \delta n \left[\mu_\mathrm{eff}\left(\frac{\partial \hat{u}_i}{\partial n} + \frac{\partial \hat{u}_n}{\partial x_i}\right)\frac{\partial \bar{u}_i}{\partial n}\right] \mathrm{d}\Gamma. \qquad (3.78)\end{aligned}$$

In light of all the simplifications, the gradient is finally calculated based on Eqs. (2.16) and (3.78) as:

$$\delta L = G\delta n \quad \text{with} \quad G = \int_{\Gamma_\mathrm{D}} \left[-\mu_\mathrm{eff}\left(\frac{\partial \hat{u}_i}{\partial n} + \frac{\partial \hat{u}_n}{\partial x_i}\right)\frac{\partial \bar{u}_i}{\partial n} + G_\mathrm{var}\right] \mathrm{d}\Gamma, \qquad (3.79)$$

and

$$G_\mathrm{var} = \begin{cases} \dfrac{\partial J_\Gamma}{\partial n} - \dfrac{\partial J_\Gamma}{\partial \bar{u}_i}\dfrac{\partial \bar{u}_i}{\partial n} & \text{on} \quad \Gamma_\mathrm{D}\cap\Gamma_\mathrm{O}, \\ 0 & \text{on} \quad \Gamma_\mathrm{D}\setminus\Gamma_\mathrm{O}. \end{cases} \qquad (3.80)$$

In this sense, the gradient of the objective function can be interpreted as sensitivity derivatives evaluated on each mesh element of the design surface. Computing it for the entire design surface creates a sensitivity surface map (OTHMER, 2008). Accordingly, sensitivity derivatives with negative values indicate that an outward movement ($\delta n > 0$) of the surface minimizes the objective function. On the other hand, positive values indicate that the surface has to move inward ($\delta n < 0$) to get an improvement.

3.1.3.3 Minimizing total pressure losses

The loss in total pressure of a fluid dynamics device can be computed in terms of the net energy flux through the inlet Γ_in and outlet Γ_out boundaries:

$$J = -\int_{\Gamma_\mathrm{in}} \left[\bar{p} + \frac{\rho}{2}(\bar{u}_j)^2\right] \bar{u}_i n_i \,\mathrm{d}\Gamma - \int_{\Gamma_\mathrm{out}} \left[\bar{p} + \frac{\rho}{2}(\bar{u}_j)^2\right] \bar{u}_i n_i \,\mathrm{d}\Gamma. \qquad (3.81)$$

For this objective function, it is given that:

$$J_\Omega = 0 \quad \text{on} \quad \Omega, \tag{3.82}$$

and

$$J_\Gamma = \begin{cases} -\left[\bar{p} + \frac{\rho}{2}(\bar{u}_j)^2\right]\bar{u}_i n_i & \text{on} \quad \Gamma_{\text{in}} \text{ and } \Gamma_{\text{out}}, \\ \\ 0 & \text{on} \quad \Gamma \setminus (\Gamma_{\text{in}} \cup \Gamma_{\text{out}})\,. \end{cases} \tag{3.83}$$

So, the derivatives needed to compute the boundary conditions are:

$$\frac{\partial J_\Gamma}{\partial \bar{u}_i} = -\left[\bar{p} + \frac{\rho}{2}(\bar{u}_j)^2\right] n_i - \rho\bar{u}_j\bar{u}_i n_i \quad \text{on} \quad \Gamma_{\text{in}} \text{ and } \Gamma_{\text{out}}, \tag{3.84}$$

and

$$\frac{\partial J_\Gamma}{\partial \bar{p}} = -\bar{u}_i n_i \quad \text{on} \quad \Gamma_{\text{in}} \text{ and } \Gamma_{\text{out}}. \tag{3.85}$$

From Eqs. (3.54) and (3.60), the adjoint velocity on the inlet and wall boundaries is obtained by:

$$\hat{u}_i = \begin{cases} \bar{u}_i & \text{on} \quad \Gamma_{\text{in}}, \\ \\ 0 & \text{on} \quad \Gamma_{\text{wall}}, \end{cases} \tag{3.86}$$

whereas according to Eqs. (3.67) to (3.69), the adjoint conditions on the outlet are:

$$\hat{p} = \rho\bar{u}_n(\hat{u}_n - \bar{u}_n) + \mu_{\text{eff}}\frac{\partial \hat{u}_n}{\partial n} - \frac{\rho}{2}(\bar{u}_j)^2 \quad \text{on} \quad \Gamma_{\text{out}}, \tag{3.87}$$

$$\rho\bar{u}_n(\hat{u}_t - \bar{u}_t) + \mu_{\text{eff}}\frac{\partial \hat{u}_t}{\partial n} = 0 \quad \text{on} \quad \Gamma_{\text{out}}, \tag{3.88}$$

$$\rho\bar{u}_n(\hat{u}_s - \bar{u}_s) + \mu_{\text{eff}}\frac{\partial \hat{u}_s}{\partial n} = 0 \quad \text{on} \quad \Gamma_{\text{out}}. \tag{3.89}$$

As $\Gamma_{\mathrm{O}} = \Gamma_{\mathrm{in}} \cup \Gamma_{\mathrm{out}}$ in Eq. (3.81), $\Gamma_{\mathrm{D}} \cap \Gamma_{\mathrm{O}} = \emptyset$, so the sensitivity derivatives for minimizing the total pressure losses of a fluid dynamics system can be estimated from Eqs. (3.79) and (3.80) as:

$$G = -\int_{\Gamma_{\mathrm{D}}} \mu_{\mathrm{eff}} \left(\frac{\partial \hat{u}_i}{\partial n} + \frac{\partial \hat{u}_n}{\partial x_i} \right) \frac{\partial \bar{u}_i}{\partial n} \, \mathrm{d}\Gamma. \tag{3.90}$$

3.2 Numerical-computational modeling

This section presents an overview of the numerical methods and algorithms employed to solve the main problem of the chapter. The work developed in the thesis is supported by the UNSCYFL3D code. This in-house code was developed in the Laboratory of Fluid Mechanics (MFlab) at the Federal University of Uberlândia. Laminar and turbulent flows with particles in both permanent and transient regimes can be simulated with UNSCYFL3D. Amongst many other CFD packages, UNSCYFL3D is based on a finite volume method in order to resolve a flow field depending on its geometrical boundaries and their respective boundary conditions. For this method, the equations presented in the previous section have to be discretized in space.

Until the current research, it was still not possible to optimize the shape of fluid dynamics systems using UNSCYFL3D. However, a module for solving the adjoint equations and performing the sensitivity analysis was implemented and integrated with a mesh adaptation approach.

3.2.1 Finite volume solver

The finite volume method is a method for representing and evaluating PDEs in the form of algebraic equations (LEVEQUE, 2002). Similar to the finite difference method or finite element method, the solution domain is discretized into a finite number of cells. In the finite volume method, the cells of a meshed geometry are control volumes, over which the PDEs are integrated. Volume integrals in PDE that contain divergence terms are converted to surface integrals using the divergence theorem. These terms are then evaluated as fluxes at the faces of each finite volume. Because the flux entering a given volume is equivalent to that leaving the adjacent volume, the finite volume method is conservative, which makes it preferred for simulations involving fluid flows. Furthermore, it is a versatile method that can handle complex geometries and unstructured meshes (VERSTEEG; MALALASEKERA, 2007). In UNSCYFL3D, the Navier-Stokes equations in the incompressible formulation are solved numerically using the finite volume method of Ferziger and Perić (2002) in 3D unstructured meshes of different shaped cells, such as hexahedra, tetrahedra, prisms, and pyramids. The discretization of the advective terms of the linear momentum equations and turbulence closure model equations is done by using the second-order and first-order upwind schemes, respectively, whereas the centered differencing scheme is used for the diffusive terms.

Note that the set of Eqs. (3.3) and (3.12) forms a system of four equations (continuity, linear momentum for $\bar{u}$, $\bar{v}$ and $\bar{w}$) and four unknowns ($\bar{u}$, $\bar{v}$, $\bar{w}$ and $\bar{p}$). Therefore, the velocity components must be determined by the respective linear momentum equations but restricted by the imposed continuity. There is no explicit equation for the pressure, so a numerical procedure must be applied to compute the pressure field and couple it to the velocity field, ensuring that the continuity equation is also satisfied. In UNSCYFL3D, the SIMPLE (Semi-Implicit Method for Pressure-Linked Equations) algorithm is used for the pressure-velocity coupling (PATANKAR, 1980; FERZIGER; PERIĆ, 2002). In this case, the procedure solution of the equations for $\bar{u}$, $\bar{v}$, $\bar{w}$ and $\bar{p}$ is said to be segregated. Thus, a system of linear equations for each of these variables is resolved sequentially and independently by linear system solution methods, e.g., the biconjugate gradient and the algebraic multigrid methods are employed for the linear momentum and pressure correction equations, respectively, in UNSCYFL3D. The process is repeated until all the standard equation residues are reduced to the specified tolerance. Several global iterations, with the solution of linear systems for $\bar{u}$, $\bar{v}$, $\bar{w}$ and $\bar{p}$, may be necessary due to the nonlinear nature of the Navier-Stokes equations and the coupling between the variables. Since the variables converge at different speeds, it is necessary to under-relax the system solutions. The flowchart of the SIMPLE algorithm implemented in UNSCYFL3D is shown Fig. 3.1.

Figure 3.1 – SIMPLE algorithm flowchart.

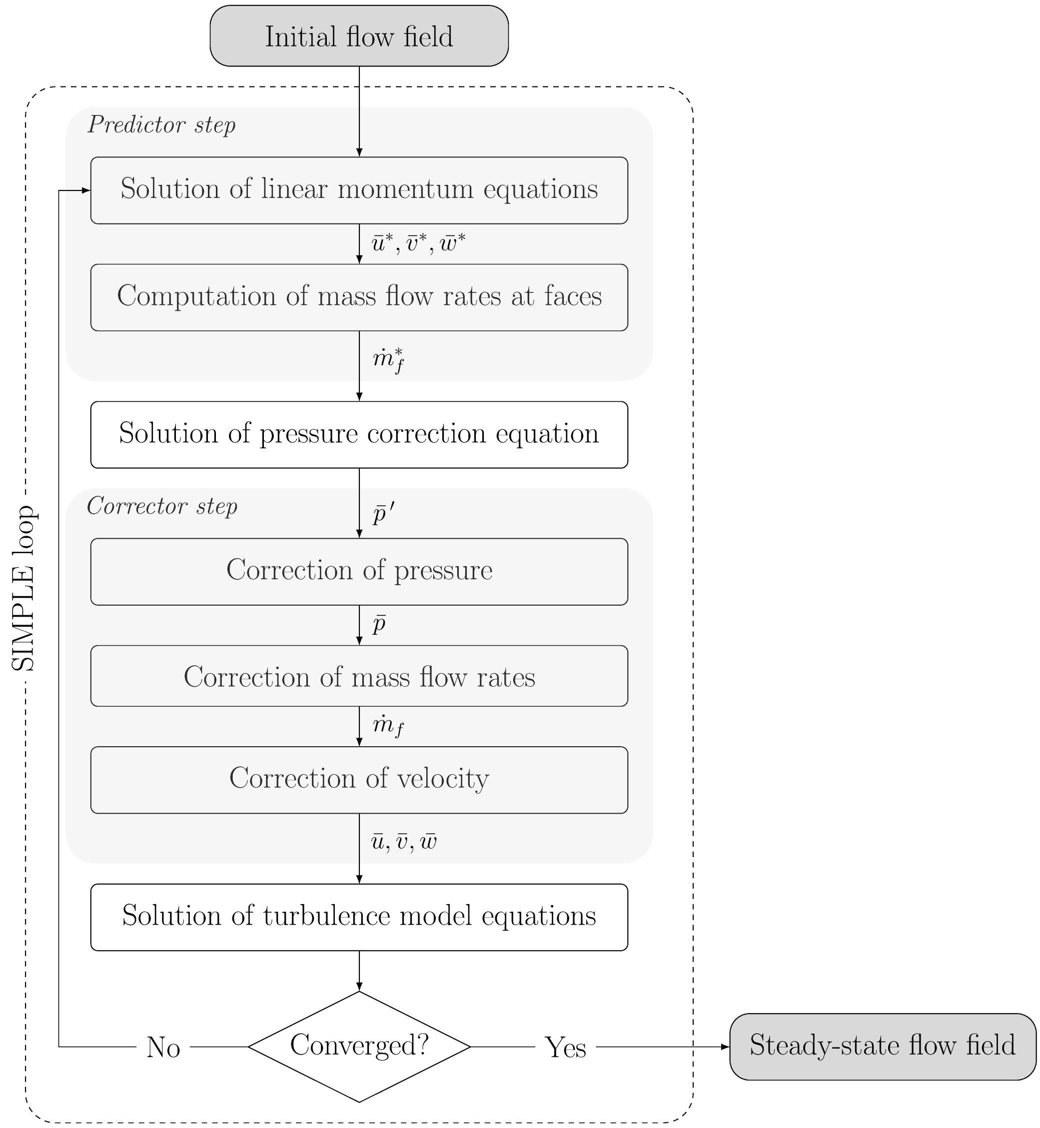

3.2.2 Optimization algorithm

For the sake of code efficiency and maintainability, the adjoint solver is drafted as an add-on module complementing the primal CFD solver. Consistency is ensured by deriving the adjoint discretization schemes from the corresponding primal schemes. The advection scheme is adapted to the inverse transport direction of the adjoint problem. Instead of the second-order upwind scheme, the second-order downwind scheme is applied for the negative advective term in the adjoint equations (KRÖGER; KÜHL; RUNG, 2018). Coding effort is reduced as adjoint discretization and solution methods are taken over from the primal implementation. With some modifications, the primal flow solver is adapted to solve the corresponding adjoint problem. Based on the primal SIMPLE algorithm, a corresponding adjoint pressure-correction procedure is implemented. The adjoint solver developed is general-purpose and also applicable in other fields beyond shape design, like topology optimization.

As the adjoint problem is specific to each objective considered, minor adaptations (hard-coding) are necessary to account for different objective functions. The objective functions for the study cases of this thesis are mainly surface integrals over the domain boundary, so they do not contain a contribution from the interior of the domain, i.e., $J_\Omega = 0$. Consequently, the adjoint equations end up being the same in these cases.

The shape optimization process in UNSCYFL3D is represented by the flowchart shown in Fig. 3.2. The iterative process starts with the baseline mesh corresponding to the original geometry. The primal equations for the flow field are solved within the geometry until convergence, following the procedure of Fig. 3.1. After that, the objective function is evaluated, and the adjoint equations, Eqs. (3.44) and (3.45), are solved until convergence. The sensitivity derivatives are then estimated for the design surface, which

Figure 3.2 – Shape optimization flowchart.

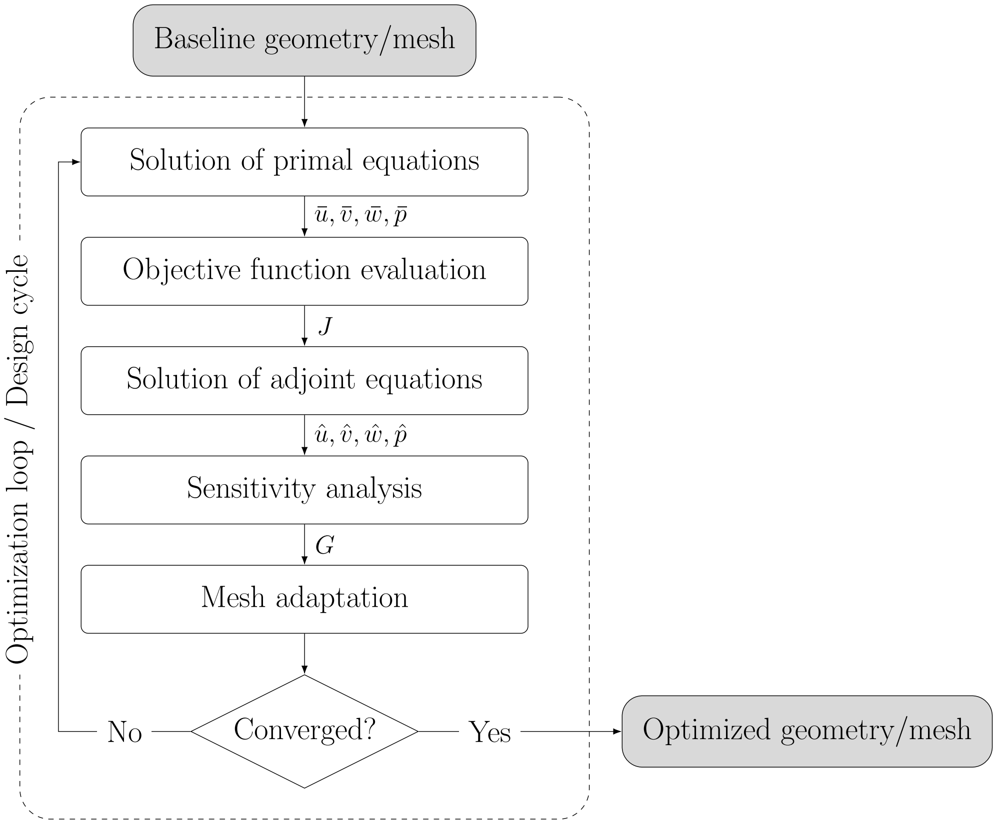

is selected in the code as the zone to be modified. Given the sensitivity derivatives, the mesh is adapted according to a morphing technique, which is detailed in the next section. Lastly, the same steps are repeated until the expected change in the objective function is achieved.

3.2.3 Mesh adaptation

Once the sensitivity map has been computed, the next step is to evaluate whether a specific point on the geometry surface should be shifted inward or outward. This is an important step towards minimizing the objective function.

When solving a CFD problem with an unstructured mesh, one possible and feasible approach for modifying the geometry is to deform the mesh. Therefore, the free-form deformation (FFD) technique (SEDERBERG; PARRY, 1986) is applied in the current work. Basically, this is a technique used to deform 3D objects or surfaces in a smooth and controlled manner. FFD works by defining control points and then deforming the object by manipulating the positions of these control points. The deformation of the object is done in such a way that the shape of the object changes smoothly and naturally, which is the main reason why FFD was chosen. The possibility of modifying the mesh to avoid distortions of the cells is a great advantage.

Thus, considering the FFD technique, a control volume is determined with $l \times m \times o$ control points that surround the region to be modified. Each mesh node q within this control volume is defined by a local coordinate $(\tilde{x}_q, \tilde{y}_q, \tilde{z}_q)$. The deformed position of these nodes in the standard coordinates $\vec{x}_q$ can be calculated as a function of Bernstein polynomials:

$$\vec{x}_q = \sum_{i,j,k=0}^{l,m,o} \vec{\psi}_{ijk} B_{i,l}(\tilde{x}_q) B_{j,m}(\tilde{y}_q) B_{k,o}(\tilde{z}_q), \tag{3.91}$$

in which $\vec{\psi}_{ijk}$ denotes the coordinate of the ijk^{th} control point, and $B_{i,l}(x)$ is the i^{th} Bernstein polynomial of degree l:

$$B_{i,l}(x) = \binom{l}{i} x^i (1-x)^{l-i}, \qquad i = 0, 1, ..., l. \tag{3.92}$$

The adjustment of the control point position is estimated by using a simple gradient-based algorithm for solving minimization problems. Then, the steepest descent method is used, assuming that:

$$\delta\vec{\psi}_{ijk} = -\lambda\vec{\Psi}_{ijk}. \tag{3.93}$$

A smooth deformation of the boundary mesh, in order to improve the design, is guaranteed for a sufficiently small λ step and for the control point sensitivity field $\vec{\Psi}_{ijk}$ given by (ELSAYED, 2015):

$$\vec{\Psi}_{ijk} = \sum_{q} \vec{G}_q B_{i,l}(\tilde{x}_q) B_{j,m}(\tilde{y}_q) B_{k,o}(\tilde{z}_q), \tag{3.94}$$

where $\vec{G}_q$ is the gradient interpolated for $\vec{x}_q$, since G is originally calculated at the center of the faces of the finite volumes.

3.3 Validation and verification studies

The adjoint equations of fluid dynamics have a mathematical and not physical origin, which makes it difficult to compare the results with experimental data. Therefore, assessing the accuracy of adjoint results requires alternative validation and verification strategies. This section explores two concepts for assessing adjoint results, which involve an analytically derived adjoint field solution and sensitivity distributions obtained numerically from other works.

3.3.1 Analytic solution for axis-symmetric Couette flow

The analytic adjoint solution presented by Stück (2011) is considered to validate the adjoint equations. The problem consists of an axis-symmetric Couette flow. This is a classical fluid dynamics problem where laminar fluid flows between two infinitely long coaxial cylinders with a relative angular velocity. In this validation case, the inner cylinder is fixed with a radius of r_i, while the outer one has a radius of r_o and an angular velocity of ω_o, as represented in Fig. 3.3.

Figure 3.3 – Sketch of the Couette flow in cylinder coordinates (r, φ).

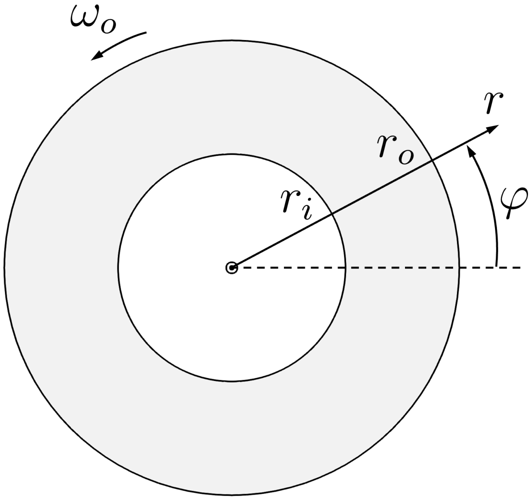

The analytical solution for the primal flow field, in cylinder coordinates (r, φ), is given by:

$$u_r(r) = 0, \tag{3.95}$$

$$u_\varphi(r) = a\left(r - \frac{r_i^2}{r}\right), \tag{3.96}$$

$$p(r) = p(r_i) + \rho a^2\left[\frac{r^2}{2} + 2r_i^2 \ln\left(\frac{r_i}{r}\right) - \frac{r_i^4}{2r^2}\right] \quad \text{with} \quad a = \frac{\omega_o}{1 - (r_i/r_o)^2}. \tag{3.97}$$

Meanwhile, the analytical solution for the adjoint flow field is written as follows:

$$\hat{u}_\varphi(r) = \hat{a}\left(\frac{r}{r_o^2} - \frac{1}{r}\right), \tag{3.98}$$

$$\hat{p}(r) = \hat{p}(r_i) + \rho a \hat{a}\left[\frac{r_i^2 - r^2}{r_o^2} + 2\ln\left(\frac{r}{r_i}\right)\right] \quad \text{with} \quad \hat{a} = \frac{r_i}{(r_i/r_o)^2 - 1}. \tag{3.99}$$

Since variations in the flow field occur only in the radial direction, the Couette flow problem can be considered one-dimensional. However, for simulation purposes, it was solved numerically in a 2D mesh of 100 × 50 cells in circumferential and radial directions, respectively, which is displayed in Fig. 3.4. The Reynolds number based on the width

$\Delta = r_o - r_i$ and the circumferential velocity component of the outer cylinder $u_\varphi(r_o) = u_{\varphi_o}$ was $Re = 100$. This is not an optimization problem, so the primal and adjoint equations were solved just once. Furthermore, the sensitivity derivatives were not calculated as they were not the focus of the validation, and an objective function was not considered.

Figure 3.4 – Mesh of 100 × 50 cells for the Couette flow simulation.

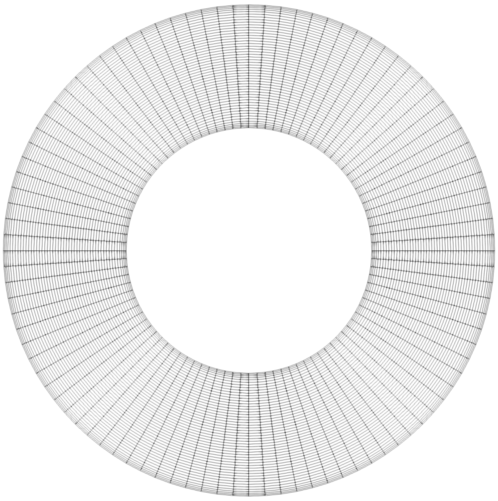

The primal solutions obtained from computational simulation for the circumferential velocity component $u_\varphi(r)$ and pressure $p(r)$ are plotted over the radius in a non-dimensional form in Fig. 3.5 along with the analytic solutions. Both distributions are in

Figure 3.5 – Non-dimensional primal flow field distributions obtained from computational simulation compared against analytic solution.

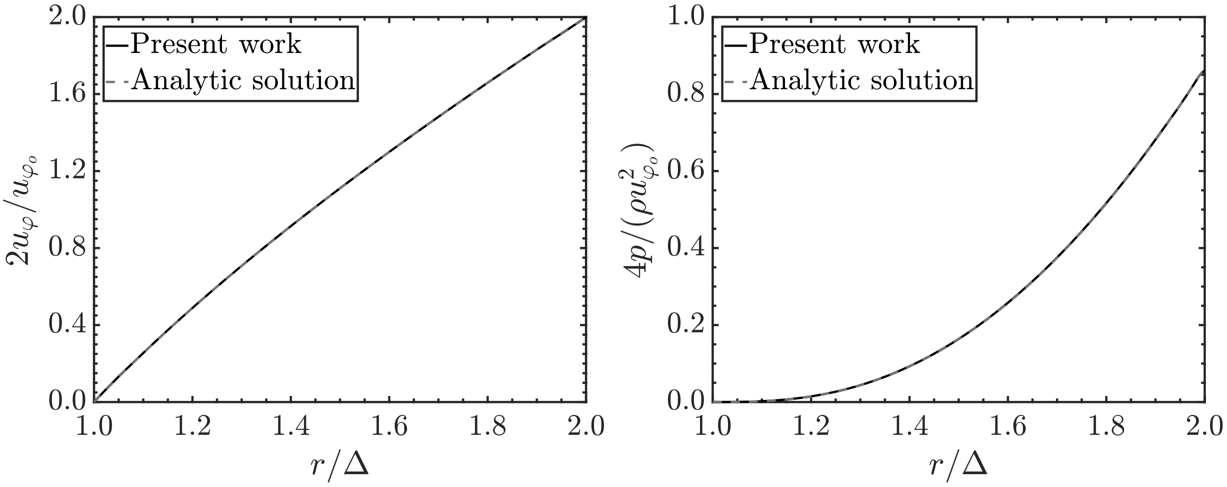

(a) Circumferential velocity component.

(b) Pressure.

agreement with the analytical results.

The non-dimensional distributions of the adjoint circumferential velocity component $\hat{u}_\varphi(r)$ and adjoint pressure $\hat{p}(r)$ are shown in Fig. 3.6. The adjoint results obtained from computational simulation meet the corresponding analytic solution, even in the adjoint pressure distribution, where a slight deviation between the compared results is noticed.

Figure 3.6 – Non-dimensional adjoint flow field distributions obtained from computational simulation compared against analytic solution.

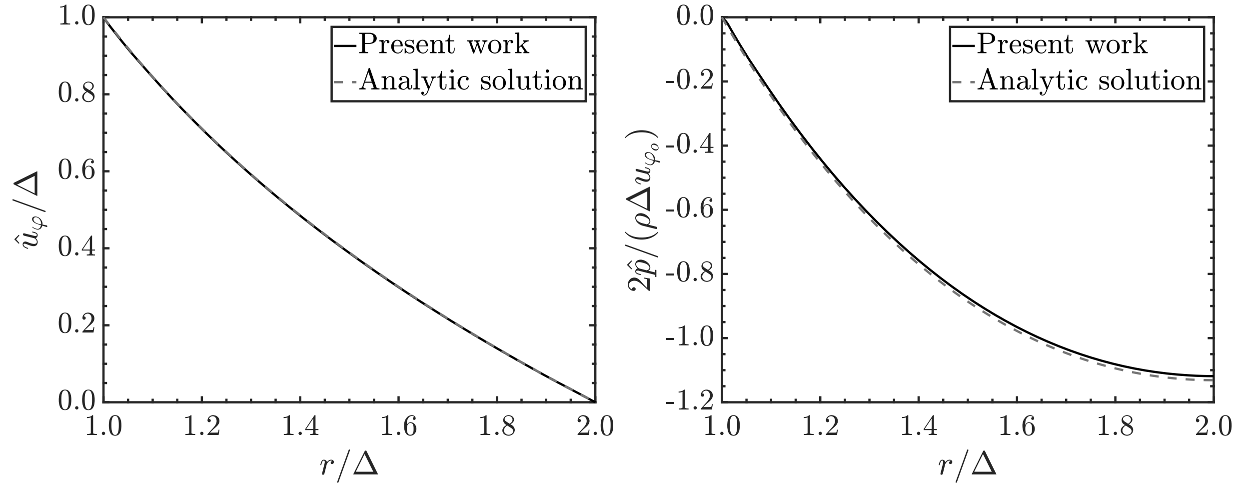

(a) Circumferential adjoint velocity component.

(b) Adjoint pressure.

3.3.2 Sensitivity analysis on S-shaped duct

The purpose of this investigation is to analyze the sensitivity derivatives calculated from UNSCYFL3D concerning the minimization of total pressure losses, Eq. (3.81), of a turbulent flow in an S-shaped duct. The same configuration investigated by Stück (2011) is adopted, which consists of the 2D problem sketched in Fig. 3.7 with a Reynolds number based on the inlet height equal to $Re = 20\,000$.

The simulation was run on a computational mesh with 50×240 cells depicted in Fig. 3.8. The mesh was adequately stretched close to the walls to guarantee that the non-dimensional distance of the first nodes off the wall y^+ was below unit. A uniform velocity was prescribed at the inlet, and the pressure was set to zero at the outlet. For the lower and upper walls, the no-slip condition was applied.

Figure 3.7 – Setup and dimensions for a bent duct configuration.

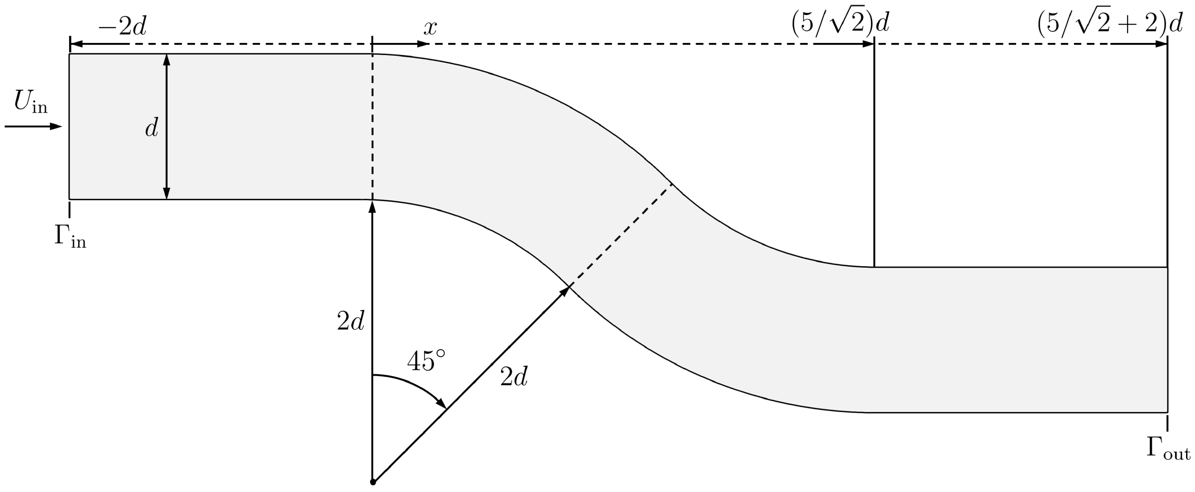

Figure 3.8 – Computational mesh of 50 × 240 cells for the S-shaped duct problem.

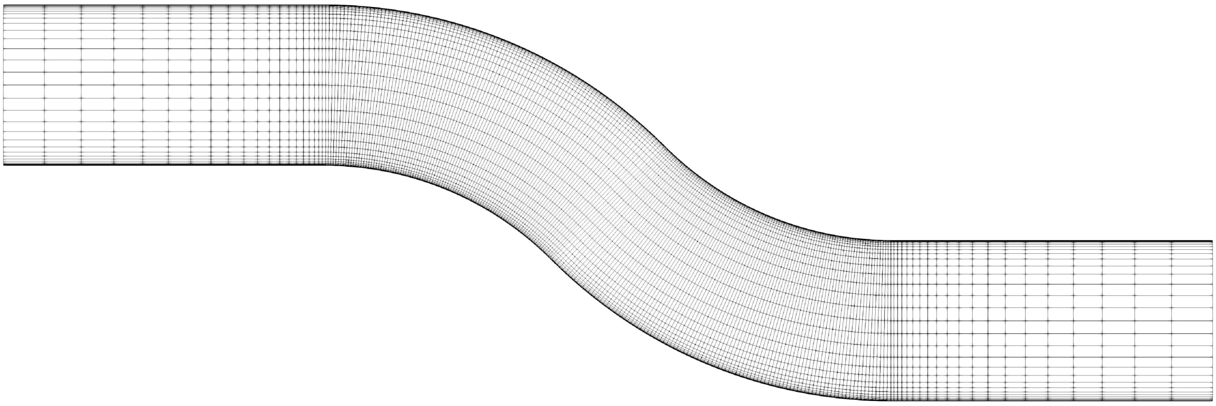

In order to verify the adjoint solver, the sensitivity derivatives obtained from the continuous adjoint calculation, Eq. (3.90), are compared against the results solved via the direct-differentiation method by Stück (2011). The comparison is done for the non-dimensional sensitivity derivatives:

$$G^* = G \frac{d}{\rho U_{\mathrm{in}}^3 a_f}, \tag{3.100}$$

where a_f is the area per unit meter of the respective cell on Γ_{D}. Here, the design surface corresponds to the S-bend section only.

In Stück (2011), the Wilcox k-ω turbulence model was used in conjunction with low Reynolds wall boundary conditions. However, this model is not available in the

UNSCYFL3D code. Therefore, in this study only, the shear-stress transport (SST) model was used to reduce possible differences in the comparison of results due to turbulence closure modeling. The SST turbulence model is a hybrid model that combines the Wilcox k-ω and the k-ε models (MENTER, 1994).

The distribution of the primal and adjoint velocity fields resolved in UNSCYFL3D is plotted in Fig. 3.9. The flow field features a recirculation zone on the lower wall. The rapid expansion of the duct (divergent part) in the S-bend section causes the boundary layer separation. For internal flows, flow separation produces an increase in flow losses. Given the objective of minimizing total pressure losses, it is expected that the sensitivity derivatives exhibit greater magnitudes in this specific region.

Figure 3.9 – Turbulent flow through the S-shaped duct.

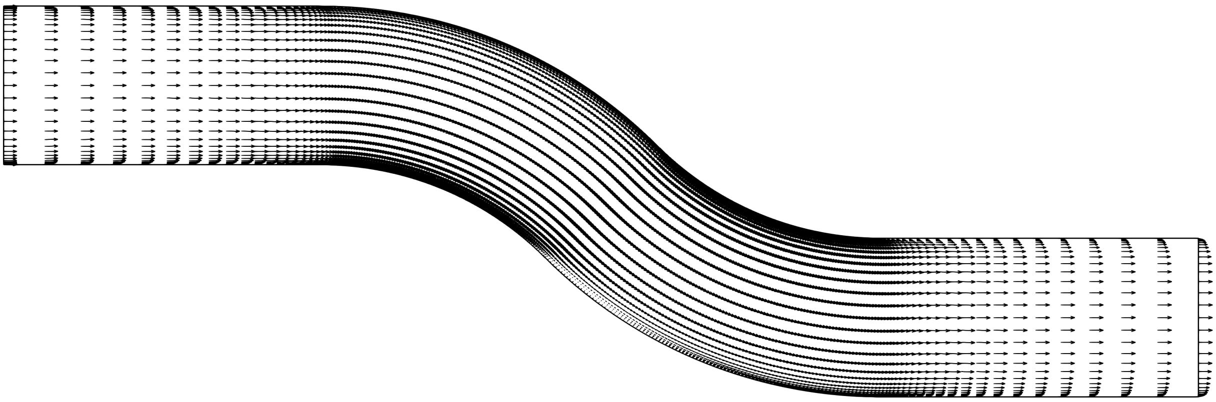

(a) Primal velocity field.

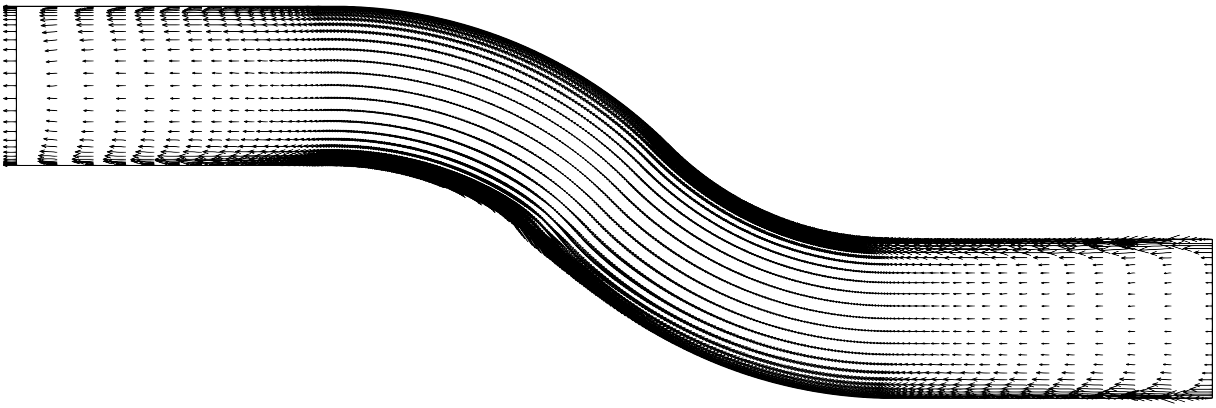

(b) Adjoint velocity field.

In Figure 3.10, the sensitivity distribution is plotted over the duct walls, and its correlation with the flow separation ranging from x_S to x_R is shown in Fig. 3.11. The arrows indicate the direction that the surface should move to minimize the total pressure losses, and they are scaled with the magnitude of the sensitivities. Thus, the cool/warm colors refer to the areas where an outward/inward surface displacement improves the flow passage. The sensitivity distribution clearly reflects the beginning of separation x_S, suggesting a wider duct shape upstream of this point and a reduced duct width downstream, which will intuitively delay the separation.

Figure 3.10 – Non-dimensional sensitivity derivatives G^*.

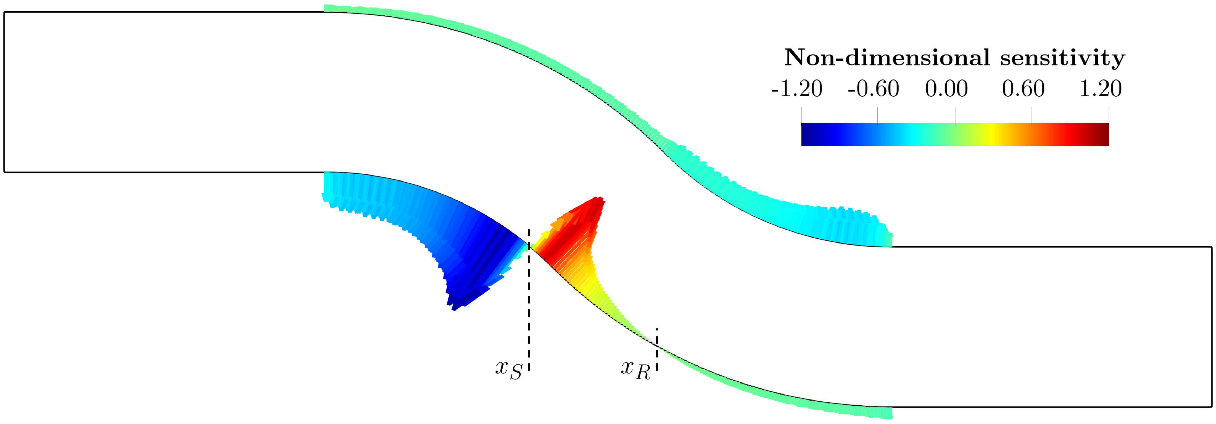

Figure 3.11 – Close-up view of primal flow in divergent part with sensitivity indicators.

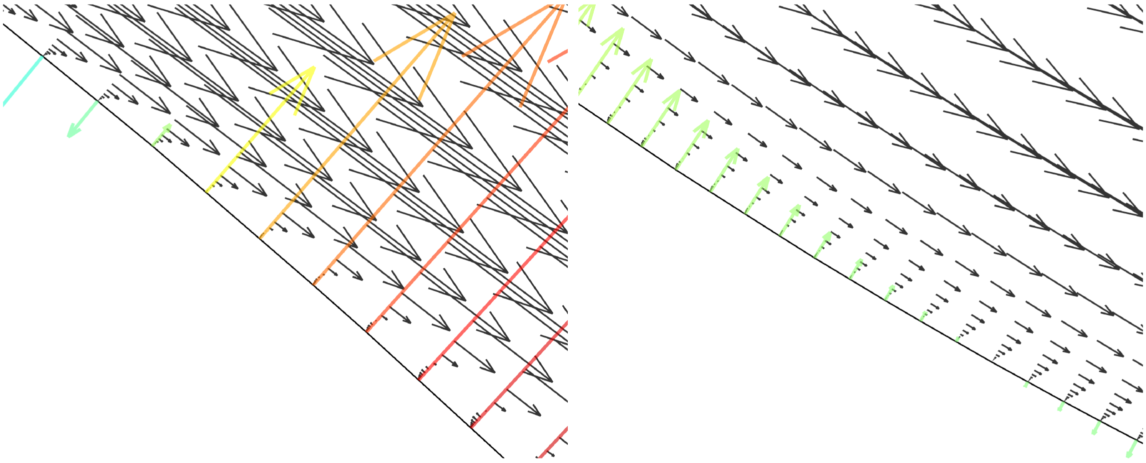

(a) x_S.

(b) x_R.

The adjoint method is verified against the direct-differentiation method in Fig. 3.12. For both upper and lower wall predictions, the sensitivity distributions are in fair agreement. The distributions mainly deviate from the peak predictions, particularly on the lower wall surface. These deviations can be explained by the different turbulence closure models, as different models predict different flow fields, which, in turn, reveal different sensitivity derivatives. Furthermore, the sensitivity derivatives in the direct differentiation method were obtained by integration over Γ_O, which led to smoother distributions. Hence, more pronounced oscillations can be observed in the adjoint case. Finally, the flow separation occurred from $x_S = 1.31d$ to $x_R = 1.89d$ for the direct-differentiation method and from $x_S = 1.28d$ to $x_R = 2.06d$ for the adjoint method. This results in a relative difference of 2.29 % and 8.99 %, respectively.

Figure 3.12 – Non-dimensional sensitivity G^* according to adjoint (present work) and direct-differentiation (STÜCK, 2011) methods.

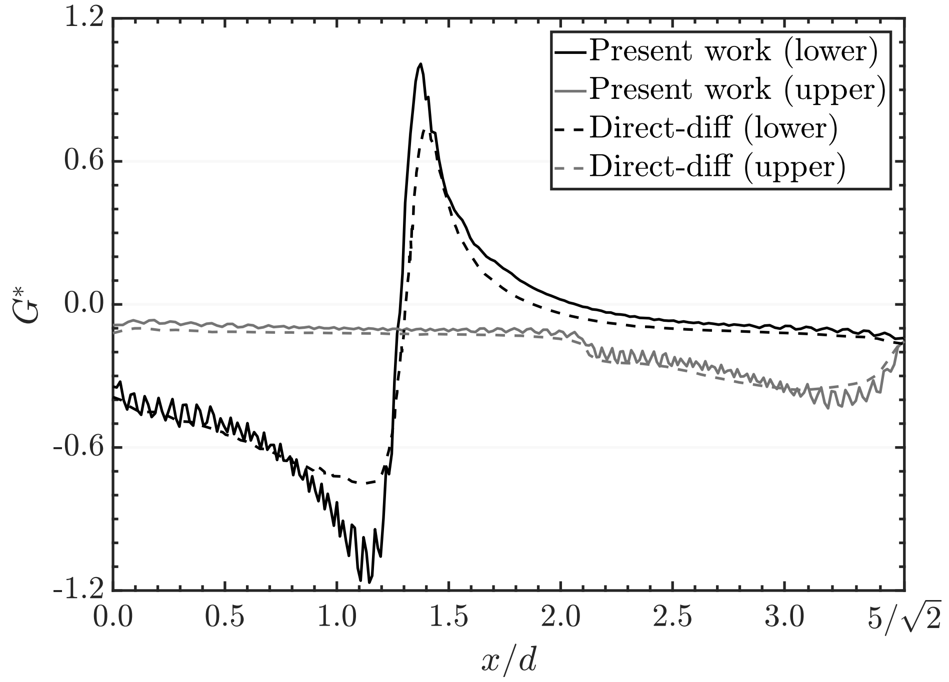

3.4 Results and discussion

The shape optimization carried out in this chapter is related to CFD simulations of three distinct pipeline components found mainly in the transport systems of the oil and gas industry. They all correspond to pipe bends with a diameter of 2.54 cm and a curvature radius of 3.81 cm, but with different curvature angles. The first one is a 45° bend, the second one is a 90° bend, and the last one is a 180° bend, shown in Fig. 3.13, respectively.

Figure 3.13 – Baseline geometries.

(a) 45° bend. (b) 90° bend. (c) 180° bend.

In all three cases, fluid enters a 12.70 cm long vertical pipe and then passes through the bend. In the 45° bend case, fluid comes out of a 10.16 cm long diagonal pipe, whereas in the 90° bend case, fluid comes out of a horizontal pipe of the same length. However, in the 180° bend case, fluid comes out of another 12.70 cm long vertical pipe. A static pressure condition is prescribed at the pipe outlet, and the fluid flow properties, which remain the same across all scenarios, are listed in Tab. 3.1.

Table 3.1 – Fluid flow simulation conditions.

Fluid properties	
Fluid	Air
Specific mass (kg/m^3)	1.225
Dynamic viscosity (Pa·s)	1.79×10^{-5}
Inlet velocity (m/s)	34.1

Turbulence parameters	
Turbulence closure model	two-layer k-ε
Turbulence intensity	5 %

3.4.1 Mesh independence study

Before delving into the shape optimization process, it is crucial to address the issue of mesh independence to determine the appropriate mesh resolution and ensure that the subsequent analyses are based on reliable and consistent numerical simulations. For the sake of brevity, the mesh independence study is presented only for the 90° bend baseline mesh, considering five grid levels.

Unstructured 3D hexahedral meshes were generated with 214 890, 332 640, 476 035, 651 780, and 862 875 cells. Moreover, the pressure drop of the fluid flow was selected as the parameter to assess the mesh independence. After simulating the flow for all meshes, the outcomes were plotted in Fig. 3.14.

Figure 3.14 – Pressure drop for five levels of grid.

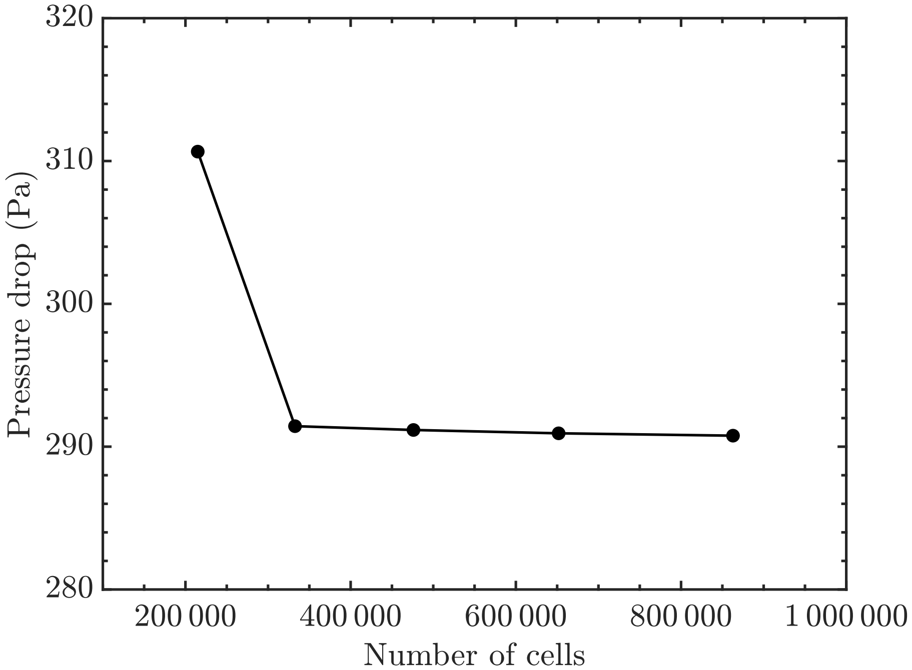

In order to safely evaluate these results, the concept of grid convergence index (GCI) was adopted (ROACHE, 1994). The GCI measures the distance between the simulation results and the asymptotic numerical value. In other words, it indicates how much the solution changes as the mesh is refined. Thus, the GCI method was applied to compare the three finer grids. Following Roache (1994, 1997, 1998), the grid convergence was calculated, and the results are displayed in Tab. 3.2.

Table 3.2 – Details of the mesh independence study based on GCI method.

$\boldsymbol{i}$	$\boldsymbol{N_i}$	$\boldsymbol{\Delta p_i}$ (Pa)	$\mathbf{GCI}^{\mathrm{fine}}_{\boldsymbol{i,i+1}}$ (%)	$\boldsymbol{R_m}$	$\boldsymbol{a_r}$
1	862 875	290.7696			
			0.3454		
2	651 780	290.9348		0.7083	0.9676
			0.4303		
3	476 035	291.1682			

In Table 3.2, $i = 1$, 2, and 3 denote the calculations at the fine, medium, and coarse mesh, N is the number of hexahedral cells, Δp is the computed pressure drop, a_r is a parameter that shows if the solution is in the asymptotic range when close to unity, and R_m is a ratio that can represent a monotonic convergence if less than unity. From the GCI analysis, the results are in the asymptotic range, and a monotonic convergence is observed. Besides that, a reduction in the GCI value for the successive mesh refinements ($\mathrm{GCI}^{\mathrm{fine}}_{1,2} < \mathrm{GCI}^{\mathrm{fine}}_{2,3}$) is identified, meaning the dependence of the numerical results on the cell size has been reduced. Consequently, the third refinement level already guarantees a mesh-independent solution.

Therefore, a mesh with 476 035 cells was adopted in the further simulations on the 90° bend. An adequate near-wall refinement was guaranteed with $y^+ = 1.10$. For the 45° and 180° bends, the meshes were generated based on the mesh of the 90° bend, resulting in 319 725 cells and 781 550 cells, respectively, as illustrated in Fig. 3.15.

3.4.2 Shape optimization

The shape optimization process depicted in Fig. 3.2 was executed for all three pipeline components separately. The process starts with the baseline meshes shown in Fig. 3.15, representing the baseline geometries of Fig. 3.13. The purpose of the optimization is to find new shapes for these geometries with the intention of minimizing the total pressure losses of the fluid flow using the continuous adjoint approach.

Figure 3.15 – Baseline hexahedral meshes.

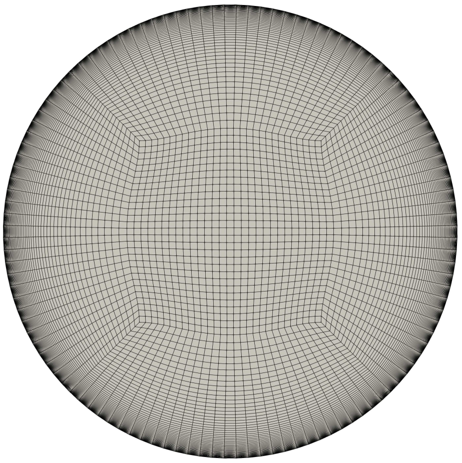

(a) Perpendicular face.

(b) 45° bend - 319 725 cells. (c) 90° bend - 476 035 cells. (d) 180° bend - 781 550 cells.

The steepest descent algorithm was run for $\lambda = 2.40 \times 10^{-5}$ and the shape modification throughout the process was achieved with the FFD technique. Then, in all three cases, a box around the design surface was defined as the control volume with a minimum limit at $(-3.17,\ 7.49,\ -1.61)$ cm and a maximum limit at $(10.79,\ 20.99,\ 1.61)$ cm, and also with $9 \times 9 \times 9$ control points, as illustrated in Fig. 3.16. The coordinate system was positioned at the center of the inlet face. Defining the control volume precisely at the limits of the design surface can lead to abrupt deformations at those points. To ensure a smooth deformation, the control volume was extended slightly beyond the design surface.

Figure 3.16 – Control volumes of the FFD technique around the red design surface.

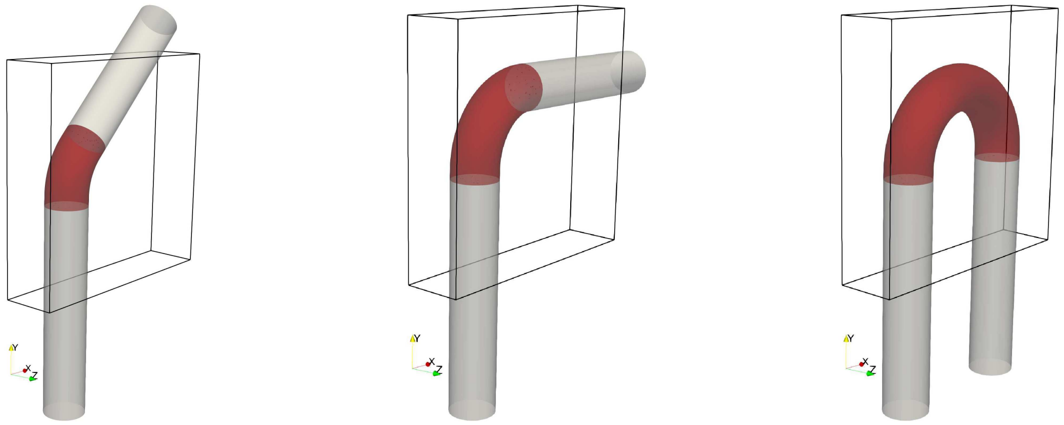

(a) 45° bend.

(b) 90° bend.

(c) 180° bend.

3.4.2.1 Sensitivity analysis

The sensitivity map is computed on the design surface and is updated throughout the iterative process as the mesh changes. In Figure 3.17, the sensitivity map is shown

Figure 3.17 – Sensitivity map for baseline geometry of the 90° bend case.

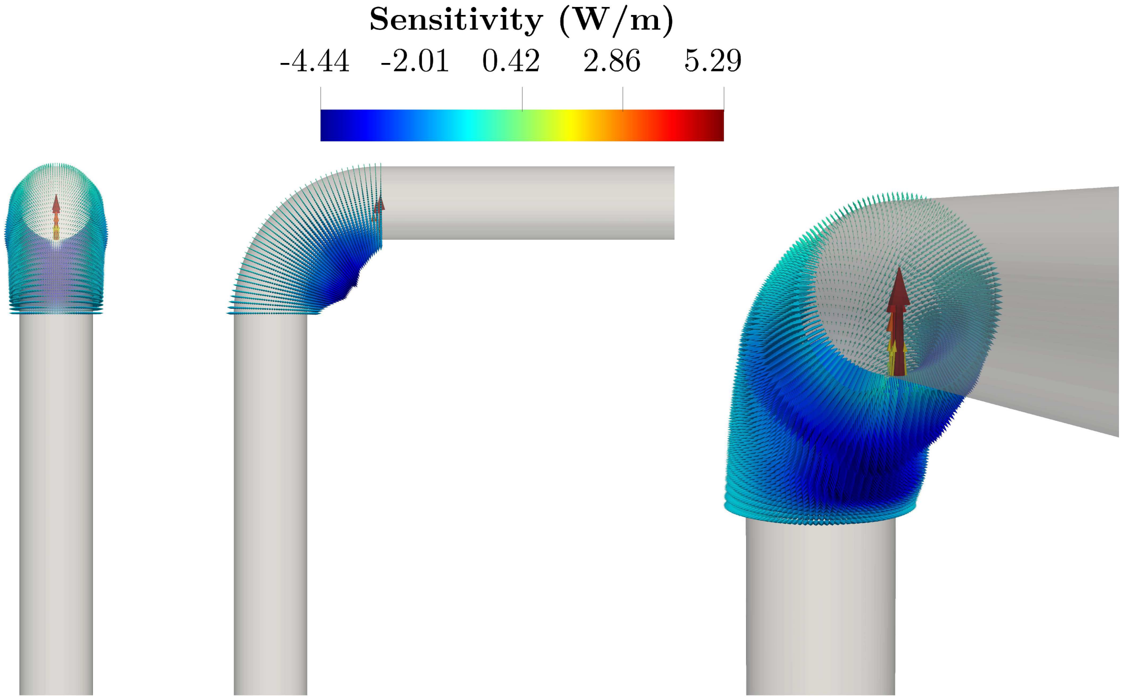

(a) Rear view.

(b) Side view.

(c) Perspective view.

only for the baseline geometry of the 90° to clarify what will happen to the bend. The sensitivities are represented by arrows in the normal direction of the surface scaled with their magnitude. The regions with cool colors correspond to negative values, so the arrows are facing outward, indicating that the mesh deformation should happen in the respective direction. Conversely, regions with warm colors correspond to positive values, and the arrows are facing inward. Hence, a widening of the pipe in the bend region is expected, especially on the intrados, which is the most sensitive part.

3.4.2.2 Objective function evolution

The evolution of the objective function value is plotted in Fig. 3.18. The objective function mostly exhibits a monotonic decrease over the design cycles, except for the 90°

Figure 3.18 – Objective function evolution of all bend cases.

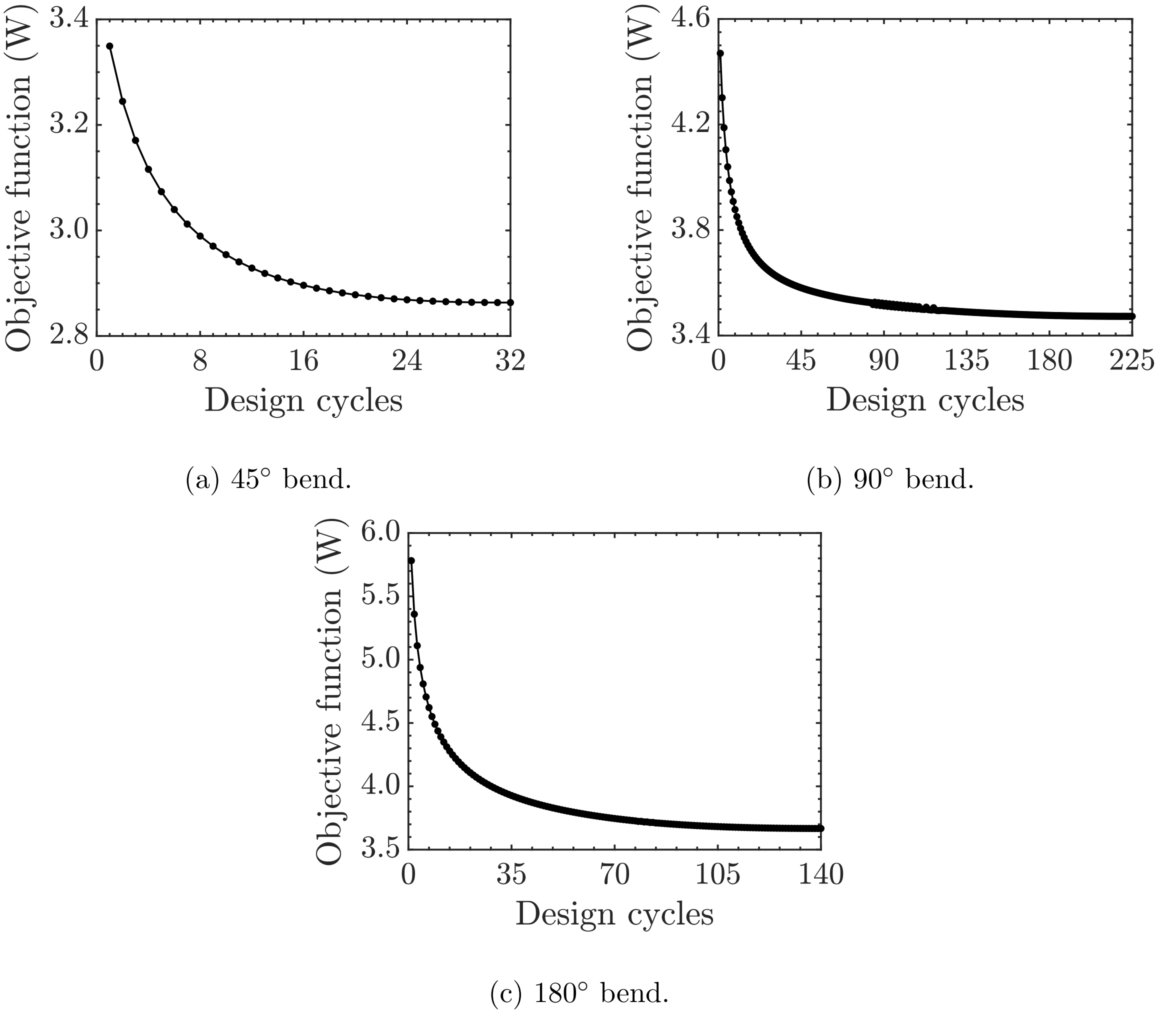

(a) 45° bend.

(b) 90° bend.

(c) 180° bend.

bend case, for which oscillations are observed around 90 design cycles. These oscillations are believed to arise from the assumption of frozen turbulence, in which the approximate adjoint field is obtained by neglecting the variation of the effective viscosity.

Regarding the optimization convergence criterion, the objective function was monitored until the relative difference between the values of two consecutive design cycles was less than 10^{-6}. Approximately 32, 225, and 140 design cycles were necessary for the convergence criterion to be reached in the 45°, 90°, and 180° bend cases, respectively. The convergence of the objective function may be an indication that a local optimum has been found. Nevertheless, the resulting shapes are considered improved designs rather than strict local optima. At the end of the optimization process, the objective function was reduced by 14.51 %, 22.30 %, and 36.50 %, following the previously mentioned order.

The final shapes for minimizing total pressure losses are shown in Fig. 3.19. Evidently, they are non-standard shapes. However, thanks to existing modern and efficient manufacturing techniques, such as additive manufacturing, concerns about their manufacturability are no longer a major problem.

Figure 3.19 – Optimized geometries.

(a) 45° bend.

(b) 90° bend.

(c) 180° bend.

Furthermore, it is worth noting that the optimization process was not hindered by operational or space limitations, allowing for a more flexible exploration of design possibilities. In case limitations arise during the practical implementation of these geometries, one potential solution would involve enforcing restrictions on the nodes of the meshes to prevent deformations beyond the desired bounds and ensure adherence to the required specifications.

Since the mesh cells are deformed, the corresponding values of y^+ change. For this reason, the y^+ of the optimized meshes were checked. The lowest value found was $y^+ = 0.56$ for all bends. The highest value found was $y^+ = 0.82$ for the 45° bend and $y^+ = 1.00$ for both 90° and 180° bends. Therefore, all these values are sufficient to reproduce the near-wall conditions.

3.4.2.3 Comparison between baseline and optimized systems

Overlaying the optimized geometry on the baseline, it can be seen in Fig. 3.20 that the pipe widens in the bend region, but towards the sides, while the most sensitive region (intrados of the bend) does not exhibit major changes. This can be explained by the gradient filtering that occurs when applying the FFD technique. In this way, very sensitive, small regions do not suffer great expansion or contraction. This issue might

Figure 3.20 – Overlapping geometries of the 90° bend case.

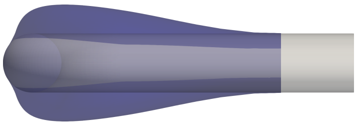

(a) Top view.

(b) Rear view. (c) Side view. (d) Perspective view.

seem to limit the potential of the optimization, but it actually prevents any divergences caused by a very distorted mesh.

Another aspect to be addressed is the behavior of the baseline and optimized system velocity fields represented in Fig. 3.21. Observing the magnitude of the velocity field with the arrows indicating the flow direction, it can be noticed that there is a flow separation in the bend region of the baseline case. The flow separation contributes to the total pressure losses as mentioned in the S-shaped duct investigation (Section 3.3.2). Consequently, such behavior is not observed in the optimized system because the pipe shape was modified so that the total pressure losses of the flow were reduced.

Figure 3.21 – Comparison between baseline and optimized system velocity fields of the 90° bend case.

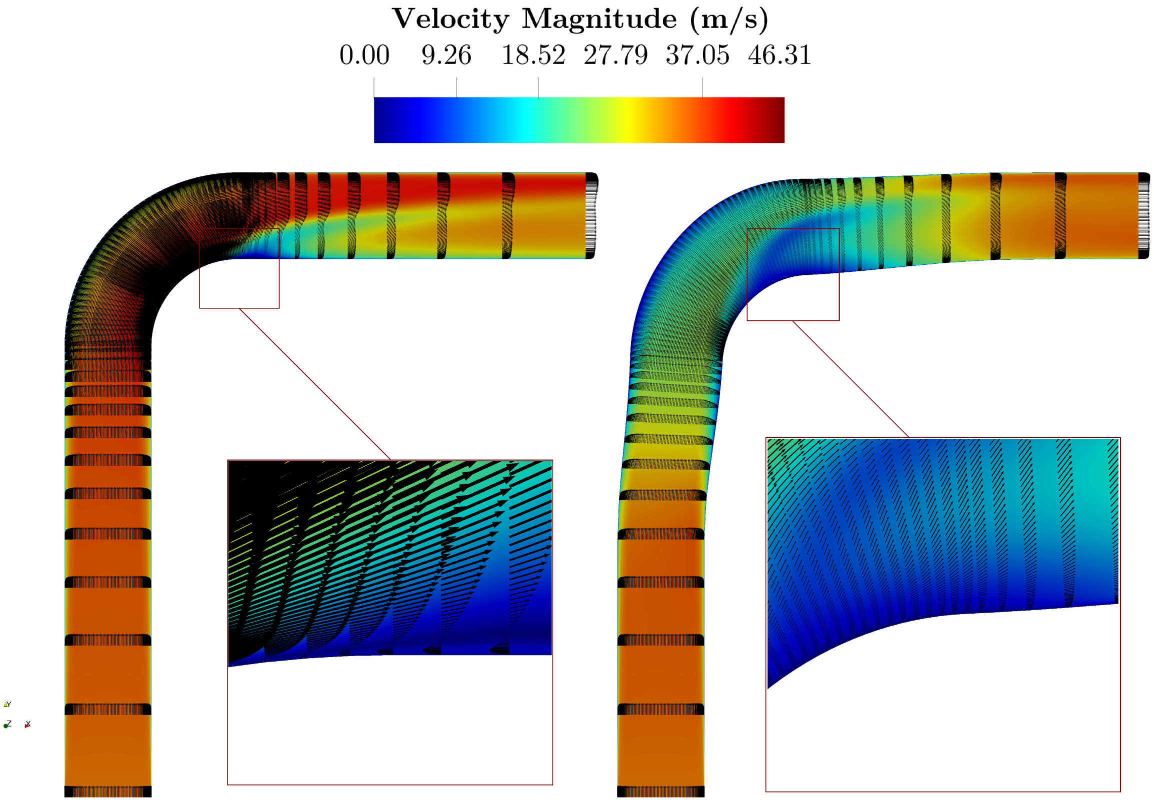

(a) Baseline.

(b) Optimized.

3.5 Conclusions

While the continuous adjoint approach to sensitivity analysis is straightforward to understand, its mathematical development is undeniably complex and demanding. Essentially, as shown in this chapter, the deduction of the continuous adjoint boils down to four tasks:

(i) Formulating the Lagrange function, which comprises the objective function augmented by the constraints weighted by the Lagrange multipliers. This involves integrating the primal equations multiplied by the adjoint variables over the volume of the domain.

(ii) Determining the total variation of the Lagrange function.

(iii) Employing integration by parts to transfer derivatives from local variations to adjoint variables within volume integrals and assuming hypotheses to simplify some terms. This leads to the adjoint equations and boundary conditions reducing the variation of the Lagrange function to integrals applied to the design surface.

(iv) Computing the surface sensitivities using the final expression for the variation of the Lagrange function.

Nevertheless, the implementation of the continuous adjoint solver brings significant advantages, as it allows for leveraging the existing primal solver to effectively implement the adjoint solver. In UNSCYFL3D, the adjoint equations were implemented, tested, and validated, and the gradient for minimizing total pressure losses was verified. This paved the way for investigating shape optimization problems.

To explore the potential of the adjoint method, three types of pipe fittings with different curvature angles (45°, 90°, and 180°) were subjected to shape optimization. The goal was to minimize the total pressure losses of an internal single-phase fluid flow. After successfully reducing the objective function by at least 14 %, the optimization process resulted in unconventional shapes that will be studied from another perspective in the next chapter.

CHAPTER IV

EROSION MITIGATION PROBLEM

The application of adjoint methods to multiphase flows is not yet well established in the literature. There are fundamental limitations to the use of such methods within a Lagrangian framework.

Despite these circumstances, it is intuitively plausible to think that optimizing the carrier flow should also “optimize” the particle flow. By reducing the total pressure losses in a pipe fitting, as seen previously, a more streamlined design is achieved. This, in turn, helps avoid sudden changes in fluid motion and, consequently, in particle path.

As pipeline components are very prone to erosion problems, which can significantly affect the service life of equipment, it is desirable to minimize erosive wear. In this sense, an investigation is performed in this chapter to verify if the shape optimization applied to the fluid flow (as discussed in Chapter 4) favors the mitigation of erosion caused by the impact of particles on pipe walls. The correlation with Stokes number, which characterizes the relationship between fluid and particle flows, is explored as well.

4.1 Mathematical modeling

In erosion problems, the accurate prediction of erosion rates relies on resolving the movement and behavior of particles within a fluid flow. This requires appropriate modeling to capture the interaction between the continuous and dispersed phases. In

UNSCYFL3D code, multiphase flows are modeled using the Euler-Lagrange approach, treating the dispersed phase as Lagrangian particles.

In the previous chapter, the mathematical modeling for the continuous phase was already discussed. Now, attention is turned to dispersed phase modeling and, subsequently, erosion prediction modeling.

4.1.1 Lagrangian particle equations

Since the Lagrangian approach is adopted to track the particles through the domain, the motion of each particle is computed based on Newton's second law. The addressed problems are carried out at low mass loadings, so the coupling between continuous and discrete phases is assumed to be one-way. Thus, the trajectory, linear momentum, and angular momentum equations for a rigid, spherical particle can be written, respectively, as:

$$\frac{dx_{p_i}}{dt} = u_{p_i}, \tag{4.1}$$

$$m_p \frac{du_{p_i}}{dt} = m_p g_i \left(1 - \frac{\rho}{\rho_p}\right) + \underbrace{m_p f_d \left(u_i - u_{p_i}\right)}_{F_{d_i}} + F_{ls_i} + F_{lr_i}, \tag{4.2}$$

$$I_p \frac{d\omega_{p_i}}{dt} = T_i, \tag{4.3}$$

in which x_{p_i} are the coordinates of the particle position, u_{p_i}, and ω_{p_i} are its linear and angular velocity components, m_p and $I_p = 0.1 m_p d_p^2$ are the mass and the moment of inertia for a sphere, while $u_i = \bar{u}_i + u'_i$ are the components of the instantaneous fluid velocity. The average fluid velocity $\bar{u}_i$ is interpolated from the resolved flow field, whereas the fluctuating component u'_i is calculated according to the Langevin dispersion model proposed by Sommerfeld (2001).

The right-hand side of Eq. (4.2) corresponds to the sum of the forces acting on the particle. Its first term represents the weight and buoyancy forces, with g_i being the gravitational acceleration, F_{d_i} being the drag force, F_{ls_i} being the shear-induced lift force, and F_{lr_i} being the rotation-induced lift force. In the case of gas-solid flows, the density of particles is about 1 000 times the gas density. Hence, other forces, such as virtual mass and the Basset force, are neglected since they are unimportant for high ratios of particle to gas densities (LAÍN; SOMMERFELD; KUSSIN, 2002). In Equation (4.3), T_i corresponds to the torque acting on the particle.

The drag arises due to the interaction between the particle and the fluid, resulting in a retarding force that acts opposite to the particle velocity:

$$\vec{F}_d = \frac{\pi}{8}\rho d_p^2 C_d \left\|\vec{u} - \vec{u}_p\right\| (\vec{u} - \vec{u}_p)\,, \tag{4.4}$$

this means that in Eq. (4.2):

$$f_d = \frac{3}{4}\frac{\rho}{\rho_p d_p} C_d \left\|\vec{u} - \vec{u}_p\right\|. \tag{4.5}$$

The drag coefficient C_d is defined as a function of the particle Reynolds number:

$$Re_p = \frac{\rho d_p \left\|\vec{u} - \vec{u}_p\right\|}{\mu}, \tag{4.6}$$

using the empirical correlation proposed by Schiller and Naumann (1935):

$$C_d = \begin{cases} \dfrac{24}{Re_p}\left(1 + 0.15\,Re_p^{0.687}\right) & \text{if } \; Re_p \leq 1\,000, \\ \\ 0.44 & \text{if } \; Re_p > 1\,000. \end{cases} \tag{4.7}$$

When a particle is suspended in a fluid and subjected to shear flow, the difference in fluid velocity between the particle surface and the surrounding fluid leads to a variation in shear stress. This variation produces a lift force that acts perpendicular to the flow direction. The shear-induced lift force is calculated based on the analytical result of Saffman (1965):

$$\vec{F}_s = \frac{\pi}{8}\rho d_p^3 C_{ls} \left[(\vec{u} - \vec{u}_p) \times \vec{\omega}\right], \tag{4.8}$$

and extended for higher particle Reynolds numbers by considering the following coefficient (MEI, 1992):

$$C_{ls} = \begin{cases} \dfrac{4.1126}{\sqrt{Re_s}} \left[\left(1 - 0.3314\sqrt{b}\right) \exp\left(-0.1\,Re_p\right) + 0.3314\sqrt{b} \right] & \text{if } Re_p \leq 40, \\ \dfrac{4.1126}{\sqrt{Re_s}} \left(0.0524\sqrt{bRe_p}\right) & \text{if } Re_p > 40, \end{cases} \tag{4.9}$$

where $b = 0.5Re_s/Re_p$ is valid for $0.005 < b < 0.4$, and the particle Reynolds number of the shear flow is determined as a function of the fluid vorticity $\vec{\omega} = \nabla \times \vec{u}$:

$$Re_s = \frac{\rho d_p^2 \left\|\vec{\omega}\right\|}{\mu}. \tag{4.10}$$

When a particle rotates while moving through a fluid, the velocity of the fluid relative to the particle surface differs between the sides that are moving with the fluid and the sides that are moving against the fluid. As a result, a difference in the pressure distribution around the particle arises, generating a lift force. This phenomenon is also known as the Magnus effect, and the rotation-induced lift force is computed by the relation of Rubinow and Keller (1961):

$$\vec{F}_{lr} = \frac{\pi}{8}\rho d_p^3 \frac{Re_p}{Re_r} C_{lr} \left[\vec{\Omega} \times \left(\vec{u} - \vec{u}_p\right)\right], \tag{4.11}$$

where the lift coefficient is estimated from the correlation proposed by Lun and Liu (1997):

$$C_{lr} = \begin{cases} \dfrac{Re_r}{Re_p} & \text{if } Re_p \leq 1, \\ \dfrac{Re_r}{Re_p}\left(0.178 + 0.822Re_p^{-0.522}\right) & \text{if } Re_p > 1, \end{cases} \tag{4.12}$$

with $\vec{\Omega} = 0.5\nabla \times \vec{u} - \vec{\omega}_p$, and the Reynolds number of particle rotation is given by:

$$Re_r = \frac{\rho d_p^2 \|\vec{\Omega}\|}{\mu}. \tag{4.13}$$

Moreover, the rotating particle experiences torque from the fluid flow, which is evaluated using the extended version of the equation presented by Rubinow and Keller (1961) to account for the relative motion between fluid and particle at a higher Reynolds number:

$$\vec{T} = \frac{1}{64} \rho d_p^5 C_r \, \|\vec{\Omega}\| \, \vec{\Omega}. \tag{4.14}$$

The coefficient of rotation C_r is then obtained from Rubinow and Keller (1961) and the direct numerical simulations of Dennis, Singh, and Ingham (1980):

$$C_r = \begin{cases} \dfrac{64\pi}{Re_r} & \text{if } \; Re_r \leq 32, \\ \\ \dfrac{12.9}{\sqrt{Re_r}} + 128.4/Re_r & \text{if } \; 32 < Re_r \leq 1\,000. \end{cases} \tag{4.15}$$

4.1.2 Particle-wall collision

In flows involving wall boundaries, particles may end up colliding with these walls depending on their trajectory. Therefore, modeling the particle-wall interaction is important to properly simulate the particle path. The forces acting on particles during the particle-wall collision include the wall repulsion force, which prevents the particles from penetrating the wall, and the restitution force, which accounts for the energy transfer between the particle and the wall during the collision.

Upon a particle colliding with a wall, its trajectory is affected by the energy lost. Thus, the inelastic hard-sphere collision model is adopted, in which the particle is assumed to be a homogeneous and non-deformable sphere, and the wall is also considered non-deformable. The particle linear and angular velocities after rebound are then updated (BREUER; ALLETTO; LANGFELDT, 2012). In case of a no-sliding collision, $\|\vec{u}_{pr}^-\| \leq \frac{7}{2} (1+e) \left(\vec{u}_p^- \cdot \vec{n}\right) \mu_s$, it is given that:

$$\vec{u}_p^+ = \vec{u}_p^- - \frac{2}{7} \vec{u}_{pr}^- - (1+e) \left(\vec{u}_p^- \cdot \vec{n}\right) \vec{n}, \tag{4.16}$$

$$\vec{\omega}_p^+ = \vec{\omega}_p^- - \frac{10}{7} \frac{1}{d_p} \vec{n} \times \vec{u}_{pr}^-, \tag{4.17}$$

and in case of sliding collision:

$$\vec{u}_p^+ = \vec{u}_p^- - (1+e)\left(\vec{u}_p^- \cdot \vec{n}\right)\left[\mu_d \frac{\vec{u}_{pr}^-}{\|\vec{u}_{pr}^-\|} + \vec{n}\right], \tag{4.18}$$

$$\vec{\omega}_p^+ = \vec{\omega}_p^- - \frac{5}{d_p}(1+e)\left(\vec{u}_p^- \cdot \vec{n}\right)\frac{\mu_d}{\|\vec{u}_{pr}^-\|}\vec{n} \times \vec{u}_{pr}^- . \tag{4.19}$$

In the above equations, the superscripts $-$ and $+$ denote values prior to and after the collision, respectively. The restitution coefficient e as well as the static μ_s and dynamic μ_d friction coefficients are associated with the material properties of the particle-wall pair, and the relative velocity $\vec{u}_{pr}$ at the contact point between the particle and the wall is defined as:

$$\vec{u}_{pr} = \vec{u}_p - \left(\vec{u}_p^- \cdot \vec{n}\right)\vec{n} + \frac{d_p}{2}\vec{\omega}_p \times \vec{n}, \tag{4.20}$$

with $\vec{n}$ being the normal unit vector pointing outwards of the element face being impacted. The configuration considering a smooth specular wall is sketched in Fig. 4.1.

The energy lost is evaluated using the rebound model of Grant and Tabakoff (1975):

$$e = 0.993 - 1.76\alpha - 1.56\alpha^2 - 0.49\alpha^3, \tag{4.21}$$

where α is the impact angle between the particle trajectory and the wall. However, wall roughness is known to have a significant influence on particle-laden wall-bounded flows directly affecting the particulate phase (LAÍN; SOMMERFELD; KUSSIN, 2002; BREUER; ALLETTO; LANGFELDT, 2012). For simulating the wall roughness effect, a stochastic approach is adopted (SOMMERFELD; HUBER, 1999) by assuming that the effective impact angle α_{eff} is composed of the particle trajectory angle and a stochastic contribution due to wall roughness:

$$\alpha_{\text{eff}} = \alpha + \xi\,\Delta\gamma. \tag{4.22}$$

This stochastic contribution may be approximated by a normal distribution function with a standard deviation of $\Delta\gamma$. Hence, ξ represents a Gaussian random variable with zero mean and a standard deviation of one. The value of $\Delta\gamma$ depends on the structure of the wall roughness and additionally on the particle size.

Figure 4.1 – Sketch of the particle colliding with a wall and the definitions used.

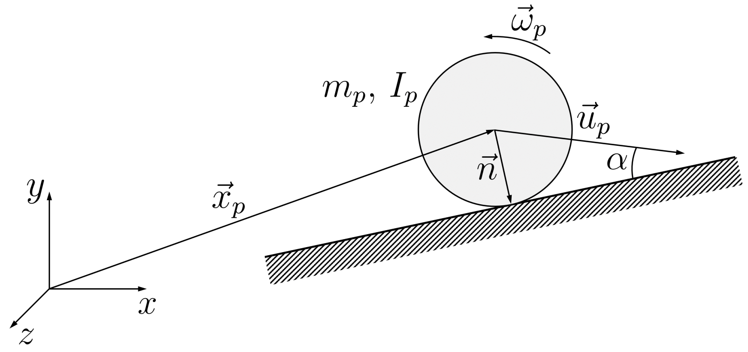

4.1.3 Erosion equations

As particle-wall collisions occur, the erosion damage can be estimated. Therefore, the penetration ratio is computed with Eqs. (2.6) and (2.7), which depends on the erosion ratio E. The erosion ratio, in turn, denotes a unit of eroded material per mass of particles, and it is calculated according to the predictive equation proposed by Oka, Okamura, and Yoshida (2005):

$$E(\alpha) = g(\alpha)\,E_{90}, \tag{4.23}$$

where $g(\alpha)$ represents the impact angle dependence and E_{90} is the erosion damage at the normal impact angle. The first parameter is expressed by two trigonometric functions and by the initial eroded material Vickers hardness number Hv in GPa:

$$g(\alpha) = (\sin\alpha)^{n_1}\left[1 + \mathrm{Hv}(1-\sin\alpha)\right]^{n_2}. \tag{4.24}$$

The second parameter is related to the impact velocity, particle diameter, and eroded material hardness, and it is formulated as follows:

$$E_{90} = K\,(a\,\mathrm{Hv})^{k_1\,b}\left(\frac{u_p}{u_{\mathrm{ref}}}\right)^{k_2}\left(\frac{d_p}{d_{\mathrm{ref}}}\right)^{k_3}. \tag{4.25}$$

The exponents n_1 and n_2 in Eq. (4.24) show the effects of repeated plastic deformation and cutting action, and they are determined by the eroded material hardness and other impact conditions, such as particle properties and shape. Meanwhile, u_{ref} and d_{ref} in Eq. (4.25) are the reference impact velocity and particle diameter used in the experiments from Oka, Okamura, and Yoshida (2005). The exponents k_2 and k_3 are obtained by particle properties, but k_2 is also determined by the Vickers hardness of the eroded material. Lastly, the term $K\,(a\,\text{Hv})^{k_1\,b}$ is highly dependent on the type of particle and eroded material Vickers hardness, which are not correlated with the impact conditions and other factors. Since the SiO_2-aluminum pair is considered in the current work, the following expressions are used (DUARTE, 2017):

$$\begin{aligned}
&n_1 = 0.71\,(\text{Hv})^{0.14}, \quad n_2 = 2.4\,(\text{Hv})^{-0.94},\\
&k_2 = 2.3\,(\text{Hv})^{0.038}, \quad k_3 = 0.19,\\
&K\,(a\,\text{Hv})^{k_1\,b} \approx 81.714\,(\text{Hv})^{-0.79}.
\end{aligned} \tag{4.26}$$

4.2 Numerical-computational modeling

A brief description of dispersed phase numerical methods is presented in this section. It is worth mentioning that any information provided here is in accordance with the UNSCYFL3D code. For more details, the interested reader can refer to Salvo (2013).

In the Lagrangian framework, the parcel concept is employed. Therefore, each computational particle represents a number of real particles with the same properties, such as size and velocity. The linear and angular velocities of each computational particle are given by the analytical integration of the ordinary differential equations, Eqs. (4.2) and (4.3). These equations depend on information related to the continuous phase. Hence, an accurate interpolation scheme is required to determine the fluid properties at the particle position. In this case, Sheppard's scheme is considered, which consists of calculating the velocity and vorticity components by weighing the neighboring cell values with their inverse distances from their centers to the particle position (SALVO, 2013). In order to interpolate the fluid properties, it is important to know the location of each computational particle within the Eulerian mesh. When a structured grid is used, determining the cell hosting the particle is simple, as there is a straightforward relationship between the cell index and its physical location. However, the in-house code is based on unstructured grids, so it requires a specific algorithm to track the computational particles. For this purpose, the particle tracking algorithm proposed by Haselbacher, Najjar, and Ferry (2007) is used. Within this algorithm, if it is detected that the particle trajectory intersects any of the domain boundaries, the application of the corresponding boundary condition, such as reflect (particle-wall collision model) or escape, is triggered.

Given the assumption of one-way coupling, the fluid flow does not "feel" the presence of the particles, so there is no need for a coupled solution of the continuous and dispersed phases. First, the steady-state solution for the fluid phase without particles is computed. Afterwards, the computational particles are injected into this flow field with a certain frequency within a time loop, and their motion is then simulated according to the flowchart shown in Fig. 4.2.

Figure 4.2 – Lagrangian particle flowchart.

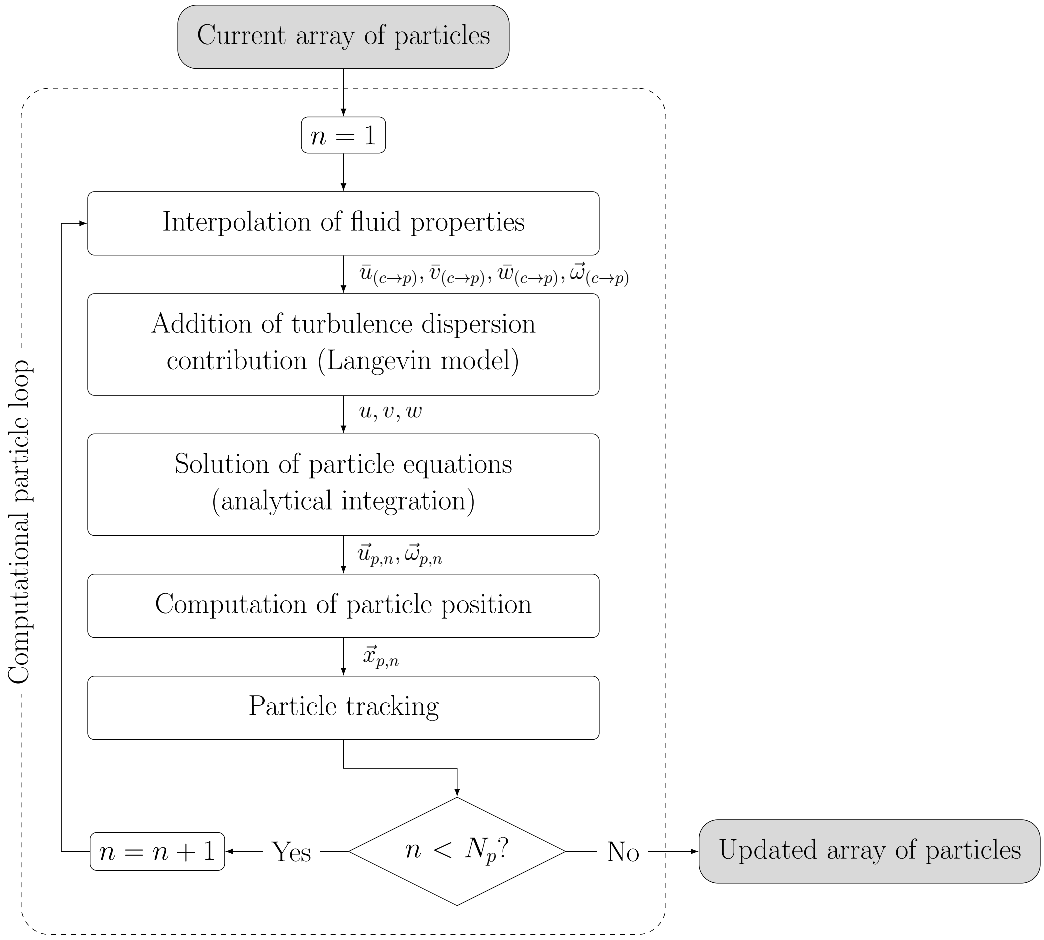

4.3 Results and discussion

In Section 3.4.2, optimized geometries were obtained while minimizing total pressure losses. The objective now is to assess whether these geometries can offer improvements in terms of erosion mitigation compared to their respective baseline geometries.

Regarding the models involved in the simulation of erosive wear, the results provided by the UNSCYFL3D code have already been validated in previous works (DUARTE; SOUZA; SANTOS, 2015, 2016; DUARTE; SOUZA, 2017; DUARTE *et al.*, 2017) against experimental data (MAZUMDER; SHIRAZI; MCLAURY, 2008; SOLNORDAL; WONG; BOULANGER, 2015). Accordingly, a particle-laden flow is simulated in the baseline and optimized geometries to analyze the erosion effects due to solid particle impacts on the pipe bend walls. Three Stokes numbers are investigated to evaluate different correlations between fluid and particle flows.

Sand particles are fed into the vertical pipe through the inlet face. The pipe walls are considered perfectly smooth, and the static and dynamic friction coefficients for the particle-wall collision model are assumed to be equal to 0.25. Such assumptions are justified by their good agreement with experimental results (MAZUMDER; SHIRAZI; MCLAURY, 2008), as presented by Duarte, Souza, and Santos (2016). Similar conditions to those of the above-mentioned experiment were considered in this investigation. Table 4.1 summarizes only the particle and the pipe properties, since the fluid properties were previously shown in Tab. 3.1.

Particle flow simulations are unsteady and executed for one million time steps of 2×10^{-5} s. A total of 300 computational particles are injected through the inlet every 10 time steps. Thus, about 30 million computational particles are simulated to obtain statistically converging results.

For all bend configurations (45°, 90° and 180°), the baseline design is first simulated three times, each one for a different Stokes number. Then, the geometry is switched to the optimized design, and the same procedures are repeated. After investigating the erosion behavior for each configuration, the optimization gains are analyzed. In this context, the decrease in penetration ratio from baseline to optimized geometry is calculated, as is the reduction in mass loss of aluminum caused by erosion.

Table 4.1 – Particle and pipe properties for erosion investigation.

Particle properties	
Material	Sand
Density (kg/m^3)	2 600
Mass flow rate (kg/s)	2.75×10^{-4}
Diameter (µm)	30, 96, 182
Stokes number	9.75, 99.84, 358.85

Pipe properties	
Material	Aluminum
Density (kg/m^3)	2 700
Vickers hardness (GPa)	1.049

4.3.1 Designs' effects on erosion

For a better comprehension of the erosion patterns, the analysis of this part of the results is limited to the penetration ratio profile and other erosion-related parameters. The optimization improvements are discussed in more detail in Section 4.3.2.

The results of penetration ratio for both baseline and optimized designs are shown in Fig. 4.3 for the simulations of the 45° bend, in Fig. 4.4 for the simulations of the 90° bend, and in Fig. 4.5 for the simulations of the 180° bend. In order to easily compare, the

Figure 4.3 – Contours of penetration ratio for the baseline geometry (left) and optimized geometry (right) of the 45° bend.

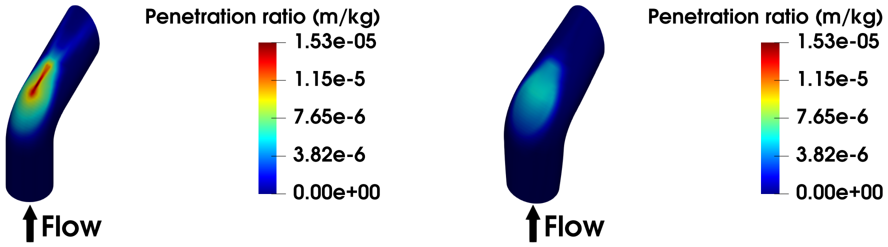

(a) $St = 9.75$.

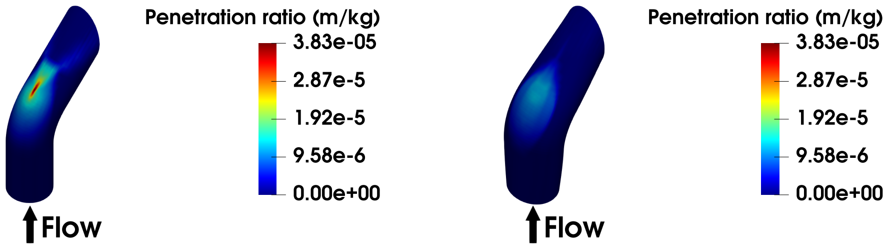

(b) $St = 99.84$.

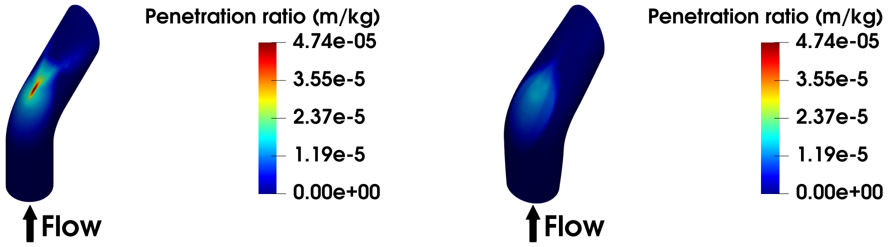

(c) $St = 358.85$.

results are presented on the same scale for the same Stokes number. Evidently, the contour patterns are quite different between the two designs. Observing the baseline design in all cases, the penetration ratio has a contour with a well-defined maximum erosion spot. Meanwhile, for the optimized design, the contours can hardly be seen, demonstrating that the penetration ratio values are lower than those of the baseline designs.

Figure 4.4 – Contours of penetration ratio for the baseline geometry (left) and optimized geometry (right) of the 90° bend.

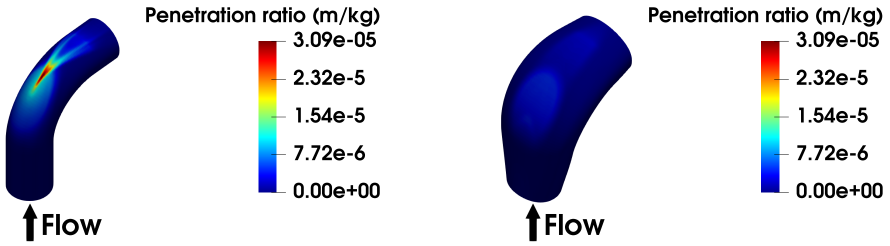

(a) $St = 9.75$.

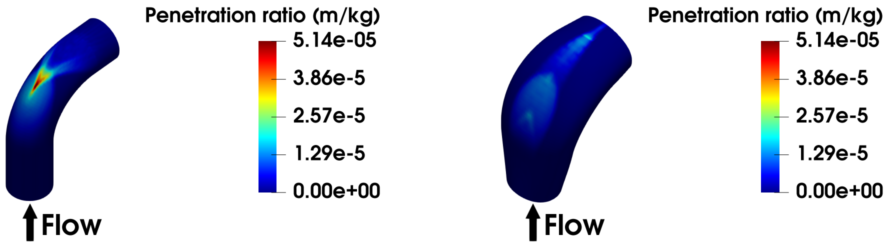

(b) $St = 99.84$.

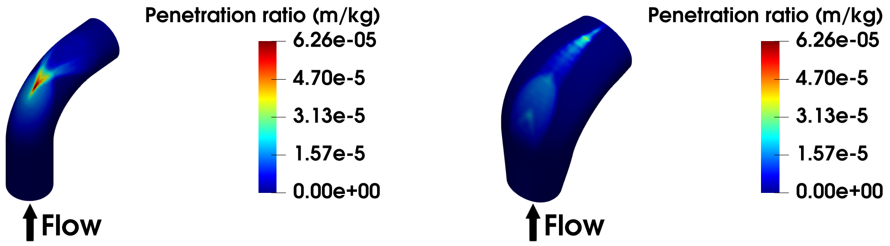

(c) $St = 358.85$.

Figure 4.5 – Contours of penetration ratio for the baseline (left) and optimized (right) geometries of the 180° bend.

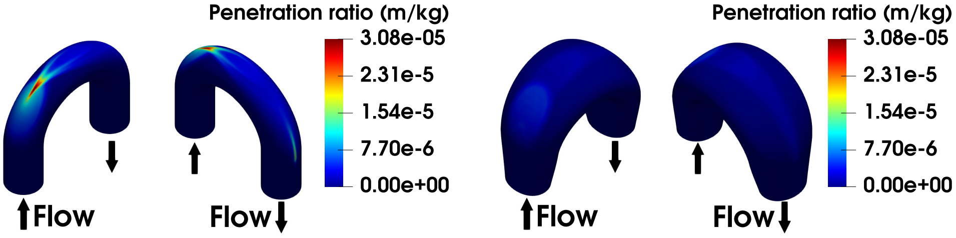

(a) $St = 9.75$.

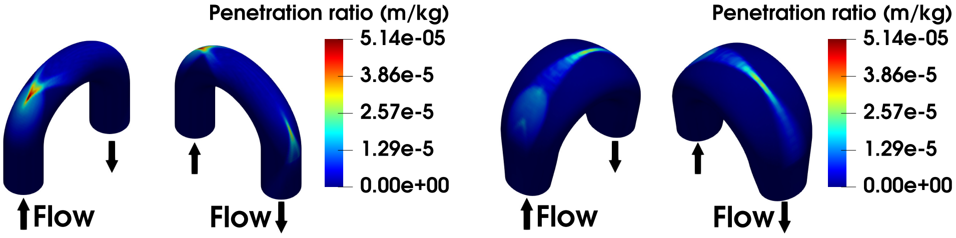

(b) $St = 99.84$.

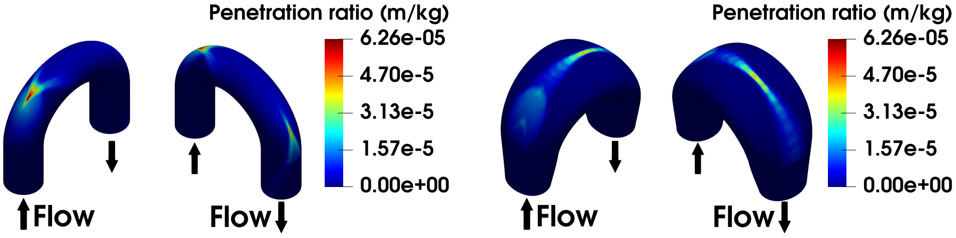

(c) $St = 358.85$.

Additional statistics for explaining the erosive wear due to particle-wall collisions are essential to evaluating the occurrence and behavior of the erosion. Hence, the particle impact angle, particle impact velocity, and particle impact frequency are averaged over time and used as parameters. The erosion profile is measured along the outer curvature surface as indicated in Fig. 4.6. The origin, or 0°, of the local coordinate system is placed at the bend inlet for the three considered cases, while 45° (Fig. 4.6a), 90° (Fig. 4.6b) and 180° (Fig. 4.6c) correspond, respectively, to the bend outlet of each pipeline component type.

Figure 4.6 – Schematic representation of the measurement region.

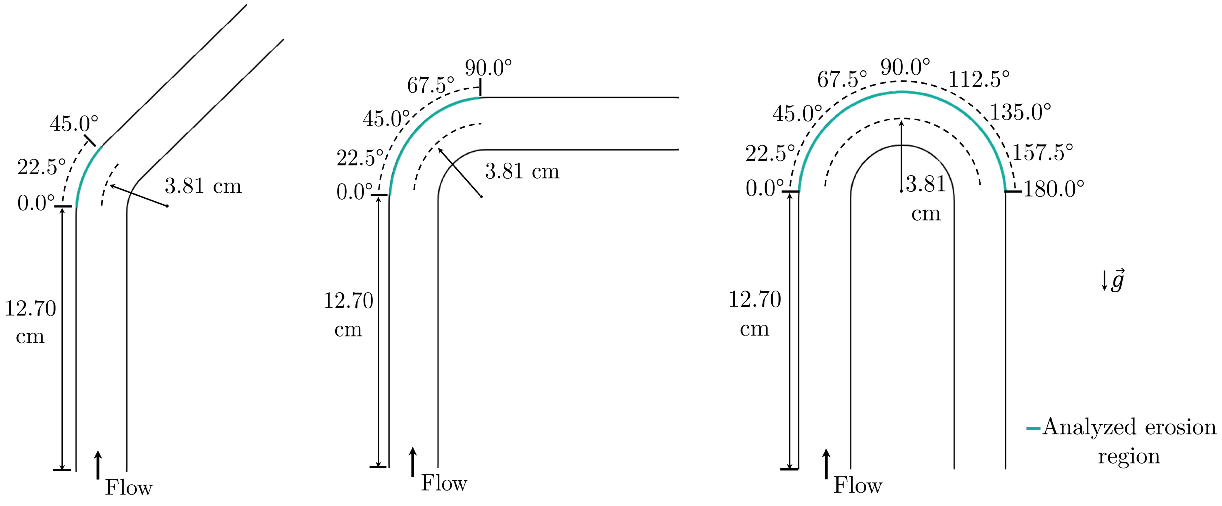

(a) 45° bend.
(b) 90° bend.
(c) 180° bend.

A quantitative comparison of the results for each erosion-related parameter is presented in Fig. 4.7. Since similar behavior can be observed in all bend cases, only the results for the 90° bends are displayed. The erosion-related parameters were extracted from the plane of symmetry of the baseline and optimized curvatures.

Considering the baseline geometry results, there is a clear penetration peak having a maximum value at a curvature angle close to 50° for all Stokes numbers (Figs. 4.7a–c). By contrast, the optimized geometry does not exhibit the same behavior. Comparing the values of penetration ratio at the curvature angles between 40° and 60°, the optimized geometry values are smaller than baseline values. This can be clarified by looking at the impact frequency profiles (Figs. 4.7j–l). For the same range of curvature angles, the values of impact frequency are also smaller for the optimized geometry. Consequently, the reduction in impact frequency certainly influenced the reduction in penetration values.

Another distinctive feature of the impact frequency for the optimized geometry is that it increases steadily from nearly 67.5° to 90°, reaching a peak at the latter. In particular, for the two larger Stokes numbers, their value is actually higher than that for

Figure 4.7 – Erosion-related parameters extracted from the plane of symmetry of the baseline and optimized 90° bends. From left to right: $St = 9.75$, $St = 99.84$, and $St = 358.85$.

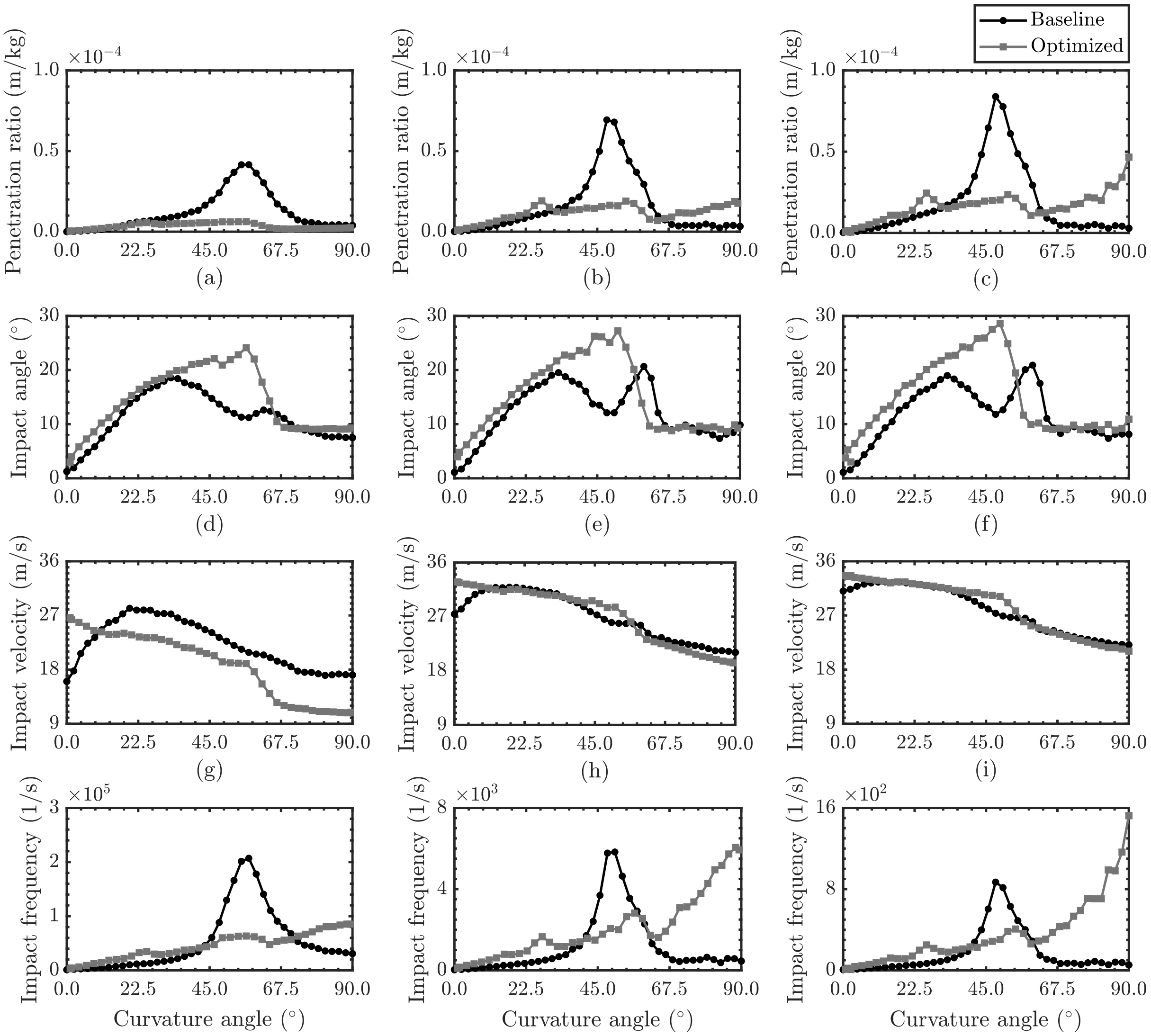

(a) (b) (c)

(d) (e) (f)

(g) (h) (i)

(j) (k) (l)

the baseline geometry. This behavior can be explained as follows: with the optimization, the flow in the region between 0° and 90° was smoothed according to its sensitivity gradient, such that the whole region is expanded, as visible from Fig. 3.20. This is somehow analogous to an increase in the curvature radius, which can be observed, for example, in the case of larger pipes. Thus, incoming particles from the straight pipe upstream of the bend now must travel a longer distance to hit the bend wall. Conversely, instead of colliding with the bend directly as in the baseline geometry, particles tend to move more tangentially in the optimized case. However, this effect is interrupted as the particles approach the end of the curve, since the geometry downstream is the same as in the baseline geometry. This in turn causes the peak of maximum impact frequency to be spatially delayed to 90°, resulting in a higher erosion rate at this angle. The increase in the impact frequency at that position is proportional to the Stokes number since more inertial particles will tend to move closer to the bend wall and will strike the downstream straight pipe at 90° more intensively than in the non-optimized geometry.

Nevertheless, one can also observe that the penetration value of the optimized geometry at 90° does not exceed the maximum penetration found in the baseline geometry. In this case, it is important to note the role that velocity plays in penetration ratio and how the optimized geometry took advantage of it (Figs. 4.7g–i). The impact velocity at 90° is smaller when compared to the impact velocity values at 40°–60° for any geometry and Stokes number. For a high impact frequency, as the corresponding impact velocity is low, the penetration ratio did not result in such a high value. Therefore, a low value of the impact frequency as well as a low value of the impact velocity contribute to reducing the penetration ratio.

The impact angle profiles are presented in Figs. 4.7d–f. In the profiles of the baseline geometry, two characteristic peaks are noticed. As already shown by Duarte *et al.* (2020), the particles tend to return to the core region of the elbow after their first impact. Then, the flow pushes them back against the wall, resulting in two regions with higher impact angles. In the case of the optimized geometry, just one peak is observed. Even though the impact angle for the optimized case is higher, the impact frequency remains low in this region, resulting in a low penetration ratio.

4.3.2 Stokes number effects on erosion reduction

The maximum penetration ratio and the total mass loss considering each Stokes number and shape design are provided in Tabs. 4.2 to 4.4, for the 45°, 90°, and 180° bends, respectively. The erosion reduction is evaluated by calculating the relative difference between the maximum penetration of the optimized design and the maximum penetration of the baseline design. Furthermore, the total mass loss is obtained by summing the entire aluminum mass lost from the pipe at all locations.

Regarding the 45° bend configuration (see Tab. 4.2), the erosion parameter reduced 62.46 %, 68.52 %, and 68.63 % for the Stokes numbers 9.75, 99.84, and 358.85, respectively. The amount of aluminum mass loss also decreased, and, following the same order, mass loss reductions of 44.82 %, 44.33 %, and 52.83 % were found.

Table 4.2 – Maximum penetration ratio and total mass loss caused by erosion for different Stokes numbers for the 45° bend.

Parameter	$\boldsymbol{St = 9.75}$		$\boldsymbol{St = 99.84}$		$\boldsymbol{St = 358.85}$	
	Baseline	**Optimized**	**Baseline**	**Optimized**	**Baseline**	**Optimized**
Max. p. ratio ($\times 10^{-5}$ m/kg)	1.5258	0.5728	3.8308	1.2058	4.7446	1.4882
Total mass loss ($\times 10^{-7}$ kg)	1.2488	0.6891	2.7998	1.5585	3.9703	1.8728

In the 90° bend case (see Tab. 4.3), the erosion reduction was 84.96 %, 61.94 %, and 45.09 %, from the smallest to the largest Stokes number. Additionally, the total mass loss was reduced by 52.53 %, 33.48 %, and 31.16 %, respectively.

Table 4.3 – Maximum penetration ratio and total mass loss caused by erosion for different Stokes numbers for the 90° bend.

Parameter	$\boldsymbol{St = 9.75}$		$\boldsymbol{St = 99.84}$		$\boldsymbol{St = 358.85}$	
	Baseline	**Optimized**	**Baseline**	**Optimized**	**Baseline**	**Optimized**
Max. p. ratio ($\times 10^{-5}$ m/kg)	3.0904	0.4648	5.1377	1.9552	6.2570	3.4357
Total mass loss ($\times 10^{-7}$ kg)	1.5264	0.7246	2.7059	1.8000	3.3379	2.2977

Lastly, in the 180° bend case (see Tab. 4.4), the maximum values of penetration ratio were reduced by 84.08 %, 44.11 %, and 32.10 %, following the ascending order of Stokes numbers. Moreover, the reductions in total mass loss were obtained approximately equal to the 90° bend case, being 52.97 %, 34.40 %, and 31.56 %, respectively.

Table 4.4 – Maximum penetration ratio and total mass loss caused by erosion for different Stokes numbers for the 180° bend.

Parameter	$\boldsymbol{St = 9.75}$		$\boldsymbol{St = 99.84}$		$\boldsymbol{St = 358.85}$	
	Baseline	**Optimized**	**Baseline**	**Optimized**	**Baseline**	**Optimized**
Max. p. ratio ($\times 10^{-5}$ m/kg)	3.0803	0.4903	5.1400	2.8729	6.2601	4.2505
Total mass loss ($\times 10^{-7}$ kg)	1.9892	0.9355	4.1010	2.6903	5.3320	3.6493

Consequently, in all cases, even considering flows with high-inertia particles, the erosive effect was reduced. It is noteworthy that for the 45° bend case, the reductions obtained were similar for all Stokes numbers, while in the 90°, and 180° bend cases, for the smallest Stokes number, the gains with the optimized geometry were more significant.

As a final remark, the flow dynamics provided by the optimized geometry are very promising in terms of mitigating the erosive process in pipeline components, regardless of particle size. Even reducing the total pressure losses by 14.51 %, 22.30 %, and 36.50 %, it was possible to reduce the erosion peak by up to 68.63 %, 84.96 %, and 84.08 %, respectively.

4.4 Conclusions

A comprehensive investigation of gas-particle flow was conducted, covering both the original designs and the optimized designs obtained in the previous chapter. The optimized geometries were evaluated and compared to their respective baseline geometries, with a specific focus on erosion wear. The erosive effect was then analyzed for three different Stokes numbers. Remarkably, the optimization process successfully contributed to a reduction in erosion despite the objective function being applied to a single-phase flow.

Significant improvements were observed for all pipe bend cases and Stokes numbers.

The maximum value of the penetration ratio, as well as the amount of material mass loss, decreased by over 30 %. These results can be better explained by the reduction in both the impact velocity and frequency of the particles against the bend walls.

The gains achieved through optimization exceeded expectations, especially when considering the percentage reduction in the objective function. The benefits derived from shape optimization are twofold: not only can total pressure losses be minimized, but the service life of equipment can also be maximized. As a result, the optimization process leads to shapes that can embody innovative designs.

It is important to point out that, until now, the shape optimization has not actually been carried out for the multiphase flow system. The reduction in erosion is merely a consequence of the reduction in total pressure losses in the fluid flow. In the forthcoming chapter, shape optimization involving aspects of the dispersed phase of multiphase flow will be addressed.

CHAPTER V

MULTIPHASE FLOW OPTIMIZATION PROBLEM

This chapter introduces a new proposal to tackle shape optimization problems in the context of multiphase flow systems. In order to overcome the associated challenges, the traditional choice of the Euler-Lagrange approach for modeling multiphase flows is no longer suitable, necessitating a shift towards the Euler-Euler approach.

A two-fluid model is adopted to capture the dynamics of the multiphase flow. In this approach, dispersed particles are treated as a continuous medium, and their behavior is described by partial differential equations. In line with the Euler-Euler approach, the shape optimization problem is formulated, and the corresponding continuous adjoint equations are derived.

The chosen case study to be investigated here corresponds to the deposition of dispersed particles in pipe bends. Understanding and predicting the transport and deposition of these particles is crucial in developing and optimizing various medical and industrial applications, such as drug delivery, blood flow, clean-coal gas turbines, and food processing. Notably, the ability to control the deposition efficiency is often desired in these scenarios.

5.1 Mathematical modeling

In the two-fluid Eulerian model, the particle-phase continuity and linear momentum equations are solved independently of the fluid phase equations, which are the same ones presented in Section 3.1.1. From the Eulerian particle equations and the respective boundary conditions, it is possible to estimate the efficiency of particle deposition on wall boundaries. Based on the Euler-Euler system of equations, new adjoint equations are developed for shape optimization and applied to the problem of particle deposition.

5.1.1 Eulerian particle equations

The Eulerian particle equations solved for the two-fluid model were obtained based on the assumptions of a laminar flow, a dilute phase (one-way coupling), a very high particle-to-fluid density ratio, and only weight and drag forces acting on individual particles (VASQUEZ; WALTERS; WALTERS, 2015). The resulting simplified equations in their steady-state form are:

$$\frac{\partial(\rho_p \Phi_p u_{p_j})}{\partial x_j} = 0, \tag{5.1}$$

$$\frac{\partial(\rho_p \Phi_p u_{p_j} u_{p_i})}{\partial x_j} = \rho_p \Phi_p g_i \left(1 - \frac{\rho}{\rho_p}\right) + \rho_p \Phi_p f_d (u_i - u_{p_i}), \tag{5.2}$$

where f_d is the same term as in Eq. (4.5), and the particle-phase volume fraction is within the range $0 < \Phi_p < 1$.

At the **inlet** boundaries Γ_{in}, a uniform particle concentration is set. Therefore, a Dirichlet condition is considered for the particle-phase volume fraction and velocity components:

$$\Phi_p = \Phi_{p,\text{in}} \quad \text{on} \quad \Gamma_{\text{in}}, \tag{5.3}$$

$$u_{p_n} = U_{p,\text{in}} \quad \text{on} \quad \Gamma_{\text{in}}, \tag{5.4}$$

$$u_{p_t} = u_{p_s} = 0 \quad \text{on} \quad \Gamma_{\text{in}}, \tag{5.5}$$

in which $\Phi_{p,\text{in}}$ is the volume fraction of particles at the inlet, and $U_{p,\text{in}}$ is the inlet velocity of particles in the domain.

Simple convection condition is applied at the **outlet** boundaries Γ_{out}. In this case, a Neumann condition is considered for the particle-phase volume fraction and velocity components:

$$\frac{\partial \Phi_p}{\partial n} = 0 \quad \text{on} \quad \Gamma_{\text{out}}, \tag{5.6}$$

$$\frac{\partial u_{p_i}}{\partial n} = 0 \quad \text{on} \quad \Gamma_{\text{out}}. \tag{5.7}$$

The treatment of the **wall** boundaries Γ_{wall} for particles is a critical component of the two-fluid model. The particle-wall interaction can be represented as a particle-phase convective flux out of the domain. In the current study, a simple approach is employed, assuming a zero Neumann boundary condition for the particle velocity components. In practice, this assumes that the velocity at the wall is equivalent to the velocity in the first near-wall computational cell:

$$\frac{\partial u_{p_i}}{\partial n} = 0 \quad \text{on} \quad \Gamma_{\text{wall}}. \tag{5.8}$$

For volume fraction estimation, it is necessary to know the direction of particle-phase impact velocity at the wall. Defining that:

$$\Gamma_{\text{wall}}^{-} = \left\{ x_i \in \Gamma_{\text{wall}} \mid u_{p_n}(x_i) \leq 0 \right\}, \tag{5.9}$$

and

$$\Gamma_{\text{wall}}^{+} = \Gamma_{\text{wall}} \setminus \Gamma_{\text{wall}}^{-}, \tag{5.10}$$

the boundary condition is:

$$\begin{cases} \Phi_p = 0 & \text{on} \quad \Gamma^-_{\text{wall}}, \\ \dfrac{\partial \Phi_p}{\partial n} = 0 & \text{on} \quad \Gamma^+_{\text{wall}}. \end{cases} \tag{5.11}$$

When the particle-phase velocity points outside the domain, the zero Neumann boundary condition is used, and the volume fraction at the wall is equal to the volume fraction in the first near-wall cell. However, when the particle-phase velocity does not point outside the domain, the volume fraction at the wall is assumed to be zero, which prevents the appearance of unphysical inflow. Vasquez, Walters, and Walters (2015) tested more advanced and complex wall boundary condition methods and found that, for the considered problem, they did not imply a significant change in the results. Since the studied cases involve flows with a dominant convective transport direction, the simplest model is useful, although it has limitations.

5.1.2 Deposition efficiency

Deposition efficiency is a measure of the fraction of particles that are deposited or collected onto a specific surface. This surface could be a filter, a collector, or a target area. In numerical terms, it typically corresponds to a wall boundary. The calculation of deposition efficiency involves dividing the mass of particles deposited in the wall by the total mass of particles that entered the region of interest:

$$\eta_{\text{dep}} = \frac{\dot{m}_{p,\text{dep}}}{\dot{m}_{p,\text{in}}} \quad \text{with} \quad \dot{m}_{p,\text{dep}} = \int_{\Gamma_{\text{wall}}} \rho_p \, \Phi_p \, u_{p_i} \, n_i \, \mathrm{d}\Gamma. \tag{5.12}$$

5.1.3 Continuous adjoint for multiphase flows

The shape optimization problem restricted by a laminar multiphase flow can be stated as:

$$\begin{aligned} &\text{minimize} && J(\beta, u_i, p, u_{p_i}, \Phi_p) \\ &\text{subject to} && \mathcal{R}(\beta, u_i, p, u_{p_i}, \Phi_p) = 0, \end{aligned} \tag{5.13}$$

where the state equations $\mathcal{R} = (R_i, Q, R_{p_i}, Q_p)^\intercal$ are the Navier-Stokes and continuity equations, Eqs. (3.12) and (3.3), in addition to the linear momentum equations of particles and the transport equation of volume fraction, Eqs. (5.2) and (5.1). For the mathematical development of the adjoint method, these equations were adopted in the non-divergence form. Once again, the fluid dynamics equations, Eqs. (3.27) and (3.28), are shown, but this time for a laminar regime, in which the primal equations also involve the particle equations:

$$R_i = \rho u_j \frac{\partial u_i}{\partial x_j} + \frac{\partial p}{\partial x_i} - \frac{\partial}{\partial x_j}\left[\mu\left(\frac{\partial u_i}{\partial x_j} + \frac{\partial u_j}{\partial x_i}\right)\right] = 0, \tag{5.14}$$

$$Q = -\frac{\partial u_i}{\partial x_i} = 0, \tag{5.15}$$

$$R_{p_i} = \rho_p u_{p_j} \frac{\partial u_{p_i}}{\partial x_j} + \rho_p f_d u_{p_i} - \rho_p g_i \left(1 - \frac{\rho}{\rho_p}\right) - \rho_p f_d u_i = 0, \tag{5.16}$$

$$Q_p = -\frac{\partial (\Phi_p u_{p_j})}{\partial x_j} = 0. \tag{5.17}$$

Thus, the Lagrange function is formulated as:

$$L = J + \int_\Omega \left(\hat{u}_i R_i + \hat{p} Q + \hat{u}_{p_i} R_{p_i} + \hat{\Phi}_p Q_p\right) \, \mathrm{d}\Omega, \tag{5.18}$$

and its variation according to Eq. (2.15) is:

$$\begin{aligned} \delta L = & \int_{\Gamma_\mathrm{O} \cap \Gamma_\mathrm{D}} \delta_\beta J_\Gamma \, \mathrm{d}\Gamma + \int_{\Gamma_\mathrm{O}} \left(\delta_{u_i} J_\Gamma + \delta_p J_\Gamma + \delta_{u_{p_i}} J_\Gamma + \delta_{\Phi_p} J_\Gamma\right) \, \mathrm{d}\Gamma \\ & + \int_{\Omega_\mathrm{O}} \left(\delta_{u_i} J_\Omega + \delta_p J_\Omega + \delta_{u_{p_i}} J_\Omega + \delta_{\Phi_p} J_\Omega\right) \, \mathrm{d}\Omega \\ & + \int_\Omega \left(\hat{u}_i \delta R_i + \hat{p} \delta Q + \hat{u}_{p_i} \delta R_{p_i} + \hat{\Phi}_p \delta Q_p\right) \, \mathrm{d}\Omega, \end{aligned} \tag{5.19}$$

in which the adjoint variables are the adjoint velocity $\hat{u}_i$ and the adjoint pressure $\hat{p}$ of the fluid, and the adjoint velocity $\hat{u}_{p_i}$ and the adjoint volume fraction $\hat{\Phi}_p$ of particles.

The variations of the primal equations with respect to the state variables can be obtained as:

$$\delta R_i = \rho(\delta u_j)\frac{\partial u_i}{\partial x_j} + \rho u_j \frac{\partial(\delta u_i)}{\partial x_j} + \frac{\partial(\delta p)}{\partial x_i} - \frac{\partial}{\partial x_j}\left[\mu\left(\frac{\partial(\delta u_i)}{\partial x_j} + \frac{\partial(\delta u_j)}{\partial x_i}\right)\right], \tag{5.20}$$

$$\delta Q = -\frac{\partial(\delta u_i)}{\partial x_i}, \tag{5.21}$$

$$\delta R_{p_i} = \rho_p(\delta u_{p_j})\frac{\partial u_{p_i}}{\partial x_j} + \rho_p u_{p_j}\frac{\partial(\delta u_{p_i})}{\partial x_j} + \rho_p f_d(\delta u_{p_i}) - \rho_p f_d(\delta u_i), \tag{5.22}$$

$$\delta Q_p = -\Phi_p \frac{\partial(\delta u_{p_j})}{\partial x_j} - \delta u_{p_j}\frac{\partial \Phi_p}{\partial x_j} - \delta\Phi_p \frac{\partial u_{p_j}}{\partial x_j} - u_{p_j}\frac{\partial(\delta\Phi_p)}{\partial x_j}. \tag{5.23}$$

Thereby, Eq. (5.19) is rewritten as:

$$\begin{aligned}
\delta L = & \int_{\Gamma_\mathrm{O}\cap\Gamma_\mathrm{D}} \delta_\beta J_\Gamma \,\mathrm{d}\Gamma + \int_{\Gamma_\mathrm{O}} \left(\delta_{u_i} J_\Gamma + \delta_p J_\Gamma + \delta_{u_{p_i}} J_\Gamma + \delta_{\Phi_p} J_\Gamma\right) \mathrm{d}\Gamma \\
& + \int_{\Omega_\mathrm{O}} \left(\delta_{u_i} J_\Omega + \delta_p J_\Omega + \delta_{u_{p_i}} J_\Omega + \delta_{\Phi_p} J_\Omega\right) \mathrm{d}\Omega \\
& + \int_\Omega \hat{u}_i \rho(\delta u_j)\frac{\partial u_i}{\partial x_j}\,\mathrm{d}\Omega \underbrace{+ \int_\Omega \hat{u}_i \rho u_j \frac{\partial(\delta u_i)}{\partial x_j}\,\mathrm{d}\Omega}_{\text{(t.1)}} \underbrace{+ \int_\Omega \hat{u}_i \frac{\partial(\delta p)}{\partial x_i}\,\mathrm{d}\Omega}_{\text{(t.2)}} \\
& \underbrace{- \int_\Omega \hat{u}_i \frac{\partial}{\partial x_j}\left[\mu\left(\frac{\partial(\delta u_i)}{\partial x_j} + \frac{\partial(\delta u_j)}{\partial x_i}\right)\right] \mathrm{d}\Omega}_{\text{(t.3)}} \underbrace{- \int_\Omega \hat{p}\frac{\partial(\delta u_i)}{\partial x_i}\,\mathrm{d}\Omega}_{\text{(t.4)}} \\
& + \int_\Omega \hat{u}_{p_i}\left[\rho_p(\delta u_{p_j})\frac{\partial u_{p_i}}{\partial x_j} + \rho_p f_d(\delta u_{p_i}) - \rho_p f_d(\delta u_i)\right] \mathrm{d}\Omega \\
& \underbrace{+ \int_\Omega \hat{u}_{p_i}\rho_p u_{p_j}\frac{\partial(\delta u_{p_i})}{\partial x_j}\,\mathrm{d}\Omega}_{\text{(t.7)}} - \int_\Omega \hat{\Phi}_p\left[\delta u_{p_j}\frac{\partial \Phi_p}{\partial x_j} + \delta\Phi_p\frac{\partial u_{p_j}}{\partial x_j}\right] \mathrm{d}\Omega \\
& \underbrace{- \int_\Omega \hat{\Phi}_p \Phi_p \frac{\partial(\delta u_{p_j})}{\partial x_j}\,\mathrm{d}\Omega}_{\text{(t.8)}} \underbrace{- \int_\Omega \hat{\Phi}_p u_{p_j}\frac{\partial(\delta\Phi_p)}{\partial x_j}\,\mathrm{d}\Omega}_{\text{(t.9)}}
\end{aligned} \tag{5.24}$$

The terms (t.1) to (t.4) of the above equation have already been derived by applying the integration by parts in Section 3.1.3. Similarly, the terms (t.7) to (t.9) are determined:

$$
\begin{aligned}
(\text{t.7}) :\ & \int_{\Omega} \hat{u}_{p_i} \rho_p u_{p_j} \frac{\partial(\delta u_{p_i})}{\partial x_j}\, \mathrm{d}\Omega \\
&= \int_{\Gamma} \hat{u}_{p_i} \rho_p u_{p_j} n_j (\delta u_{p_i})\, \mathrm{d}\Gamma - \int_{\Omega} \frac{\partial(\rho_p u_{p_j} \hat{u}_{p_i})}{\partial x_j} (\delta u_{p_i})\, \mathrm{d}\Omega
\end{aligned}
\tag{5.25}
$$

$$
\begin{aligned}
(\text{t.8}) :\ & -\int_{\Omega} \hat{\Phi}_p \Phi_p \frac{\partial(\delta u_{p_j})}{\partial x_j}\, \mathrm{d}\Omega = -\int_{\Gamma} \hat{\Phi}_p \Phi_p n_i (\delta u_{p_i})\, \mathrm{d}\Gamma + \int_{\Omega} \frac{\partial(\hat{\Phi}_p \Phi_p)}{\partial x_i} (\delta u_{p_i})\, \mathrm{d}\Omega \\
&= -\int_{\Gamma} \hat{\Phi}_p \Phi_p n_i (\delta u_{p_i})\, \mathrm{d}\Gamma + \int_{\Omega} \hat{\Phi}_p \frac{\partial \Phi_p}{\partial x_i} (\delta u_{p_i})\, \mathrm{d}\Omega + \int_{\Omega} \Phi_p \frac{\partial \hat{\Phi}_p}{\partial x_i} (\delta u_{p_i})\, \mathrm{d}\Omega
\end{aligned}
\tag{5.26}
$$

$$
\begin{aligned}
(\text{t.9}) :\ & -\int_{\Omega} \hat{\Phi}_p u_{p_j} \frac{\partial(\delta \Phi_p)}{\partial x_j}\, \mathrm{d}\Omega = -\int_{\Gamma} \hat{\Phi}_p u_{p_i} n_i (\delta \Phi_p)\, \mathrm{d}\Gamma + \int_{\Omega} \frac{\partial(\hat{\Phi}_p u_{p_i})}{\partial x_i} (\delta \Phi_p)\, \mathrm{d}\Omega \\
&= -\int_{\Gamma} \hat{\Phi}_p u_{p_i} n_i (\delta \Phi_p)\, \mathrm{d}\Gamma + \int_{\Omega} \hat{\Phi}_p \frac{\partial u_{p_i}}{\partial x_i} (\delta \Phi_p)\, \mathrm{d}\Omega + \int_{\Omega} u_{p_i} \frac{\partial \hat{\Phi}_p}{\partial x_i} (\delta \Phi_p)\, \mathrm{d}\Omega
\end{aligned}
\tag{5.27}
$$

Replacing all the terms in Eq. (5.24) and rearranging them, it can be found that:

$$
\begin{aligned}
\delta L = & \int_{\Gamma_{\mathrm{O}} \cap \Gamma_{\mathrm{D}}} \delta_{\beta} J_{\Gamma}\, \mathrm{d}\Gamma + \int_{\Gamma_{\mathrm{O}}} \left(\delta_{u_i} J_{\Gamma} + \delta_p J_{\Gamma} + \delta_{u_{p_i}} J_{\Gamma} + \delta_{\Phi_p} J_{\Gamma} \right)\, \mathrm{d}\Gamma \\
& + \int_{\Omega_{\mathrm{O}}} \left(\delta_{u_i} J_{\Omega} + \delta_p J_{\Omega} + \delta_{u_{p_i}} J_{\Omega} + \delta_{\Phi_p} J_{\Omega} \right)\, \mathrm{d}\Omega \\
& + \int_{\Omega} \hat{u}_i \rho (\delta u_j) \frac{\partial u_i}{\partial x_j}\, \mathrm{d}\Omega + \int_{\Gamma} \rho u_j n_j \hat{u}_i \, (\delta u_i)\, \mathrm{d}\Gamma - \int_{\Omega} \frac{\partial(\rho u_j \hat{u}_i)}{\partial x_j} \, (\delta u_i)\, \mathrm{d}\Omega \\
& + \int_{\Gamma} \delta p \, (\hat{u}_i n_i)\, \mathrm{d}\Gamma - \int_{\Omega} \delta p \left(\frac{\partial \hat{u}_i}{\partial x_i} \right) \mathrm{d}\Omega - \int_{\Gamma} \hat{p} \, (\delta u_i n_i)\, \mathrm{d}\Gamma + \int_{\Omega} \delta u_i \frac{\partial \hat{p}}{\partial x_i}\, \mathrm{d}\Omega \\
& - \int_{\Gamma} \hat{u}_i \left[\mu \left(\frac{\partial(\delta u_i)}{\partial x_j} + \frac{\partial(\delta u_j)}{\partial x_i} \right) \right] n_j\, \mathrm{d}\Gamma \\
& + \int_{\Gamma} \delta u_i \left[\mu \left(\frac{\partial \hat{u}_i}{\partial x_j} + \frac{\partial \hat{u}_j}{\partial x_i} \right) \right] n_j\, \mathrm{d}\Gamma - \int_{\Omega} \delta u_i \frac{\partial}{\partial x_j} \left[\mu \left(\frac{\partial \hat{u}_i}{\partial x_j} + \frac{\partial \hat{u}_j}{\partial x_i} \right) \right] \mathrm{d}\Omega \\
& + \int_{\Omega} \hat{u}_{p_i} \left[\rho_p (\delta u_{p_j}) \frac{\partial u_{p_i}}{\partial x_j} + \rho_p f_d (\delta u_{p_i}) - \rho_p f_d (\delta u_i) \right] \mathrm{d}\Omega \\
& \int_{\Gamma} \hat{u}_{p_i} \rho_p u_{p_j} n_j (\delta u_{p_i})\, \mathrm{d}\Gamma - \int_{\Omega} \frac{\partial(\rho_p u_{p_j} \hat{u}_{p_i})}{\partial x_j} (\delta u_{p_i})\, \mathrm{d}\Omega - \int_{\Gamma} \hat{\Phi}_p \Phi_p n_i (\delta u_{p_i})\, \mathrm{d}\Gamma \\
& + \int_{\Omega} \Phi_p \frac{\partial \hat{\Phi}_p}{\partial x_i} (\delta u_{p_i})\, \mathrm{d}\Omega - \int_{\Gamma} \hat{\Phi}_p u_{p_i} n_i (\delta \Phi_p)\, \mathrm{d}\Gamma + \int_{\Omega} u_{p_i} \frac{\partial \hat{\Phi}_p}{\partial x_i} (\delta \Phi_p)\, \mathrm{d}\Omega
\end{aligned}
\tag{5.28}
$$

Then, applying the variation of the objective function in relation to the state variables, as shown in Eqs. (3.41) and (3.42), the above equation becomes:

$$
\begin{aligned}
\delta L = {} & \int_{\Gamma_{\mathrm{O}} \cap \Gamma_{\mathrm{D}}} \delta_\beta J_\Gamma \, \mathrm{d}\Gamma - \int_\Gamma \hat{u}_i \left[\mu \left(\frac{\partial(\delta u_i)}{\partial n} + \frac{\partial(\delta u_n)}{\partial x_i} \right) \right] \mathrm{d}\Gamma \\
& + \int_\Gamma \delta u_i \left[\rho u_n \hat{u}_i + \mu \left(\frac{\partial \hat{u}_i}{\partial n} + \frac{\partial \hat{u}_n}{\partial x_i} \right) - \hat{p} n_i \right] \mathrm{d}\Gamma + \int_{\Gamma_{\mathrm{O}}} \delta u_i \left(\frac{\partial J_\Gamma}{\partial u_i} \right) \mathrm{d}\Gamma \\
& + \int_\Gamma \delta p \, (\hat{u}_n) \, \mathrm{d}\Gamma + \int_{\Gamma_{\mathrm{O}}} \delta p \left(\frac{\partial J_\Gamma}{\partial p} \right) \mathrm{d}\Gamma + \int_\Gamma \delta u_{p_i} \left(\rho_p \hat{u}_{p_i} u_{p_n} - \hat{\Phi}_p \Phi_p n_i \right) \mathrm{d}\Gamma \\
& + \int_{\Gamma_{\mathrm{O}}} \delta u_{p_i} \left(\frac{\partial J_\Gamma}{\partial u_{p_i}} \right) \mathrm{d}\Gamma - \int_\Gamma \delta \Phi_p \left(\hat{\Phi}_p u_{p_n} \right) \mathrm{d}\Gamma + \int_{\Gamma_{\mathrm{O}}} \delta \Phi_p \left(\frac{\partial J_\Gamma}{\partial \Phi_p} \right) \mathrm{d}\Gamma \\
& + \int_\Omega \delta u_i \left\{ - \frac{\partial(\rho u_j \hat{u}_i)}{\partial x_j} + \frac{\partial \hat{p}}{\partial x_i} - \frac{\partial}{\partial x_j} \left[\mu \left(\frac{\partial \hat{u}_i}{\partial x_j} + \frac{\partial \hat{u}_j}{\partial x_i} \right) \right] + \rho \hat{u}_j \frac{\partial u_j}{\partial x_i} \right\} \mathrm{d}\Omega \\
& - \int_\Omega \delta u_i \left(\rho_p f_d \hat{u}_{p_i} \right) \mathrm{d}\Omega + \int_{\Omega_{\mathrm{O}}} \delta u_i \left(\frac{\partial J_\Omega}{\partial u_i} \right) \mathrm{d}\Omega \\
& - \int_\Omega \delta p \left(\frac{\partial \hat{u}_i}{\partial x_i} \right) \mathrm{d}\Omega + \int_{\Omega_{\mathrm{O}}} \delta p \left(\frac{\partial J_\Omega}{\partial p} \right) \mathrm{d}\Omega \\
& + \int_\Omega \delta u_{p_i} \left[- \frac{\partial(\rho_p u_{p_j} \hat{u}_{p_i})}{\partial x_j} + \rho_p \hat{u}_{p_i} \frac{\partial u_{p_j}}{\partial x_i} + \rho_p f_d \hat{u}_{p_i} + \Phi_p \frac{\partial \hat{\Phi}_p}{\partial x_i} \right] \mathrm{d}\Omega \\
& + \int_{\Omega_{\mathrm{O}}} \delta u_{p_i} \left(\frac{\partial J_\Omega}{\partial u_{p_i}} \right) \mathrm{d}\Omega + \int_\Omega \delta \Phi_p \left(u_{p_i} \frac{\partial \hat{\Phi}_p}{\partial x_i} \right) \mathrm{d}\Omega + \int_{\Omega_{\mathrm{O}}} \delta \Phi_p \left(\frac{\partial J_\Omega}{\partial \Phi_p} \right) \mathrm{d}\Omega.
\end{aligned}
\tag{5.29}
$$

As already mentioned, vanishing the integrals over the domain of Eq. (5.29) individually yields the adjoint equations. Therefore, the adjoint equations for steady-state, incompressible fluid flows carrying particles are:

$$
\begin{cases}
\dfrac{\partial \hat{u}_i}{\partial x_i} = \dfrac{\partial J_\Omega}{\partial p} & \text{in} \quad \Omega_O, \\[2ex]
\dfrac{\partial \hat{u}_i}{\partial x_i} = 0 & \text{in} \quad \Omega \setminus \Omega_O,
\end{cases}
\tag{5.30}
$$

$$
\begin{cases}
\begin{aligned}
- \frac{\partial (\rho u_j \hat{u}_i)}{\partial x_j} = {} & - \frac{\partial \hat{p}}{\partial x_i} + \frac{\partial}{\partial x_j} \left[\mu \left(\frac{\partial \hat{u}_i}{\partial x_j} + \frac{\partial \hat{u}_j}{\partial x_i} \right) \right] - \rho \hat{u}_j \frac{\partial u_j}{\partial x_i} \\
& + \rho_p f_d \hat{u}_{p_i} - \frac{\partial J_\Omega}{\partial u_i}
\end{aligned} & \text{in} \quad \Omega_O, \\[4ex]
\begin{aligned}
- \frac{\partial (\rho u_j \hat{u}_i)}{\partial x_j} = {} & - \frac{\partial \hat{p}}{\partial x_i} + \frac{\partial}{\partial x_j} \left[\mu \left(\frac{\partial \hat{u}_i}{\partial x_j} + \frac{\partial \hat{u}_j}{\partial x_i} \right) \right] - \rho \hat{u}_j \frac{\partial u_j}{\partial x_i} \\
& + \rho_p f_d \hat{u}_{p_i}
\end{aligned} & \text{in} \quad \Omega \setminus \Omega_O,
\end{cases}
\tag{5.31}
$$

$$\begin{cases} -u_{p_j}\dfrac{\partial \hat{\Phi}_p}{\partial x_j} = \dfrac{\partial J_\Omega}{\partial \Phi_p} & \text{in} \quad \Omega_O, \\[2ex] -u_{p_j}\dfrac{\partial \hat{\Phi}_p}{\partial x_j} = -\dfrac{\partial(\rho_p \Phi_p u_{p_j} \hat{\Phi}_p)}{\partial x_j} = 0 & \text{in} \quad \Omega \setminus \Omega_O, \end{cases} \tag{5.32}$$

$$\begin{cases} -\dfrac{\partial(\rho_p u_{p_j} \hat{u}_{p_i})}{\partial x_j} = -\rho_p f_d \hat{u}_{p_i} - \rho_p \hat{u}_{p_j}\dfrac{\partial u_{p_j}}{\partial x_i} - \Phi_p \dfrac{\partial \hat{\Phi}_p}{\partial x_i} - \dfrac{\partial J_\Omega}{\partial u_{p_i}} & \text{in} \quad \Omega_O, \\[2ex] -\dfrac{\partial(\rho_p u_{p_j} \hat{u}_{p_i})}{\partial x_j} = -\rho_p f_d \hat{u}_{p_i} - \rho_p \hat{u}_{p_j}\dfrac{\partial u_{p_j}}{\partial x_i} - \Phi_p \dfrac{\partial \hat{\Phi}_p}{\partial x_i} & \text{in} \quad \Omega \setminus \Omega_O. \end{cases} \tag{5.33}$$

For the one-way coupling problem, it is clear in the primal field that the particle transport is influenced by the fluid motion, but the opposite does not happen. Nevertheless, in the corresponding adjoint field, particles have an influence on the fluid motion. The adjoint momentum equations of the fluid, Eq. (5.31), depend on the adjoint velocity of the particles.

For any $(\hat{u}_i, \hat{p}, \hat{u}_{p_i}, \hat{\Phi}_p)$ that satisfies the adjoint equations, the variation of the Lagrange function can be simplified to:

$$\begin{aligned} \delta L = {} & \int_{\Gamma_\mathrm{O} \cap \Gamma_\mathrm{D}} \delta_\beta J_\Gamma \, \mathrm{d}\Gamma - \int_\Gamma \hat{u}_i \left[\mu\left(\frac{\partial(\delta u_i)}{\partial n} + \frac{\partial(\delta u_n)}{\partial x_i}\right)\right] \mathrm{d}\Gamma \\ & + \int_\Gamma \delta u_i \left[\rho u_n \hat{u}_i + \mu\left(\frac{\partial \hat{u}_i}{\partial n} + \frac{\partial \hat{u}_n}{\partial x_i}\right) - \hat{p} n_i\right] \mathrm{d}\Gamma + \int_{\Gamma_\mathrm{O}} \delta u_i \left(\frac{\partial J_\Gamma}{\partial u_i}\right) \mathrm{d}\Gamma \\ & + \int_\Gamma \delta p \left(\hat{u}_n\right) \mathrm{d}\Gamma + \int_{\Gamma_\mathrm{O}} \delta p \left(\frac{\partial J_\Gamma}{\partial p}\right) \mathrm{d}\Gamma + \int_\Gamma \delta u_{p_i} \left(\rho_p \hat{u}_{p_i} u_{p_n} - \hat{\Phi}_p \Phi_p n_i\right) \mathrm{d}\Gamma \\ & + \int_{\Gamma_\mathrm{O}} \delta u_{p_i} \left(\frac{\partial J_\Gamma}{\partial u_{p_i}}\right) \mathrm{d}\Gamma - \int_\Gamma \delta \Phi_p \left(\hat{\Phi}_p u_{p_n}\right) \mathrm{d}\Gamma + \int_{\Gamma_\mathrm{O}} \delta \Phi_p \left(\frac{\partial J_\Gamma}{\partial \Phi_p}\right) \mathrm{d}\Gamma. \end{aligned} \tag{5.34}$$

5.1.3.1 Boundary conditions

Boundaries that coincide with the design surface are disregarded here and will be addressed later. The adjoint boundary conditions are obtained by vanishing the surface integrals of Eq. (5.34):

$$\begin{aligned} & \int_\Gamma \delta u_i \left\{\rho u_n \hat{u}_i + \left[\mu\left(\frac{\partial \hat{u}_i}{\partial n} + \frac{\partial \hat{u}_n}{\partial x_i}\right)\right] - \hat{p} n_i\right\} \mathrm{d}\Gamma + \int_{\Gamma_\mathrm{O}} \delta u_i \left(\frac{\partial J_\Gamma}{\partial u_i}\right) \mathrm{d}\Gamma \\ & - \int_\Gamma \hat{u}_i \left[\mu\left(\frac{\partial(\delta u_i)}{\partial n} + \frac{\partial(\delta u_n)}{\partial x_i}\right)\right] \mathrm{d}\Gamma = 0, \end{aligned} \tag{5.35}$$

$$\int_{\Gamma} \delta p \left(\hat{u}_n\right) \, \mathrm{d}\Gamma + \int_{\Gamma_\mathrm{O}} \delta p \left(\frac{\partial J_\Gamma}{\partial p}\right) \, \mathrm{d}\Gamma = 0, \tag{5.36}$$

$$-\int_{\Gamma} \delta \Phi_p \left(u_{p_n} \hat{\Phi}_p\right) \, \mathrm{d}\Gamma + \int_{\Gamma_\mathrm{O}} \delta \Phi_p \left(\frac{\partial J_\Gamma}{\partial \Phi_p}\right) \, \mathrm{d}\Gamma = 0, \tag{5.37}$$

$$\int_{\Gamma} \delta u_{p_i} \left(\rho_p u_{p_n} \hat{u}_{p_i} - \Phi_p \hat{\Phi}_p n_i\right) \, \mathrm{d}\Gamma + \int_{\Gamma_\mathrm{O}} \delta u_{p_i} \left(\frac{\partial J_\Gamma}{\partial u_{p_i}}\right) \, \mathrm{d}\Gamma = 0. \tag{5.38}$$

Equations (5.35) and (5.36) leads to the same boundary conditions for the adjoint velocity and adjoint pressure of the fluid determined in Section 3.1.3.1. Hence, this section focuses solely on presenting the boundary conditions related to the adjoint variables of the particles.

By definition, the local variation of particle velocity and volume fraction on **inlet** boundaries is zero, $\delta u_{p_i} = 0$, and $\delta \Phi_p = 0$. As nothing can be concluded from Eqs. (5.37) and (5.38), it is assumed that:

$$\frac{\partial \hat{\Phi}_p}{\partial n} = 0 \quad \text{on} \quad \Gamma_\mathrm{in}, \tag{5.39}$$

$$\frac{\partial \hat{u}_{p_i}}{\partial n} = 0 \quad \text{on} \quad \Gamma_\mathrm{in}. \tag{5.40}$$

At the **outlet** boundaries, it can be inferred from the primal boundary conditions that $\delta \Phi_p \neq 0$ and $\delta u_{p_i} \neq 0$. Therefore, for an arbitrary value of $\delta \Phi_p$, it is found from Eq. (5.37) that:

$$-u_{p_n} \hat{\Phi}_p + \frac{\partial J_\Gamma}{\partial \Phi_p} = 0, \tag{5.41}$$

which means:

$$\hat{\Phi}_p = \begin{cases} \dfrac{1}{u_{p_n}} \dfrac{\partial J_\Gamma}{\partial \Phi_p} & \text{on} \quad \Gamma_\mathrm{out} \cap \Gamma_\mathrm{O}, \\[2ex] 0 & \text{on} \quad \Gamma_\mathrm{out} \setminus \Gamma_\mathrm{O}. \end{cases} \tag{5.42}$$

For an arbitrary value of δu_{p_i}, it is implied based on Eq. (5.38) that:

$$\rho_p u_{p_n} \hat{u}_{p_i} - \Phi_p \hat{\Phi}_p n_i + \frac{\partial J_\Gamma}{\partial u_{p_i}} = 0, \tag{5.43}$$

consequently:

$$\hat{u}_{p_i} = \begin{cases} \dfrac{1}{\rho_p u_{p_n}} \left(\Phi_p \hat{\Phi}_p n_i - \dfrac{\partial J_\Gamma}{\partial u_{p_i}} \right) & \text{on} \quad \Gamma_{\text{out}} \cap \Gamma_{\text{O}}, \\ \dfrac{\Phi_p \hat{\Phi}_p n_i}{\rho_p u_{p_n}} = 0 & \text{on} \quad \Gamma_{\text{out}} \setminus \Gamma_{\text{O}}. \end{cases} \tag{5.44}$$

In the case of **wall** boundaries, two situations have to be analyzed, as there are two different boundary conditions for the volume fraction. When $u_{p_n} \leq 0$, the variation of the volume fraction is zero, $\delta \Phi_p = 0$. However, when $u_{p_n} > 0$, this is not true, so $\delta \Phi_p \neq 0$. In both situations, $\delta u_{p_i} \neq 0$. Finally, it is deduced for the adjoint volume fraction that:

$$\begin{cases} \dfrac{\partial \hat{\Phi}_p}{\partial n} = 0 & \text{on} \quad \Gamma^-_{\text{wall}}, \\ \hat{\Phi}_p = \dfrac{1}{u_{p_n}} \dfrac{\partial J_\Gamma}{\partial \Phi_p} & \text{on} \quad \Gamma^+_{\text{wall}} \cap \Gamma_{\text{O}}, \\ \hat{\Phi}_p = 0 & \text{on} \quad \Gamma^+_{\text{wall}} \setminus \Gamma_{\text{O}}, \end{cases} \tag{5.45}$$

and for the adjoint velocity of particles that:

$$\hat{u}_{p_i} = \begin{cases} \dfrac{1}{\rho_p u_{p_n}} \left(\Phi_p \hat{\Phi}_p n_i - \dfrac{\partial J_\Gamma}{\partial u_{p_i}} \right) & \text{on} \quad \Gamma_{\text{wall}} \cap \Gamma_{\text{O}}, \\ \dfrac{\Phi_p \hat{\Phi}_p n_i}{\rho_p u_{p_n}} & \text{on} \quad \Gamma_{\text{wall}} \setminus \Gamma_{\text{O}}. \end{cases} \tag{5.46}$$

5.1.3.2 Gradient equation

Considering the adjoint boundary conditions on $\Gamma \setminus \Gamma_{\text{D}}$, Eq. (5.34) reduces to:

$$\delta L = \int_{\Gamma_{\text{O}} \cap \Gamma_{\text{D}}} \delta_\beta J_\Gamma \, \mathrm{d}\Gamma - \int_{\Gamma_{\text{D}}} \hat{u}_i \left[\mu \left(\frac{\partial (\delta u_i)}{\partial n} + \frac{\partial (\delta u_n)}{\partial x_i} \right) \right] \mathrm{d}\Gamma \tag{5.47a}$$

$$+ \int_{\Gamma_{\text{D}}} \delta u_i \left[\rho u_n \hat{u}_i + \mu \left(\frac{\partial \hat{u}_i}{\partial n} + \frac{\partial \hat{u}_n}{\partial x_i} \right) - \hat{p} n_i \right] \mathrm{d}\Gamma + \int_{\Gamma_{\text{O}} \cap \Gamma_{\text{D}}} \delta u_i \left(\frac{\partial J_\Gamma}{\partial u_i} \right) \mathrm{d}\Gamma \tag{5.47b}$$

$$+\int_{\Gamma_{\mathrm{D}}} \delta p\left(\hat{u}_n\right) \mathrm{d}\Gamma + \int_{\Gamma_{\mathrm{O}}\cap\Gamma_{\mathrm{D}}} \delta p\left(\frac{\partial J_\Gamma}{\partial p}\right) \mathrm{d}\Gamma + \int_{\Gamma_{\mathrm{D}}} \delta u_{p_i}\left(\rho_p \hat{u}_{p_i} u_{p_n} - \hat{\Phi}_p \Phi_p n_i\right) \mathrm{d}\Gamma \tag{5.47c}$$

$$+\int_{\Gamma_{\mathrm{O}}\cap\Gamma_{\mathrm{D}}} \delta u_{p_i}\left(\frac{\partial J_\Gamma}{\partial u_{p_i}}\right) \mathrm{d}\Gamma - \int_{\Gamma_{\mathrm{D}}} \delta \Phi_p\left(\hat{\Phi}_p u_{p_n}\right) \mathrm{d}\Gamma + \int_{\Gamma_{\mathrm{O}}\cap\Gamma_{\mathrm{D}}} \delta \Phi_p\left(\frac{\partial J_\Gamma}{\partial \Phi_p}\right) \mathrm{d}\Gamma. \tag{5.47d}$$

Based on this updated equation of the variation of the Lagrange function, the gradient of the shape optimization problem can be found.

Furthermore, it is known that spatial disturbances on the design surface are represented by displacements in the normal direction, Eq. (3.71), and $\Gamma_{\mathrm{D}} \subset \Gamma_{\mathrm{wall}}$, which leads to:

$$\begin{aligned}
\delta L = &\int_{\Gamma_{\mathrm{O}}\cap\Gamma_{\mathrm{D}}} \delta n\left(\frac{\partial J_\Gamma}{\partial n}\right) \mathrm{d}\Gamma + \int_{\Gamma_{\mathrm{O}}\cap\Gamma_{\mathrm{D}}} \delta u_i\left(\frac{\partial J_\Gamma}{\partial u_i}\right) \mathrm{d}\Gamma \\
&+\int_{\Gamma_{\mathrm{D}}} \delta u_i\left[\mu\left(\frac{\partial \hat{u}_i}{\partial n} + \frac{\partial \hat{u}_n}{\partial x_i}\right) - \hat{p} n_i\right] \mathrm{d}\Gamma - \int_{\Gamma_{\mathrm{D}}} \hat{u}_i\left[\mu\left(\frac{\partial(\delta u_i)}{\partial n} + \frac{\partial(\delta u_n)}{\partial x_i}\right)\right] \mathrm{d}\Gamma \\
&+\int_{\Gamma_{\mathrm{D}}} \delta p\left(\hat{u}_n\right) \mathrm{d}\Gamma + \int_{\Gamma_{\mathrm{O}}\cap\Gamma_{\mathrm{D}}} \delta p\left(\frac{\partial J_\Gamma}{\partial p}\right) \mathrm{d}\Gamma \\
&+\int_{\Gamma_{\mathrm{D}}} \delta u_{p_i}\left(\rho_p \hat{u}_{p_i} u_{p_n} - \hat{\Phi}_p \Phi_p n_i\right) \mathrm{d}\Gamma + \int_{\Gamma_{\mathrm{O}}\cap\Gamma_{\mathrm{D}}} \delta u_{p_i}\left(\frac{\partial J_\Gamma}{\partial u_{p_i}}\right) \mathrm{d}\Gamma \\
&-\int_{\Gamma_{\mathrm{D}}} \delta \Phi_p\left(\hat{\Phi}_p u_{p_n}\right) \mathrm{d}\Gamma + \int_{\Gamma_{\mathrm{O}}\cap\Gamma_{\mathrm{D}}} \delta \Phi_p\left(\frac{\partial J_\Gamma}{\partial \Phi_p}\right) \mathrm{d}\Gamma.
\end{aligned} \tag{5.48}$$

Evaluating the adjoint boundary conditions on Γ_{wall}, Eqs. (5.45) and (5.46) imply that:

$$\begin{aligned}
\delta L = &\int_{\Gamma_{\mathrm{O}}\cap\Gamma_{\mathrm{D}}} \delta n\left(\frac{\partial J_\Gamma}{\partial n}\right) \mathrm{d}\Gamma + \int_{\Gamma_{\mathrm{O}}\cap\Gamma_{\mathrm{D}}} \delta u_i\left(\frac{\partial J_\Gamma}{\partial u_i}\right) \mathrm{d}\Gamma \\
&+\int_{\Gamma_{\mathrm{D}}} \delta u_i\left[\mu\left(\frac{\partial \hat{u}_i}{\partial n} + \frac{\partial \hat{u}_n}{\partial x_i}\right) - \hat{p} n_i\right] \mathrm{d}\Gamma - \int_{\Gamma_{\mathrm{D}}} \hat{u}_i\left[\mu\left(\frac{\partial(\delta u_i)}{\partial n} + \frac{\partial(\delta u_n)}{\partial x_i}\right)\right] \mathrm{d}\Gamma \\
&+\int_{\Gamma_{\mathrm{D}}} \delta p\left(\hat{u}_n\right) \mathrm{d}\Gamma + \int_{\Gamma_{\mathrm{O}}\cap\Gamma_{\mathrm{D}}} \delta p\left(\frac{\partial J_\Gamma}{\partial p}\right) \mathrm{d}\Gamma \\
&-\int_{\Gamma_{\mathrm{D}}^{-}} \delta \Phi_p\left(\hat{\Phi}_p u_{p_n}\right) \mathrm{d}\Gamma + \int_{\Gamma_{\mathrm{O}}\cap\Gamma_{\mathrm{D}}^{-}} \delta \Phi_p\left(\frac{\partial J_\Gamma}{\partial \Phi_p}\right) \mathrm{d}\Gamma.
\end{aligned} \tag{5.49}$$

In the specific case of $\partial J_\Gamma/\partial p = 0$, the boundary condition for the adjoint velocity is $\hat{u}_i = 0$, and so:

$$\begin{aligned}
\delta L = &\int_{\Gamma_{\mathrm{O}}\cap\Gamma_{\mathrm{D}}} \delta n\left(\frac{\partial J_\Gamma}{\partial n}\right) \mathrm{d}\Gamma + \int_{\Gamma_{\mathrm{O}}\cap\Gamma_{\mathrm{D}}} \delta u_i\left(\frac{\partial J_\Gamma}{\partial u_i}\right) \mathrm{d}\Gamma + \int_{\Gamma_{\mathrm{O}}\cap\Gamma_{\mathrm{D}}^{-}} \delta \Phi_p\left(\frac{\partial J_\Gamma}{\partial \Phi_p}\right) \mathrm{d}\Gamma \\
&+\int_{\Gamma_{\mathrm{D}}} \delta u_i\left[\mu\left(\frac{\partial \hat{u}_i}{\partial n} + \frac{\partial \hat{u}_n}{\partial x_i}\right) - \hat{p} n_i\right] \mathrm{d}\Gamma - \int_{\Gamma_{\mathrm{D}}^{-}} \delta \Phi_p\left(\hat{\Phi}_p u_{p_n}\right) \mathrm{d}\Gamma.
\end{aligned} \tag{5.50}$$

As a result of the shape disturbances, the boundary conditions of the design surface undergo variations, i.e., $\delta u_i \neq 0$ and $\delta \Phi_p \neq 0$. Then, the local variation of velocity is approximated by Eq. (3.77), which can be extended for the local variation of volume fraction:

$$\delta \Phi_p \approx -\delta n \frac{\partial \Phi_p}{\partial n} \quad \text{on} \quad \Gamma_\mathrm{D}^-. \tag{5.51}$$

Thereafter, Eq. (5.50) looks like:

$$\begin{aligned}\delta L = &\int_{\Gamma_\mathrm{O} \cap \Gamma_\mathrm{D}} \delta n \left(\frac{\partial u_i}{\partial n} \frac{\partial J_\Gamma}{\partial n} \right) \, \mathrm{d}\Gamma - \int_{\Gamma_\mathrm{O} \cap \Gamma_\mathrm{D}} \delta n \left(\frac{\partial J_\Gamma}{\partial u_i} \right) \, \mathrm{d}\Gamma - \int_{\Gamma_\mathrm{O} \cap \Gamma_\mathrm{D}^-} \delta n \left(\frac{\partial \Phi_p}{\partial n} \frac{\partial J_\Gamma}{\partial \Phi_p} \right) \, \mathrm{d}\Gamma \\ &- \int_{\Gamma_\mathrm{D}} \delta n \left[\mu \left(\frac{\partial \hat{u}_i}{\partial n} + \frac{\partial \hat{u}_n}{\partial x_i} \right) \frac{\partial u_i}{\partial n} \right] \, \mathrm{d}\Gamma + \int_{\Gamma_\mathrm{D}^-} \delta n \left(\hat{\Phi}_p u_{p_n} \frac{\partial \Phi_p}{\partial n} \right) \, \mathrm{d}\Gamma.\end{aligned} \tag{5.52}$$

Finally, the gradient can be calculated by:

$$\delta L = G \delta n \quad \text{with} \quad G = \int_{\Gamma_\mathrm{D}} \left[-\mu \left(\frac{\partial \hat{u}_i}{\partial n} + \frac{\partial \hat{u}_n}{\partial x_i} \right) \frac{\partial u_i}{\partial n} + G_\mathrm{var} \right] \mathrm{d}\Gamma, \tag{5.53}$$

and

$$G_\mathrm{var} = \begin{cases} \dfrac{\partial J_\Gamma}{\partial n} - \dfrac{\partial J_\Gamma}{\partial u_i} \dfrac{\partial u_i}{\partial n} + \left(\hat{\Phi}_p u_{p_n} - \dfrac{\partial J_\Gamma}{\partial \Phi_p} \right) \dfrac{\partial \Phi_p}{\partial n} & \text{on} \quad \Gamma_\mathrm{D}^- \cap \Gamma_\mathrm{O}, \\ \hat{\Phi}_p u_{p_n} \dfrac{\partial \Phi_p}{\partial n} & \text{on} \quad \Gamma_\mathrm{D}^- \setminus \Gamma_\mathrm{O}, \\ \dfrac{\partial J_\Gamma}{\partial n} - \dfrac{\partial J_\Gamma}{\partial u_i} \dfrac{\partial u_i}{\partial n} & \text{on} \quad \Gamma_\mathrm{D}^+ \cap \Gamma_\mathrm{O}, \\ 0 & \text{on} \quad \Gamma_\mathrm{D}^+ \setminus \Gamma_\mathrm{O}, \end{cases} \tag{5.54}$$

5.1.3.3 Maximizing deposition efficiency

Maximizing the particle efficiency of deposition on wall surfaces, Eq. (5.12), leads to the respective objective function:

$$J = -\frac{1}{\dot{m}_{p,\mathrm{in}}} \int_{\Gamma_\mathrm{wall}} \rho_p \Phi_p u_{p_i} n_i \, \mathrm{d}\Gamma. \tag{5.55}$$

For this objective function, it is given that:

$$J_\Omega = 0 \quad \text{on} \quad \Omega, \tag{5.56}$$

$$J_\Gamma = \begin{cases} -\dfrac{\rho_p \, \Phi_p \, u_{p_i} \, n_i}{\dot{m}_{p,\text{in}}} & \text{on} \quad \Gamma_\text{wall}, \\ \\ 0 & \text{on} \quad \Gamma \setminus \Gamma_\text{wall}. \end{cases} \tag{5.57}$$

Then, the derivatives related to the state variables and control are:

$$\frac{\partial J_\Gamma}{\partial u_i} = \frac{\partial J_\Gamma}{\partial p} = 0 \quad \text{on} \quad \Gamma_\text{wall}, \tag{5.58}$$

$$\frac{\partial J_\Gamma}{\partial u_{p_i}} = -\frac{\rho_p \, \Phi_p \, n_i}{\dot{m}_{p,\text{in}}} \quad \text{on} \quad \Gamma_\text{wall}, \tag{5.59}$$

$$\frac{\partial J_\Gamma}{\partial \Phi_p} = -\frac{\rho_p \, u_{p_n}}{\dot{m}_{p,\text{in}}} \quad \text{on} \quad \Gamma_\text{wall}, \tag{5.60}$$

$$\frac{\partial J_\Gamma}{\partial n} = -\frac{\rho_p}{\dot{m}_{p,\text{in}}} \left(\Phi_p \frac{\partial u_{p_n}}{\partial n} + u_{p_n} \frac{\partial \Phi_p}{\partial n} \right) \quad \text{on} \quad \Gamma_\text{wall}. \tag{5.61}$$

It can be inferred by substituting the derivatives and the primal boundary conditions into the adjoint boundary conditions that:

$$\hat{u}_i = 0 \quad \text{on} \quad \Gamma_\text{in} \text{ and } \Gamma_\text{wall}, \tag{5.62}$$

$$\hat{p} = \rho \, u_n \, \hat{u}_n + \mu \frac{\partial \hat{u}_n}{\partial n} \quad \text{on} \quad \Gamma_\text{out}, \tag{5.63}$$

$$\rho \, u_n \, \hat{u}_t + \mu \frac{\partial \hat{u}_t}{\partial n} = 0 \quad \text{on} \quad \Gamma_\text{out}, \tag{5.64}$$

$$\rho \, u_n \, \hat{u}_s + \mu \frac{\partial \hat{u}_s}{\partial n} = 0 \quad \text{on} \quad \Gamma_\text{out}, \tag{5.65}$$

$$\hat{u}_{p_i} = 0 \quad \text{on} \quad \Gamma_{\text{out}} \text{ and } \Gamma_{\text{wall}}, \tag{5.66}$$

$$\hat{\Phi}_p = 0 \quad \text{on} \quad \Gamma_{\text{out}}, \tag{5.67}$$

$$\begin{cases} \dfrac{\partial \hat{\Phi}_p}{\partial n} = 0 & \text{on} \quad \Gamma^{-}_{\text{wall}}, \\ \hat{\Phi}_p = -\dfrac{\rho_p}{\dot{m}_{p,\text{in}}} & \text{on} \quad \Gamma^{+}_{\text{wall}}. \end{cases} \tag{5.68}$$

For those that are not shown, the zero Neumann condition is applied.

The sensitivity derivatives for maximizing the deposition efficiency of particles can be estimated from Eqs. (5.53) and (5.54) as:

$$G = -\int_{\Gamma_{\text{D}}} \left[\mu \left(\frac{\partial \hat{u}_i}{\partial n} + \frac{\partial \hat{u}_n}{\partial x_i} \right) \frac{\partial u_i}{\partial n} \right] \text{d}\Gamma + \int_{\Gamma^{-}_{\text{D}}} \left(\hat{\Phi}_p u_{p_n} \frac{\partial \Phi_p}{\partial n} \right) \text{d}\Gamma. \tag{5.69}$$

5.2 Numerical-computational modeling

The same numerical-computational modeling presented in Section 3.2 is applicable in this chapter. However, specific aspects concerning the employment of the Euler-Euler approach within the UNSCYFL3D code must be discussed. It is worth noting that the procedure used to solve the primal system of particles is reused for the adjoint system.

The discretization of the advective terms of the linear momentum equations of particles is done by using the second-order upwind scheme. For the transport equations of volume fraction, the advective term is discretized with the first-order upwind scheme. Regarding the advective terms of the adjoint equations, the downwind scheme was used. The system of linear equations for each variable is resolved sequentially (first, the volume fraction and, then, the particle velocity components) and independently by the biconjugate gradient method. Due to the coupling between the variables, the process is repeated until all the equation residues are reduced to the specified tolerance.

The shape optimization process incorporating the transport of particles in a fluid flow in UNSCYFL3D is now represented by the flowchart in Fig. 5.1. Basically, it follows the same logic explained for Fig. 3.2. One difference is that, within the optimization loop, the particle primal equations are solved after the primal equations of fluid dynamics. Furthermore, as the solution of the fluid adjoint field relies on the particle adjoint field, the particle adjoint equations are solved before the fluid adjoint equations.

Figure 5.1 – Shape optimization flowchart for multiphase flow systems.

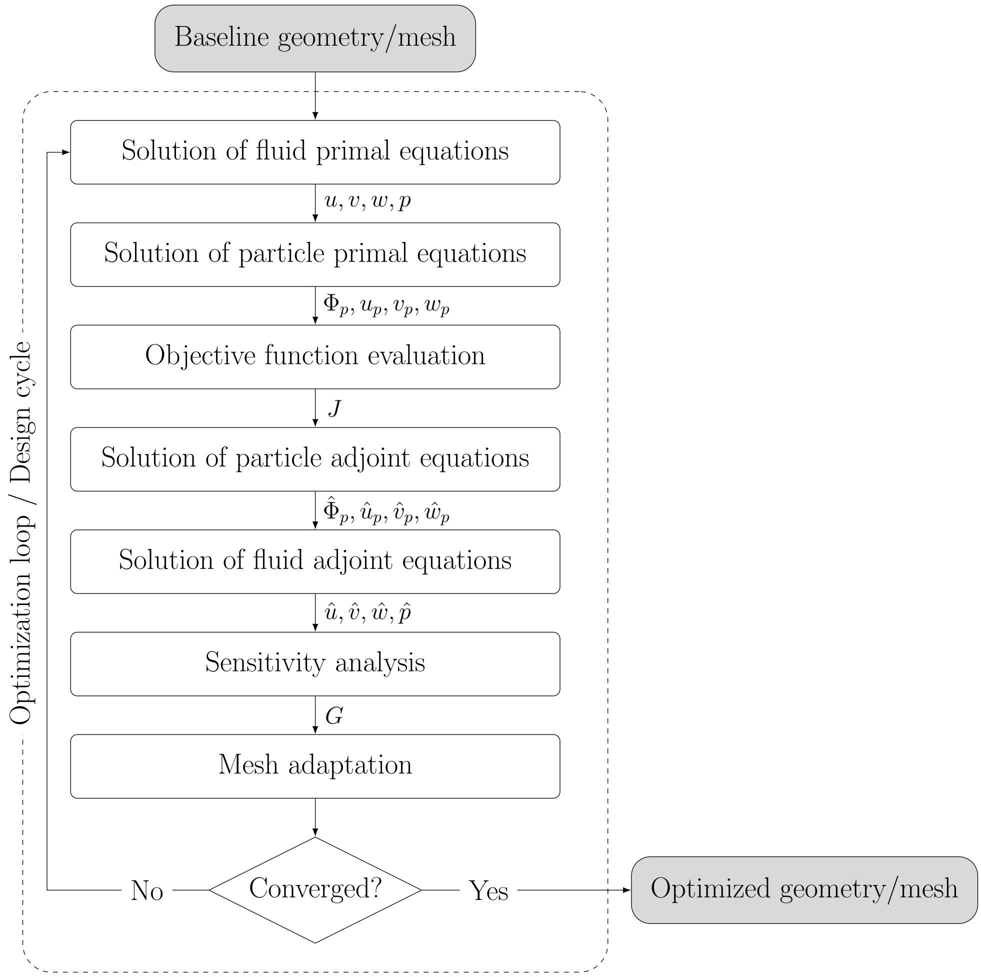

5.3 Validation of Eulerian particle equations

The experimental study presented by Pui, Romay-Novas, and Liu (1987) is considered to validate the Eulerian equations of particle transport. The problem in question focuses on the mechanism of inertial deposition of aerosol particles in bends. Starting with a less complex problem, the validation is assumed for a laminar flow and low Stokes numbers.

A schematic diagram of the used system is shown in Fig. 5.2. The 90° bend was built with a curvature radius of R_b, a pipe diameter of $d = 3.95$ mm, and a curvature ratio of $R_b/0.5d = 5.7$. Moreover, it was set up with a horizontal inlet section sufficiently long so that a fully developed flow profile was obtained prior to the bend. Table 5.1 summarizes the fluid and particle properties.

Figure 5.2 – 90° bend details of the particle deposition case.

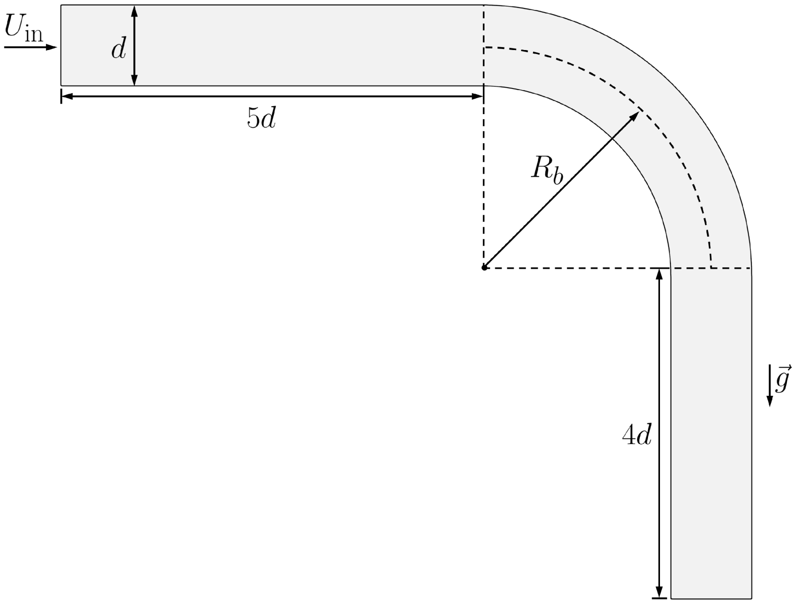

Table 5.1 – Fluid and particle properties for the investigation of particle deposition.

Fluid properties	
Fluid	Air
Density (kg/m^3)	1.196
Dynamic viscosity (Pa·s)	1.52×10^{-5}
Inlet velocity (m/s)	3.86
Reynolds number	1 000

Particle properties	
Density (kg/m^3)	907
Inlet volume fraction	10^{-6}
Stokes number	$0.17, 0.28, 0.33, 0.44, 0.57,$ $0.70, 0.90, 1.12, 1.24$

The hexahedral mesh, Fig. 5.3, used in this case was generated with 295 776 cells. Simulations were performed for several Stokes numbers to obtain the efficiency curve for particle deposition. The deposition efficiency was calculated on the bend surface according to Eq. (5.12).

Figure 5.3 – Hexahedral mesh with 295 776 cells of the 90° bend of the particle deposition case.

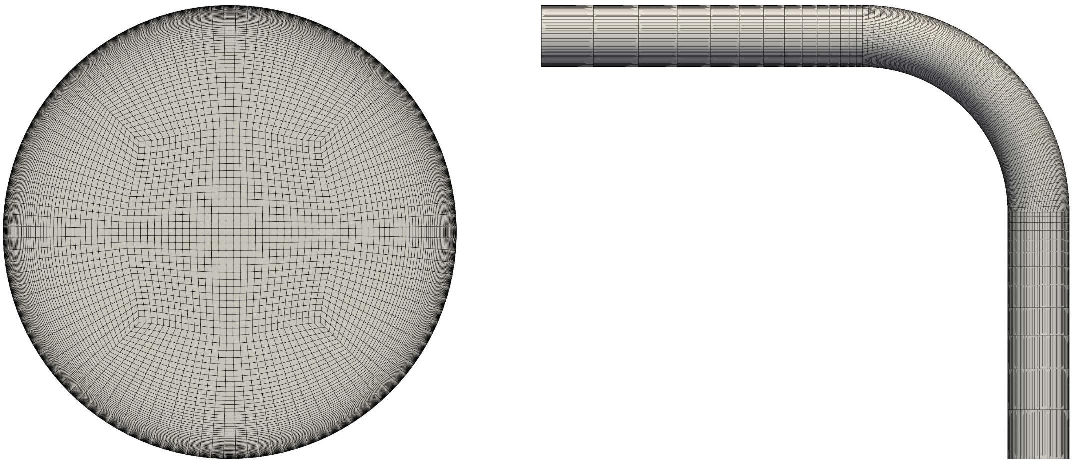

(a) Perpendicular face.

(b) Side View.

The results obtained from UNSCYFL3D with the Euler-Euler approach are compared to the experimental data of Pui, Romay-Novas, and Liu (1987) in Fig. 5.4. The efficiency curve of the present work practically meets the experimental curve. Small deviations between the two datasets are noticed. This discrepancy can be quantitatively assessed by determining the relative differences between the numerical and experimental results in terms of deposition efficiency. Consequently, the greatest calculated differences are 7.87 % for $St = 0.44$, 7.33 % for $St = 0.33$, 4.32 % for $St = 0.57$, and 3.70 % for $St = 1.24$. Still, there is good agreement between both curves. Therefore, it can be considered that the Eulerian particle equations were validated for this range of Stokes numbers.

Figure 5.4 – Comparison of deposition efficiency for the Euler-Euler simulation and experimental data (PUI; ROMAY-NOVAS; LIU, 1987).

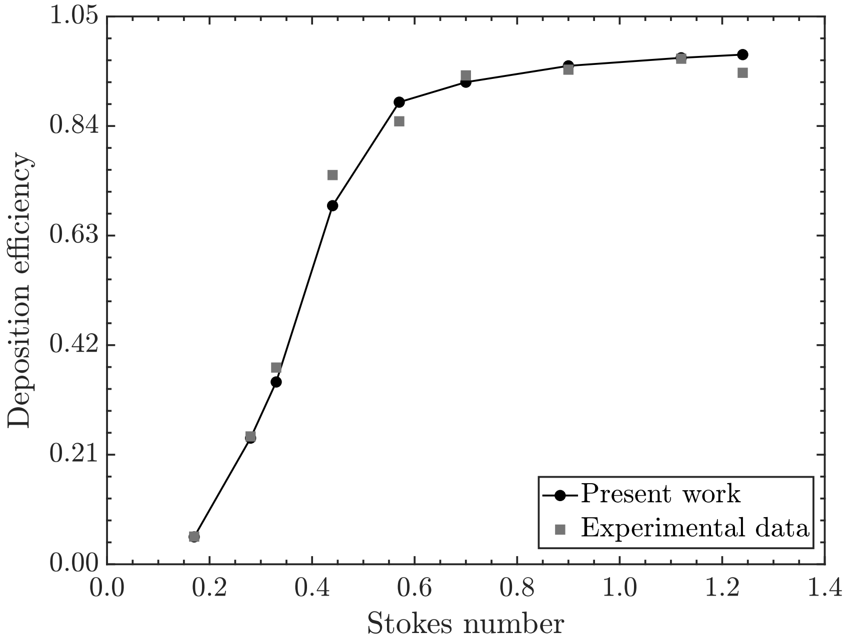

5.4 Results and discussion

The shape optimization process depicted in Fig. 5.1 was executed for the same system above in the case of $St = 0.28$. The process starts with the baseline mesh shown in Fig. 5.3. The purpose of the optimization is to find an improved bend shape for maximizing the deposition efficiency of particles based on the continuous adjoint approach.

As in Section 3.4.2, the steepest descent algorithm was run and the shape modification was achieved with the FFD technique. Then, a box around the design surface was defined as the control volume, with a minimum limit at (1.50, 0.40, -0.25) cm and a maximum limit at (3.60, -1.70, 0.25) cm, and also with $9 \times 9 \times 9$ control points, as illustrated in Fig. 5.5. The coordinate system was positioned at the center of the inlet face.

The evolution of the objective function value is plotted in Fig. 5.6. Two steps were applied for the steepest descent algorithm. It was run initially for $\lambda = 10^{-6}$, as can be seen in Fig. 5.6, the deposition efficiency increases monotonically in the first 15 design cycles. However, the optimization process diverges after that, and the objective function starts to decrease. Accordingly, a new run was set up with a smaller step, $\lambda = 10^{-7}$.

Likewise, the deposition efficiency increases from 0.2418 to a maximum value of 0.2845 around 60 design cycles, and then decreases.

Figure 5.5 – Control volume of the FFD technique around the (red) design surface.

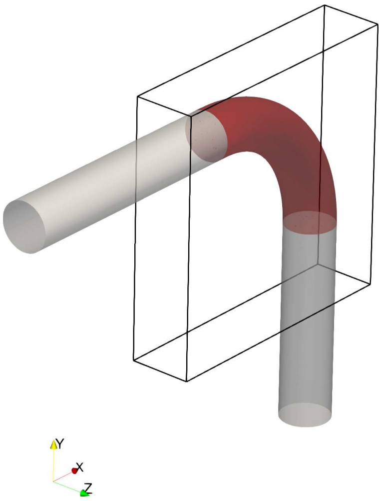

Figure 5.6 – Evolution of the particle deposition case.

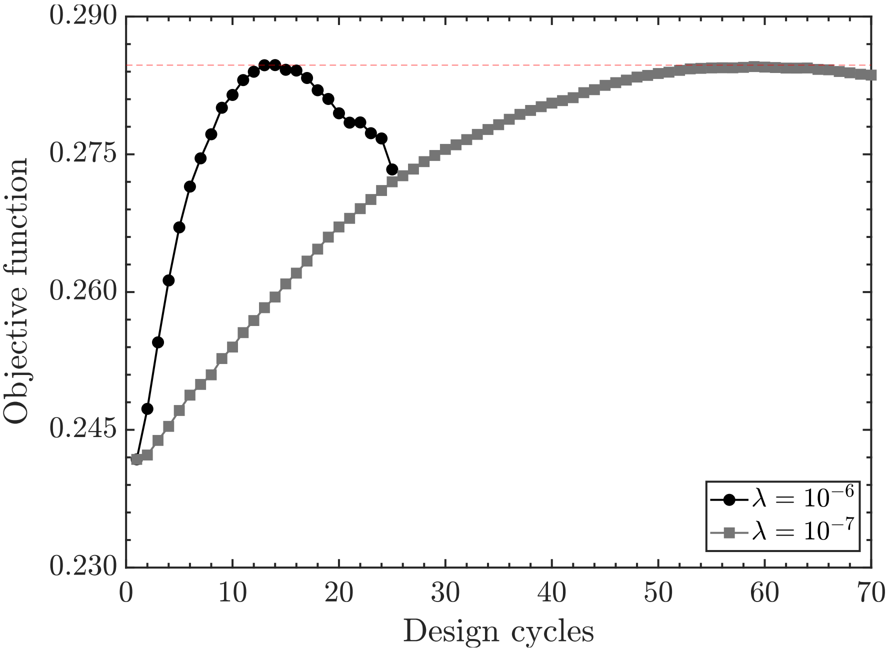

Even though the optimization process diverged, it was possible to find an improved design for which the objective function increased by approximately 18 %. This optimized shape for maximizing the deposition efficiency is illustrated in comparison with the baseline shape in Fig. 5.7. In order to visualize the particle deposition profile on the bend wall, Fig. 5.8 is presented. Such information is shown in terms of the mass flow rate of particles, which is symmetrical with respect to the axial axis of the pipeline. Clearly, from Fig. 5.8, more particles are deposited in the bend region of the optimized geometry than in the baseline geometry.

Figure 5.7 – Overlapping geometries of the optimization case of particle deposition.

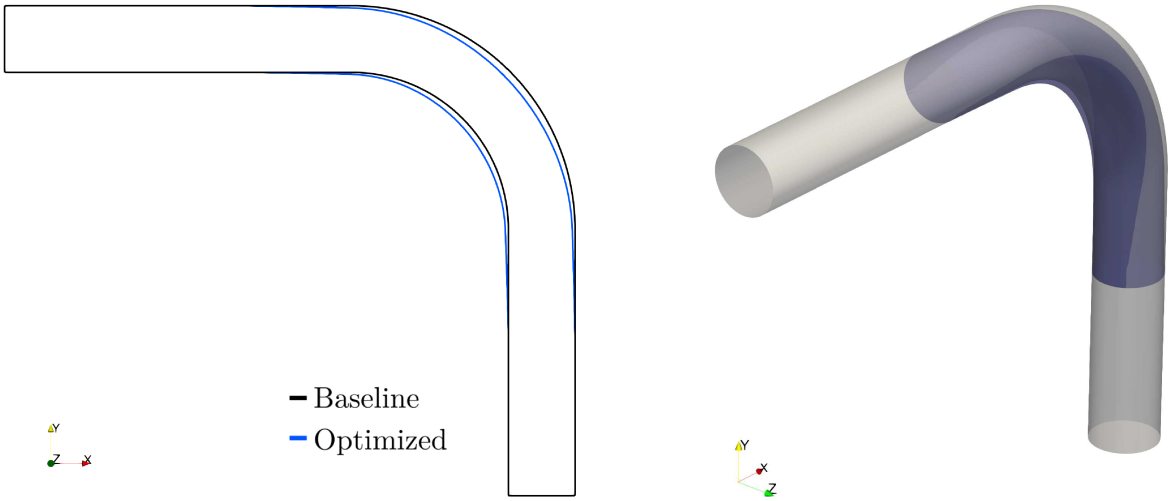

(a) Profile in side view.

(b) Perspective view.

Figure 5.8 – Deposition of particles in the bend in terms of mass flow rate.

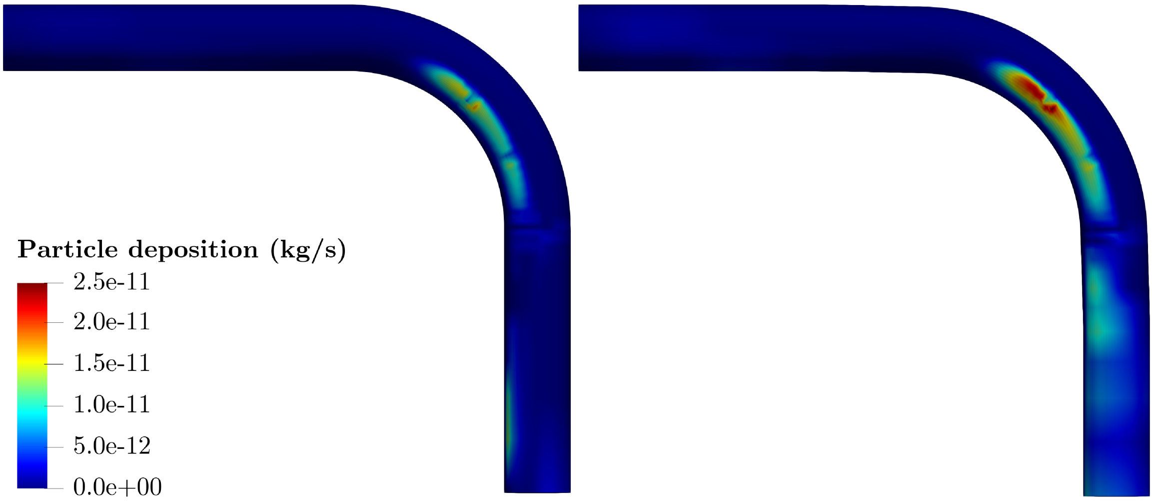

(a) Baseline.

(b) Optimized.

Addressing the convergence problem remains essential to achieving improved results. In the next section, the challenges encountered will be outlined, and measures will be proposed to overcome the issues pertinent to this chapter.

5.4.1 Challenges

Several challenges were faced during the present optimization problem that may have affected the obtained results. Solving the adjoint equations for particle transport proved to be particularly problematic due to their numerical stiffness. This inherent stiffness posed a significant obstacle to achieving convergence, as the residuals associated with the adjoint volume fraction stopped decaying over the iterations, leading to convergence stagnation. Some steps were taken to address this issue: the numerical methods available in UNSCYFL3D were verified, and it was considered using a more robust discretization scheme for the advection terms (first order downwind); different initial conditions were tested; and the solver settings were adjusted. The adjoint equations, being of mathematical origin, lack a physical interpretation, which makes it difficult to estimate the initial field. Starting the adjoint volumetric fraction field at the same order of magnitude as the boundary condition on the wall helped. Conversely, it was necessary to change the under-relaxation factor of the solver a few times during the simulation, which made the process inefficient. Consequently, the use of other methods is certainly required to solve these adjoint equations. As this is beyond the scope of the thesis, the exploration of numerical methods better suited to address the problem at hand is intended for future work.

Selecting the control volume and determining the number of control points for the FFD technique posed significant challenges. It was noticed that modifying these parameters had a substantial impact on the behavior of the objective function throughout the optimization process. Notably, defining a control volume at the boundaries of the design surface resulted in sudden deformations in those particular regions. On the other hand, defining a control volume encompassing areas that extend far beyond the design surface led to deformations that ended up hindering the convergence of the optimization process. Therefore, further analysis may be necessary to better understand these implications.

The robustness of the optimization process still needs to be improved. This can be done by choosing a more suitable algorithm for optimizing problems with adjoint equations for multiphase flows. For instance, considering the use of quasi-Newton methods could be beneficial and worth exploring in future tests (BOGER, 2013).

5.5 Conclusions

While adjoint-based shape optimization techniques have proven effective in various engineering areas, in the context of multiphase flows, their application presents its own set of challenges and limitations. In this study, significant efforts were dedicated to deriving the adjoint equations, boundary conditions, and gradient calculations using an Euler-Euler approach. The challenges started with the development of the adjoint equations themselves, which demand a strong mathematical foundation. Finding appropriate hypotheses and assumptions to simplify the problems becomes crucial, but it requires rigorous mathematical analysis.

Based on the knowledge and formulation of shape optimization for single-phase flows established in Chapter 3, this thesis extended its focus to explore the specificities of multiphase flow systems. The complexity of the problem increased as four additional equations needed to be defined and solved within the adjoint method.

Before determining the adjoint particle equations, the primal particle equations were implemented within the UNSCYFL3D code using a two-fluid model. These equations were validated with experimental data on particle deposition on a pipe bend wall under laminar flow conditions and low Stokes numbers. In pursuit of maximizing particle deposition efficiency for the aforementioned case, other challenges arose in terms of the convergence of the optimization process.

Although there are still some technical issues to be resolved, this research has its importance. It presents the complete step-by-step mathematical development for adjoint particle equations, boundary conditions, and sensitivity derivatives. It also highlights the inherent challenges and limitations associated with adjoint-based shape optimization in the realm of multiphase flows. These difficulties emphasize the need for further exploration and advancements in both theoretical formulations and numerical methods to overcome the convergence issues and, thus, fully exploit the potential of this optimization technique.

CHAPTER VI

OUTLOOK AND FINAL REMARKS

The concepts of adjoint applied to CFD were derived and implemented in this work, allowing efficient shape optimization with respect to a large number of shape parameters. The adjoint methods offer an inexpensive calculation of the gradient by formulating an additional set of equations known as adjoint equations, which must be solved after the primal flow field.

While adjoint methods for single-phase flows have been the subject of exhaustive research since the pioneering works of Pironneau (1974) and Jameson (1988), adjoint methods tailored for multiphase flows are less represented and described in the literature. The complex nature of such flows poses significant challenges for modeling. Therefore, the objective of this thesis was to address the knowledge gap by focusing on adjoint-based shape optimization involving the simulation of multiphase flow systems in a finite volume CFD code.

The development of the present work was divided into three main parts. The first part was intended to acquire more experience and knowledge in the use of the adjoint method through mathematical deductions, numerical implementations, and shape optimization applied to single-phase flows. Implementing PDEs in a finite volume CFD solver requires them to be in discretized form. There are two conceivable options for deriving the discretized adjoint equations: following the discrete adjoint approach or the continuous adjoint approach. In the case of the UNSCYFL3D code, the continuous adjoint approach was chosen for implementation. This choice was motivated by its ease of application to simulation procedures that use segregated solvers and also by the fact that the continuous adjoint inherits the computational efficiency of the primal solver due to extensive reuse of software modules. The shape optimization process was performed using a steepest descent algorithm on a CAD-free framework as the FFD, a mesh deformation technique, was employed. Classical CAD-based strategies considerably reduce the dimension of the design space, which restricts optimal shape detection and reduces the attainable improvements. The FFD technique, on the other hand, provides a more flexible shape modification. To add confidence to the simulations, the implemented adjoint equations were first validated by comparing the numerical predictions against analytical solution results for an axis-symmetric Couette flow. Furthermore, the direct-differentiation method was used to verify the adjoint solver, simulating an internal flow in an S-shaped duct. A good agreement in the sensitivity derivatives was achieved between both methods. Finally, the shape of three pipe fittings was optimized to minimize the total pressure losses of a turbulent gas flow. Even though the turbulence field was frozen in the adjoint analysis, the objective function was reduced by approximately 15 %, 22 %, and 37 % for the 45°, 90°, and 180° pipe bends, respectively. Unusual shapes were obtained, but with modern manufacturing techniques, these new designs should have no major problems being manufactured.

In the second part of the thesis, a particle-related problem was approached to evaluate the effects of the optimization done previously. Consequently, a gas-solid flow was investigated in all three bend cases, considering both the original and the optimized ones. The optimized geometries were compared with the original geometries regarding erosion wear. The erosive effect was then analyzed for three different Stokes numbers. It was concluded that the optimization favored erosion reduction, although the objective function was applied to a single-phase flow. The gains from optimization were remarkable, independently of the Stokes number. In the case of the 45° pipe bend, the maximum value of the penetration ratio decreased by about 60 % to 70 %. In the case of the 90° pipe bend, the maximum value of the penetration ratio decreased by approximately 45 % up to 85 %, for highly inertial particles and low-inertia particles, respectively. These results were similar to those of the 180° pipe bend, in which the reduction ranged from 32 % to 84 %.

The explanation for such secondary gains consists of the reduction of the impact velocity and frequency of the particles against the bend walls.

Shape optimization problems involving a dispersed phase require the extension of the adjoint system by additional PDE constraints. Different approaches are available to model multiphase flows, each more appropriate according to a specific scenario, as presented in Section 2.2. For fluid flows carrying particles, the Euler-Lagrange approach is commonly used, in which a Lagrangian particle tracking method is employed. Another approach is rarely explored, for example, in studies on erosion simulation, as in the erosion problem presented above. Nevertheless, modeling the dispersed phase as Lagrangian particles has certain fundamental limitations that make it difficult to use with adjoint concepts. To overcome this, in the third part of the thesis, adjoint equations were obtained regarding the Euler-Euler approach. Therefore, a new approach was introduced to optimize the shape of multiphase flow systems. Up to this point, an 18 % increase in the efficiency of particle deposition in bends for $St = 0.28$ has been achieved through this approach. It is believed that further improvements can be obtained by dealing with the technical issues faced during the optimization process.

Throughout the course of this thesis, some limitations and challenges were encountered, underscoring the complexities inherent in the adjoint-based shape optimization applied to CFD. These limitations include the consideration of only steady-state flows, the assumption of frozen turbulence, and the adoption of a simplified model for the transport of particles in an Eulerian description. In addition, the research faced various challenges, such as ensuring the convergence of the Eulerian particle equations and the convergence of the optimization process applied to the fluid-particle flow. However, these limitations and challenges also present opportunities for future research.

Addressing unsteady simulations requires solving the corresponding adjoint problem backward in time. Thus, the implemented approach should be complemented by an adjoint time-stepping scheme (GRIEWANK; WALTHER, 2000; NADARAJAH; MCMULLEN; JAMESON, 2006; STÜCK; CAMELLI; LOHNER, 2010). Disregarding the frozen turbulence hypothesis results in complete differentiation, including the turbulence variables and the associated PDEs. This, in turn, introduces several terms that lead to a strong interdependence between the adjoint equations of linear momentum and turbulence. In order to achieve an efficient and robust adjoint method capable of calculating the full derivatives for turbulent flow problems and complex geometries, it may be necessary to develop coupled solution algorithms. Moreover, the computation of the adjoint equations and sensitivity derivatives should be extended to more advanced multiphase flow models for fluid-particle transport. The Eulerian particle equations described in this thesis do not model turbulent particle dispersion or dense flow regimes, for example.

When trying to solve the adjoint equations of the particle transport in the Euler-Euler approach, a certain numerical stiffness became evident. The solution of these equations reached convergence stagnation. It was necessary to adjust the solver parameters and settings a few times during simulations, which made the optimization process inefficient. Consequently, investing in more efficient and robust methods can be very advantageous for optimizing multiphase systems.

Concerning the difficulties of convergence in the optimization process, it was noticed that the parameters used in the FFD technique, such as the control volume and the number of control points, can interfere in finding the minimum or maximum value of the objective function. Defining a control volume at the boundaries of the design surface leads to sudden deformations in these regions. However, if the control volume encompasses parts of the domain far beyond the design surface, it may end up generating deformations that hinder the convergence process. As an in-depth analysis of the implications of FFD parameter settings has not been performed, it is recommended for future work. Another perspective is related to the optimization algorithm used, since the steepest descent method may not have been suitable for the optimization problem presented involving multiphase flow. This then requires the use of more advanced methods, for example, quasi-Newton methods.

Despite this list of technical hurdles, the present work demonstrates how to formulate and use a continuous adjoint method to calculate objective function gradients in fluid-particle flow, thus serving as the basis for a new shape optimization method for multiphase flow systems. The implemented adjoint method can also be used for optimizing other flow systems, requiring specific adjustments according to the type of problem.

REFERENCES

AGARWAL, D.; ROBINSON, T. T.; ARMSTRONG, C. G.; KAPELLOS, C. Enhancing CAD-based shape optimisation by automatically updating the CAD model's parameterisation. **Structural and Multidisciplinary Optimization**, Springer, v. 59, n. 5, p. 1639–1654, 2019. DOI: https://doi.org/10.1007/s00158-018-2152-7.

AHLERT, K. R. **Effects of particle impingement angle and surface wetting on solid particle erosion of AISI 1018 steel**. 1994. PhD thesis – University of Tulsa.

ALLETTO, M. **Numerical Investigation of the Influence of Particle-Particle and Particle-Wall Collisions in Turbulent Wall-Bounded Flows at High Mass Loadings**. 2014. PhD thesis – Institut für Mechanik. Available from: http://edoc.sub.uni-hamburg.de/hsu/volltexte/2014/3077/.

AUVINEN, M. **A Modular Framework for Generation and Maintenance of Adjoint Solvers Assisted by Algorithmic Differentiation – with Applications to an Incompressible Navier-Stokes Solver**. 2014. s. 183. PhD thesis – Aalto University, Finland. Available from: http://urn.fi/URN:ISBN:978-952-60-5883-2.

AVVARI, R.; JAYANTI, S. Heuristic shape optimization of gas ducting in process and power plants. **Chemical Engineering Research and Design**, Elsevier, v. 91, n. 6, p. 999–1008, 2013. DOI: https://doi.org/10.1016/j.cherd.2012.12.006.

BÄNGTSSON, E.; NORELAND, D.; BERGGREN, M. Shape optimization of an acoustic horn. **Computer methods in applied mechanics and engineering**, Elsevier, v. 192, n. 11–12, p. 1533–1571, 2003. DOI: https://doi.org/10.1016/S0045-7825%2802%2900656-4.

BHUSHAN, B. **Introduction to tribology**. 2. ed. New York, USA: John Wiley & Sons, 2013. p. 744. ISBN 9781118403259.

BOGER, D. A.; PATERSON, E. G. A continuous adjoint approach to design optimization in cavitating flow using a barotropic model. **Computers & Fluids**, Elsevier, v. 101, p. 155–169, 2014. DOI: https://doi.org/10.1016/j.compfluid.2014.06.014.

BOGER, D. A. **A Continuous Adjoint Approach to Design Optimization in Multiphase Flow**. 2013. PhD thesis – Pennsylvania State University, State College. Available from: https://www.researchgate.net/publication/270216166_A_Continuous_Adjoint_Approach_to_Design_Optimization_in_Multiphase_Flow.

BONNET, M.; LIU, R.; VEERAPANENI, S.; ZHU, H. Shape Optimization of Peristaltic Pumps Transporting Rigid Particles in Stokes Flow. **SIAM Journal on Scientific Computing**, v. 45, n. 1, b78–b106, 2023. DOI: https://doi.org/10.1137/21M144863X. Available from: https://arxiv.org/abs/2110.00702.

BRENNER, M.; HARRIES, S.; KRÖGER, J.; RUNG, T. Parametric-adjoint approach for the efficient optimization of flow-exposed geometries. *In:* **Proceedings of the VI International Conference on Computational Methods in Marine Engineering**, Rome, Italy. CIMNE, p. 230–241. Available from: http://hdl.handle.net/2117/332276.

BREUER, M.; ALLETTO, M.; LANGFELDT, F. Sandgrain roughness model for rough walls within Eulerian-Lagrangian predictions of turbulent flows. **International Journal of Multiphase Flow**, v. 43, p. 157–175, 2012. DOI: https://doi.org/10.1016/j.ijmultiphaseflow.2012.03.002.

CHEN, H.-C.; PATEL, V. C. Near-wall turbulence models for complex flows including separation. **AIAA journal**, v. 26, n. 6, p. 641–648, 1988. DOI: https://doi.org/10.2514/3.9948.

CHOU, P. Y. On velocity correlations and the solutions of the equations of turbulent fluctuation. **Quarterly of Applied Mathematics**, Brown University, v. 3, n. 1, p. 38–54, 1945. Available from: https://www.jstor.org/stable/43633490.

CROWE, C. T.; SCHWARZKOPF, J. D.; SOMMERFELD, M.; TSUJI, Y. **Multiphase flows with droplets and particles**. 2. ed. Boca Raton: CRC press, 2011. p. 494. ISBN 9781439840504.

CROWE, C.; TROUTT, T.; CHUNG, J. Particle interactions with vortices. *In:* GREEN, S. I. (ed.). **Fluid Vortices. Fluid Mechanics and Its Applications**. Dordrecht: Springer, 1995. v. 30. p. 829–861. ISBN 9789401102490. DOI: https://doi.org/10.1007/978-94-011-0249-0_19.

DENNIS, S.; SINGH, S.; INGHAM, D. The steady flow due to a rotating sphere at low and moderate Reynolds numbers. **Journal of Fluid Mechanics**, Cambridge University Press, v. 101, n. 2, p. 257–279, 1980. DOI: https://doi.org/10.1017/S0022112080001656.

DOSANJH, S.; HUMPHREY, J. A. The influence of turbulence on erosion by a particle-laden fluid jet. **Wear**, Elsevier, v. 102, n. 4, p. 309–330, 1985. DOI: https://doi.org/10.1016/0043-1648(85)90175-9.

DUARTE, C. A. R. **Simulation of a new pipe design for erosion reduction in curves**. 2017. PhD thesis – Universidade Federal de Uberlândia, Uberlândia. Available from: https://repositorio.ufu.br/handle/123456789/18329.

DUARTE, C. A. R.; SOUZA, F. J. de. Innovative pipe wall design to mitigate elbow erosion: A CFD analysis. **Wear**, v. 380–381, p. 176–190, 2017. DOI: https://doi.org/10.1016/j.wear.2017.03.015.

DUARTE, C. A. R.; SOUZA, F. J. de; SALVO, R. V.; SANTOS, V. F. dos. The role of inter-particle collisions on elbow erosion. **International Journal of Multiphase Flow**, v. 89, p. 1–22, 2017. DOI: https://doi.org/10.1016/j.ijmultiphaseflow.2016.10.001.

DUARTE, C. A. R.; SOUZA, F. J. de; SANTOS, V. F. dos. Numerical investigation of mass loading effects on elbow erosion. **Powder Technology**, v. 283, p. 593–606, 2015. DOI: https://doi.org/10.1016/j.powtec.2015.06.021.

DUARTE, C. A. R.; SOUZA, F. J. de; SANTOS, V. F. dos. Mitigating elbow erosion with a vortex chamber. **Powder Technology**, v. 288, p. 6–25, 2016. DOI: https://doi.org/10.1016/j.powtec.2015.10.032.

DUARTE, C. A. R.; SOUZA, F. J. de; VENTURI, D. N.; SOMMERFELD, M. A numerical assessment of two geometries for reducing elbow erosion. **Particuology**, v. 49, p. 117–133, 2020. DOI: https://doi.org/10.1016/j.partic.2019.01.004.

DWIGHT, R. P.; BREZILLON, J. Effect of approximations of the discrete adjoint on gradient-based optimization. **AIAA journal**, v. 44, n. 12, p. 3022–3031, 2006. DOI: https://doi.org/10.2514/6.2006-690.

ELGHOBASHI, S. On predicting particle-laden turbulent flows. **Applied scientific research**, Springer, v. 52, n. 4, p. 309–329, 1994. DOI: https://doi.org/10.1007/bf00936835.

ELSAYED, K. Design of a novel gas cyclone vortex finder using the adjoint method. **Separation and Purification Technology**, v. 142, p. 274–286, 2015. DOI: https://doi.org/10.1016/j.seppur.2015.01.010.

FERZIGER, J. H.; PERIĆ, M. **Computational methods for fluid dynamics**. 3., rev. ed. Berlin; Heidelberg; New York: Springer, 2002. p. 423. ISBN 3540420746.

FINNIE, I. Some observations on the erosion of ductile metals. **wear**, Elsevier, v. 19, n. 1, p. 81–90, 1972. DOI: https://doi.org/10.1016/0043-1648(72)90444-9.

GANGL, P.; LANGER, U.; LAURAIN, A.; MEFTAHI, H.; STURM, K. Shape optimization of an electric motor subject to nonlinear magnetostatics. **SIAM Journal on**

Scientific Computing, SIAM, v. 37, n. 6, b1002–b1025, 2015. DOI: https://doi.org/10.1137/15100477X.

GIBOU, F.; FEDKIW, R.; OSHER, S. A review of level-set methods and some recent applications. **Journal of Computational Physics**, Elsevier, v. 353, p. 82–109, 2018. DOI: https://doi.org/10.1016/j.jcp.2017.10.006.

GKARAGKOUNIS, K.; PAPOUTSIS-KIACHAGIAS, E.; GIANNAKOGLOU, K. The continuous adjoint method for shape optimization in Conjugate Heat Transfer problems with turbulent incompressible flows. **Applied Thermal Engineering**, Elsevier, v. 140, p. 351–362, 2018. DOI: https://doi.org/10.1016/j.applthermaleng.2018.05.054.

GLOWINSKI, R.; PIRONNEAU, O. On the numerical computation of the minimum-drag profile in laminar flow. **Journal of Fluid Mechanics**, Cambridge University Press, v. 72, n. 2, p. 385–389, 1975. DOI: https://doi.org/10.1017/S0022112075003436.

GLOWINSKI, R.; PIRONNEAU, O. Towards the computation of minimum drag profiles in viscous laminar flow. **Applied Mathematical Modelling**, Elsevier, v. 1, n. 2, p. 58–66, 1976. DOI: https://doi.org/10.1016/0307-904X(76)90001-9.

GLOWINSKI, R. On Shape Optimization and Related Issues. *In:* BORGGAARD, J.; BURNS, J.; CLIFF, E.; SCHRECK, S. (eds.). **Computational Methods for Optimal Design and Control. Progress in Systems and Control Theory**. Boston: Birkhäuser, 1998. v. 24. p. 151–179. ISBN 9781461217800. DOI: https://doi.org/10.1007/978-1-4612-1780-0_10.

GRANT, G.; TABAKOFF, W. Erosion prediction in turbomachinery resulting from environmental solid particles. **Journal of Aircraft**, v. 12, n. 5, p. 471–478, 1975. DOI: https://doi.org/10.2514/3.59826.

GRIEWANK, A.; WALTHER, A. An implementation of checkpointing for the reverse or adjoint mode of computational differentiation. **ACM Transactions on Mathematical Software (TOMS)**, v. 26, n. 1, p. 19–45, 2000. DOI: https://doi.org/10.1145/347837.347846.

HAFTKA, R. T.; GRANDHI, R. V. Structural shape optimization—A survey. **Computer methods in applied mechanics and engineering**, Elsevier, v. 57, n. 1, p. 91–106, 1986. DOI: https://doi.org/10.1016/0045-7825(86)90072-1.

HARLOW, F. H.; NAKAYAMA, P. I. **Transport of turbulence energy decay rate**. New Mexico, 1968. Available from: https://digital.library.unt.edu/ark:/67531/metadc1026296/.

HART, J. Comparison of turbulence modeling approaches to the simulation of a dimpled sphere. **Procedia Engineering**, Elsevier, v. 147, p. 68–73, 2016. DOI: https://doi.org/10.1016/j.proeng.2016.06.191.

HASELBACHER, A.; NAJJAR, F. M.; FERRY, J. P. An efficient and robust particle-localization algorithm for unstructured grids. **Journal of Computational Physics**, Elsevier, v. 225, n. 2, p. 2198–2213, 2007. DOI: https://doi.org/10.1016/j.jcp.2007.03.018.

HELGASON, E.; KRAJNOVIĆ, S. Implementation of an adjoint-based optimization with scalar transport. *In:* ASME, Montreal, Canada. **Proceedings of the ASME 2014 International Mechanical Engineering Congress and Exposition**. [*S. l.: s. n.*], 2014. v007t09a089. DOI: https://doi.org/10.1115/IMECE2014-39691.

HINTERBERGER, C.; OLESEN, M. Industrial application of continuous adjoint flow solvers for the optimization of automotive exhaust systems. *In:* **Proceedings of the ECCOMAS Thematic Conference – CFD & Optimization**, Antalya, Turkey. ECCOMAS. Available from: https://www.researchgate.net/publication/268206324_INDUSTRIAL_APPLICATION_OF_CONTINUOUS_ADJOINT_FLOW_SOLVERS_FOR_THE_OPTIMIZATION_OF_AUTOMOTIVE_EXHAUST_SYSTEMS.

HINTERMÜLLER, M.; LAURAIN, A.; YOUSEPT, I. Shape sensitivities for an inverse problem in magnetic induction tomography based on the eddy current model. **Inverse Problems**, IOP Publishing, v. 31, n. 6, p. 065006, 2015. DOI: https://doi.org/10.1088/0266-5611%2F31%2F6%2F065006.

HOHMANN, R.; LEITHÄUSER, C. Shape optimization of a bended tube minimizing particle erosion. **PAMM**, Wiley Online Library, v. 19, n. 1, e201900188, 2019a. DOI: https://doi.org/10.1002/pamm.201900188.

HOHMANN, R.; LEITHÄUSER, C. Shape optimization of a polymer distributor using an Eulerian residence time model. **SIAM Journal on Scientific Computing**, SIAM, v. 41, n. 4, b625–b648, 2019b. DOI: https://doi.org/10.1137/18M1225847.

HOJO, H.; TSUDA, K.; YABU, T. Erosion damage of polymeric material by slurry. **Wear**, Elsevier, v. 112, n. 1, p. 17–28, 1986. DOI: https://doi.org/10.1016/0043-1648(86)90197-3.

JAMESON, A. Aerodynamic design via control theory. **Journal of scientific computing**, Springer, v. 3, n. 3, p. 233–260, 1988. DOI: https://doi.org/10.1007/BF01061285.

JAMESON, A.; MARTINELLI, L.; PIERCE, N. A. Optimum aerodynamic design using the Navier-Stokes equations. **Theoretical and computational fluid dynamics**, Springer, v. 10, n. 1, p. 213–237, 1998. DOI: https://doi.org/10.1007/s001620050060.

JONES, W.; LAUNDER, B. E. The prediction of laminarization with a two-equation model of turbulence. **International journal of heat and mass transfer**, Elsevier, v. 15, n. 2, p. 301–314, 1972. DOI: https://doi.org/10.1016/0017-9310(72)90076-2.

KIM, C. S.; KIM, C.; RHO, O. H. Feasibility study of constant eddy-viscosity assumption in gradient-based design optimization. **Journal of Aircraft**, v. 40, n. 6, p. 1168–1176, 2003. DOI: https://doi.org/10.2514/2.7206.

KIM, H. J.; SASAKI, D.; OBAYASHI, S.; NAKAHASHI, K. Aerodynamic optimization of supersonic transport wing using unstructured adjoint method. **AIAA journal**, v. 39, n. 6, p. 1011–1020, 2001. DOI: https://doi.org/10.2514/2.1441.

KRÖGER, J.; KÜHL, N.; RUNG, T. Adjoint volume-of-fluid approaches for the hydrodynamic optimisation of ships. **Ship Technology Research**, Taylor & Francis, v. 65, n. 1, p. 47–68, 2018. DOI: https://doi.org/10.1080/09377255.2017.1411001.

KUIPERS, J.; VAN DUIN, K.; VAN BECKUM, F.; VAN SWAAIJ, W. P. M. A numerical model of gas-fluidized beds. **Chemical Engineering Science**, Elsevier, v. 47, n. 8, p. 1913–1924, 1992. DOI: https://doi.org/10.1016/0009-2509(92)80309-Z.

KUNGURTSEV, P. V.; JUNIPER, M. P. Adjoint-based shape optimization of the microchannels in an inkjet printhead. **Journal of Fluid Mechanics**, Cambridge University Press, v. 871, p. 113–138, 2019. DOI: https://doi.org/10.1017/jfm.2019.271.

LAÍN, S.; SOMMERFELD, M.; KUSSIN, J. Experimental studies and modelling of four-way coupling in particle-laden horizontal channel flow. **International journal of heat and fluid flow**, Elsevier, v. 23, n. 5, p. 647–656, 2002. DOI: https://doi.org/10.1016/S0142-727X(02)00160-1.

LAUNDER, B. E.; SHARMA, B. Application of the energy-dissipation model of turbulence to the calculation of flow near a spinning disc. **Letters in heat and mass transfer**, Pergamon, v. 1, n. 2, p. 131–137, 1974. DOI: https://doi.org/10.1016/0094-4548(74)90150-7.

LE MOIGNE, A. **A discrete Navier-Stokes adjoint method for aerodynamic optimisation of Blended Wing-Body configurations**. 2002. s. 124. PhD thesis – Cranfield University, Cranfield, Bedfordshire, England. Available from: http://hdl.handle.net/1826/826.

LESIEUR, M.; MÉTAIS, O.; COMTE, P. **Large-eddy simulations of turbulence**. Cambridge; New York: Cambridge University Press, 2005. ISBN 0521781248.

LEVEQUE, R. J. **Finite volume methods for hyperbolic problems**. Cambridge: Cambridge University Press, 2002. p. 580. ISBN 9780521009249.

LI, R.; SUN, Z.; LI, A.; LI, Y.; WANG, Z. Design optimization of hemispherical protrusion for mitigating elbow erosion via CFD-DPM. **Powder Technology**, Elsevier, v. 398, p. 117128, 2022. DOI: https://doi.org/10.1016/j.powtec.2022.117128.

LIONS, J. L. **Optimal control of systems governed by partial differential equations**. Berlin; Heidelberg: Springer, 1971. p. 396. ISBN 9783642650260.

LOBATO, F. S. **Multi-objective optimization for engineering system design**. 2008. s. 402. PhD thesis – Universidade Federal de Uberlândia, Uberlândia - MG, Brasil. Available from: https://repositorio.ufu.br/handle/123456789/14677.

LUN, C.; LIU, H. Numerical simulation of dilute turbulent gas-solid flows in horizontal channels. **International Journal of Multiphase Flow**, Elsevier, v. 23, n. 3, p. 575–605, 1997. DOI: https://doi.org/10.1016/S0301-9322(96)00087-0.

MAVRIPLIS, D. J. Discrete adjoint-based approach for optimization problems on three-dimensional unstructured meshes. **AIAA journal**, v. 45, n. 4, p. 741–750, 2007. DOI: https://doi.org/10.2514/1.22743.

MAZUMDER, Q. H.; SHIRAZI, S. A.; MCLAURY, B. Experimental investigation of the location of maximum erosive wear damage in elbows. **Journal of Pressure Vessel Technology**, American Society of Mechanical Engineers Digital Collection, v. 130, n. 1, 2008. DOI: https://doi.org/10.1115/1.2826426.

MEI, R. An approximate expression for the shear lift force on a spherical particle at finite Reynolds number. **International Journal of Multiphase Flow**, Elsevier, v. 18, n. 1, p. 145–147, 1992. DOI: https://doi.org/10.1016/0301-9322(92)90012-6.

MENTER, F. R. Two-equation eddy-viscosity turbulence models for engineering applications. **AIAA journal**, v. 32, n. 8, p. 1598–1605, 1994. DOI: https://arc.aiaa.org/doi/10.2514/3.12149.

MESSA, G. V.; FERRARESE, G.; MALAVASI, S. A mixed Euler-Euler/Euler-Lagrange approach to erosion prediction. **Wear**, Elsevier, v. 342, p. 138–153, 2015. DOI: https://doi.org/10.1016/j.wear.2015.08.015.

MESSA, G. V.; MALAVASI, S. A CFD-based method for slurry erosion prediction. **Wear**, Elsevier, v. 398, p. 127–145, 2018. DOI: https://doi.org/10.1016/j.wear.2017.11.025.

MICHAELIDES, E.; CROWE, C. T.; SCHWARZKOPF, J. D. **Multiphase flow handbook**. 2. ed. Boca Raton: CRC Press, 2016. p. 1394. ISBN 9781498701006.

MIRJALILI, S.; JAIN, S. S.; DODD, M. S. Interface-capturing methods for two-phase flows: An overview and recent developments. **Center for Turbulence Research Annual**

Research Briefs, p. 117–135, 2017. Available from:
http://web.stanford.edu/~sjsuresh/mirjalili2017.pdf.

MONTANELLI, H. **Multipoint shape optimization with discrete adjoint method for the design of turbomachine blades**. 2013. s. 66. MA thesis – Institut Supérieur de l'Aéronautique et de l'Espace, Toulouse, France. Available from:
https://www.cerfacs.fr/~cfdbib/repository/WN_CFD_13_74.pdf.

NADARAJAH, S.; JAMESON, A. A comparison of the continuous and discrete adjoint approach to automatic aerodynamic optimization. *In:* AIAA, Reno, USA, p. 667. DOI: https://doi.org/10.2514/6.2000-667.

NADARAJAH, S.; MCMULLEN, M.; JAMESON, A. Non-linear frequency domain based optimum shape design for unsteady three-dimensional flow. *In:* **Proceedings of the 44th AIAA Aerospace Sciences Meeting and Exhibit**, Reno, USA. AIAA, p. 1052. DOI: https://doi.org/10.2514/6.2006-1052.

NEILSON, J.; GILCHRIST, A. Erosion by a stream of solid particles. **wear**, Elsevier, v. 11, n. 2, p. 111–122, 1968. DOI: https://doi.org/10.1016/0043-1648(68)90591-7.

NOROUZI, H. R.; ZARGHAMI, R.; SOTUDEH-GHAREBAGH, R.; MOSTOUFI, N. **Coupled CFD-DEM modeling**: Formulation, implementation and application to multiphase flows. Chichester; Hoboken: John Wiley & Sons, 2016. p. 416. ISBN 9781119005315.

OKA, Y.; OKAMURA, K.; YOSHIDA, T. Practical estimation of erosion damage caused by solid particle impact. **Wear**, v. 259, n. 1, p. 95–109, 2005. DOI: https://doi.org/10.1016/j.wear.2005.01.039.

OTHMER, C. A continuous adjoint formulation for the computation of topological and surface sensitivities of ducted flows. **International journal for numerical methods in fluids**, Wiley Online Library, v. 58, n. 8, p. 861–877, 2008. DOI: https://doi.org/10.1002/fld.1770.

OTHMER, C. Adjoint methods for car aerodynamics. **Journal of Mathematics in Industry**, Springer, v. 4, n. 1, p. 6, 2014. DOI: https://doi.org/10.1186/2190-5983-4-6.

PATANKAR, S. V. **Numerical heat transfer and fluid flow**. New York, USA: Hemisphere, 1980. p. 197.

PEREIRA, G. C.; SOUZA, F. J. de; MORO MARTINS, D. A. de. Numerical prediction of the erosion due to particles in elbows. **Powder Technology**, v. 261, p. 105–117, 2014. DOI: https://doi.org/10.1016/j.powtec.2014.04.033.

PIRONNEAU, O. On optimum profiles in Stokes flow. **Journal of Fluid Mechanics**, Cambridge University Press, v. 59, n. 1, p. 117–128, 1973. DOI: https://doi.org/10.1017/S002211207300145X.

PIRONNEAU, O. On optimum design in fluid mechanics. **Journal of Fluid Mechanics**, Cambridge University Press, v. 64, n. 1, p. 97–110, 1974. DOI: https://doi.org/10.1017/S0022112074002023.

POPE, S. B. **Turbulent flows**. Cambridge; New York: Cambridge University Press, 2000. p. 771. ISBN 0521591252.

PUI, D. Y.; ROMAY-NOVAS, F.; LIU, B. Y. Experimental study of particle deposition in bends of circular cross section. **Aerosol Science and Technology**, Taylor & Francis, v. 7, n. 3, p. 301–315, 1987. DOI: https://doi.org/10.1080/02786828708959166.

QUAGLIARELLA, D.; CIOPPA, A. D. Genetic algorithms applied to the aerodynamic design of transonic airfoils. **Journal of aircraft**, v. 32, n. 4, p. 889–891, 1995. DOI: https://doi.org/10.2514/3.46810.

REUTHER, J.; JAMESON, A.; FARMER, J.; MARTINELLI, L.; SAUNDERS, D. Aerodynamic shape optimization of complex aircraft configurations via an adjoint formulation. **34th Aerospace Sciences Meeting and Exhibit**, p. 94, 1996. DOI: https://doi.org/10.2514/6.1996-94.

RIBERA, R. L. **Understanding the dynamics of gas-liquid-solid contact points**. 2015. PhD thesis – Universidade Federal de Uberlândia, Uberlândia. Available from: http://repositorio.ufu.br/handle/123456789/21285.

RICARDO, G. A. N.; SOMMERFELD, M. Experimental evaluation of surface roughness variation of ductile materials due to solid particle erosion. **Advanced Powder Technology**, Elsevier, v. 31, n. 9, p. 3790–3816, 2020. DOI: https://doi.org/10.1016/j.apt.2020.07.023.

ROACHE, P. J. Perspective: A Method for Uniform Reporting of Grid Refinement Studies. **Journal of Fluids Engineering**, v. 116, n. 3, p. 405–413, 1994. DOI: https://doi.org/10.1115/1.2910291.

ROACHE, P. J. QUANTIFICATION OF UNCERTAINTY IN COMPUTATIONAL FLUID DYNAMICS. **Annual Review of Fluid Mechanics**, v. 29, n. 1, p. 123–160, 1997. DOI: https://doi.org/10.1146/annurev.fluid.29.1.123.

ROACHE, P. J. Verification of codes and calculations. **AIAA journal**, v. 36, n. 5, p. 696–702, 1998. DOI: https://doi.org/10.2514/2.457.

RUBINOW, S. I.; KELLER, J. B. The transverse force on a spinning sphere moving in a viscous fluid. **Journal of Fluid Mechanics**, Cambridge University Press, v. 11, n. 3, p. 447–459, 1961. DOI: https://doi.org/10.1017/S0022112061000640.

SAFFMAN, P. The lift on a small sphere in a slow shear flow. **Journal of Fluid Mechanics**, Cambridge University Press, v. 22, n. 2, p. 385–400, 1965. DOI: https://doi.org/10.1017/s0022112065000824.

SAFIKHANI, H.; AKHAVAN-BEHABADI, M.; NARIMAN-ZADEH, N.; ABADI, M. M. Modeling and multi-objective optimization of square cyclones using CFD and neural networks. **Chemical Engineering Research and Design**, Elsevier, v. 89, n. 3, p. 301–309, 2011. DOI: https://doi.org/10.1016/j.cherd.2010.07.004.

SALVO, R. V. **Application of the Eulerian-Lagrangian methodology to the analyisys of the separation processes in cyclone separators**. 2013. PhD thesis – Universidade Federal de Uberlândia, Uberlândia. Available from: https://repositorio.ufu.br/handle/123456789/14717.

SANTOS, V. F. dos; SOUZA, F. J. de; DUARTE, C. A. R. Reducing bend erosion with a twisted tape insert. **Powder Technology**, v. 301, p. 889–910, 2016. DOI: https://doi.org/10.1016/j.powtec.2016.07.020.

SANTOS, V. F. d. **Numerical analysis of the efects brought by a twisted tape insert in elbow erosion**. 2018. PhD thesis – Universidade Federal de Uberlândia, Uberlândia. Available from: https://repositorio.ufu.br/handle/123456789/21519.

SARAMAGO, S. F. P. Métodos de otimização randômica: Algoritmos genéticos e "simulated annealing". *In:* SILVA, G. N.; ANDRADE, E. X. L. de; SAMPAIO, R. (eds.). **Notas em Matemática Aplicada**. São Carlos: SBMAC, 2012. v. 6. Republishing in e-book format of the original book published in 2003. ISBN 9788586883750. Available from: https://proceedings.science/series/23/proceedings_non_indexed/12.

SCHILLER, L.; NAUMANN, Z. A drag coefficient correlation. **Zeitschrift des Vereins Deutscher Ingenieure**, v. 77, p. 318–320, 1935.

SCHMIDT, S.; WADBRO, E.; BERGGREN, M. Large-scale three-dimensional acoustic horn optimization. **SIAM Journal on Scientific Computing**, SIAM, v. 38, n. 6, b917–b940, 2016. DOI: https://doi.org/10.1137/15M1021131.

SEDERBERG, T. W.; PARRY, S. R. Free-Form Deformation of Solid Geometric Models. **SIGGRAPH Computer Graphics**, Association for Computing Machinery, New York, USA, v. 20, n. 4, p. 151–160, 1986. DOI: https://doi.org/10.1145/15886.15903.

SILVEIRA NETO, A. da. **Escoamentos turbulentos**: Análise física e modelagem teórica. Uberlândia: Composer, 2020. ISBN 9786599036514.

SKINNER, S. N.; ZARE-BEHTASH, H. State-of-the-art in aerodynamic shape optimisation methods. **Applied Soft Computing**, Elsevier, v. 62, p. 933–962, 2018. DOI: https://doi.org/10.1016/j.asoc.2017.09.030.

SOLNORDAL, C. B.; WONG, C. Y.; BOULANGER, J. An experimental and numerical analysis of erosion caused by sand pneumatically conveyed through a standard pipe elbow. **Wear**, Elsevier, v. 336, p. 43–57, 2015. DOI: https://doi.org/10.1016/j.wear.2015.04.017.

SOMMERFELD, M. Numerical methods for dispersed multiphase flows. *In:* BODNÁR, T.; GALDI, G. P.; NEČASOVÁ, Š. (eds.). **Particles in Flows. Advances in Mathematical Fluid Mechanics**. Cham: Birkhäuser, 2017. p. 327–396. ISBN 9783319602820. DOI: https://doi.org/10.1007/978-3-319-60282-0_6.

SOMMERFELD, M.; HUBER, N. Experimental analysis and modelling of particle-wall collisions. **International Journal of Multiphase Flow**, Elsevier, v. 25, n. 6-7, p. 1457–1489, 1999. DOI: https://doi.org/10.1016/s0301-9322(99)00047-6.

SOMMERFELD, M. Validation of a stochastic Lagrangian modelling approach for inter-particle collisions in homogeneous isotropic turbulence. **International Journal of Multiphase Flow**, Elsevier, v. 27, n. 10, p. 1829–1858, 2001. DOI: https://doi.org/10.1016/s0301-9322(01)00035-0.

STACHOWIAK, G. W.; BATCHELOR, A. W. **Engineering tribology**. 4. ed. Boston: Butterworth – Heinemann, 2014. p. 852. ISBN 9780123970473.

STÜCK, A. **Adjoint Navier-Stokes methods for hydrodynamic shape optimisation**. 2011. s. 196. PhD thesis – Technische Universität Hamburg, Hamburg, Germany. DOI: https://doi.org/10.15480/882.1061.

STÜCK, A.; CAMELLI, F.; LOHNER, R. Adjoint-based design of passive and active shock mitigation devices. *In:* **Proceedings of the 48th AIAA Aerospace Sciences Meeting Including the New Horizons Forum and Aerospace Exposition**, Orlando, USA. AIAA, p. 1430. DOI: https://doi.org/10.2514/6.2010-1430.

STÜCK, A.; KRÖGER, J.; RUNG, T. Adjoint-based hull design for wake optimisation. **Ship Technology Research**, Taylor & Francis, v. 58, n. 1, p. 34–44, 2011. DOI: https://doi.org/10.1179/str.2011.58.1.003.

THÉVENIN, D.; JANIGA, G. **Optimization and computational fluid dynamics**. Berlin; Heidelberg: Springer, 2008. p. 294. ISBN 9783642091322.

VAN WACHEM, B.; SCHOUTEN, J.; VAN DEN BLEEK, C.; KRISHNA, R.; SINCLAIR, J. Comparative analysis of CFD models of dense gas-solid systems. **AIChE**

Journal, Wiley Online Library, v. 47, n. 5, p. 1035–1051, 2001. DOI: https://doi.org/10.1002/aic.690470510.

VASQUEZ, E. S.; WALTERS, K. B.; WALTERS, D. K. Analysis of particle transport and deposition of micron-sized particles in a 90 bend using a two-fluid Eulerian-Eulerian approach. **Aerosol Science and Technology**, Taylor & Francis, v. 49, n. 9, p. 692–704, 2015. DOI: https://doi.org/10.1080/02786826.2015.1062466.

VERSTEEG, H. K.; MALALASEKERA, W. **An introduction to computational fluid dynamics**: The finite volume method. 2. ed. Harlow; New York: Pearson Education, 2007. p. 503. ISBN 9780131274983.

WANG, D.; HE, L. Adjoint aerodynamic design optimization for blades in multistage turbomachines – Part I: Methodology and verification. **Journal of Turbomachinery**, American Society of Mechanical Engineers Digital Collection, v. 132, n. 2, 2010. DOI: https://doi.org/10.1115/1.3072498.

WILCOX, D. C. **Turbulence modeling for CFD**. 3. ed. La Cañada: DCW Industries, 2006. ISBN 9781928729082.

YU, G.; MÜLLER, J.-D.; JONES, D.; CHRISTAKOPOULOS, F. CAD-based shape optimisation using adjoint sensitivities. **Computers & Fluids**, Elsevier, v. 46, n. 1, p. 512–516, 2011. DOI: https://doi.org/10.1016/j.compfluid.2011.01.043.

YU, W.; FEDE, P.; CLIMENT, E.; SANDERS, S. Multi-fluid approach for the numerical prediction of wall erosion in an elbow. **Powder Technology**, Elsevier, v. 354, p. 561–583, 2019. DOI: https://doi.org/10.1016/j.powtec.2019.06.007.

ZHANG, Y.; REUTERFORS, E.; MCLAURY, B. S.; SHIRAZI, S.; RYBICKI, E. Comparison of computed and measured particle velocities and erosion in water and air flows. **Wear**, Elsevier, v. 263, n. 1–6, p. 330–338, 2007. DOI: https://doi.org/10.1016/j.wear.2006.12.048.

ZHU, H.; LI, S. Numerical analysis of mitigating elbow erosion with a rib. **Powder technology**, Elsevier, v. 330, p. 445–460, 2018. DOI: https://doi.org/10.1016/j.powtec.2018.02.046.

ZYMARIS, A.; PAPADIMITRIOU, D.; GIANNAKOGLOU, K.; OTHMER, C. Continuous adjoint approach to the Spalart-Allmaras turbulence model for incompressible flows. **Computers & Fluids**, Elsevier, v. 38, n. 8, p. 1528–1538, 2009. DOI: https://doi.org/10.1016/j.compfluid.2008.12.006.